9-PHASE INVERTER DRIVEN MOTOR

by

K. Hoffman

Submitted to the

Department of Electrical Engineering

of the

University of Cape Town

in fulfilment of the requirements

for the degree of M.Sc. (Eng.)

1983

INDEX.

Appendix D.

Acknowledgements.

I would like to thank the following people for their assistance and encouragement:- Professor N.C. Enslin, P. Hoffman, M. Attfield, P. Daniels, N. Wright, D. Kenyon, the Cooperative Scientific Program Group of the C.S.I.R. for their funding, G.E.C. and my employers Metal Box SA. Ltd.

Abstract.

The behaviour of a 9-phase squirrel cage induction motor is studied when it is excited with unmodulated and chopper modulated quasi-square phase voltages. A 9-phase bridge inverter, which produces the quasi-square waveforms, and its digital controller have been constructed and tested. A theoretical analysis is included, which shows the influence of phase current harmonics upon output torque.

Nomenclature.

α	Trapizoidal waveform angle (radians).
$B_o(\theta)$	$B_1(\theta) + B_2(\theta)$ (Wb/sq m).
$B_1(\theta)$	Airgap flux density developed by the stator windings.
$B_2(\theta)$	Airgap flux density developed by the rotor (armature reaction).
β	Voltage freewheel period (radians).
δ	Magnetic reluctance.
$e_2(t)$	Emf induced across rotor bar.
η	Efficiency.
$\mathcal{E}_{rnh}$	$k_{\omega n} . k_{dh} / \lvert Z_{rn} \rvert$
$\mathcal{E}_{snh}$	$k_{\omega n} . k_{dh}$
E_{nh}	$\mathcal{E}_{rnh} \cdot \mathcal{E}_{snh}$
$F_o(\theta)$	$F_1(\theta) + F_2(\theta)$.
$F_1(\theta)$	Airgap mmf developed by stator windings.
$F_2(\theta)$	Airgap mmf developed by rotor (armature reaction).
f_n	Frequency of nth harmonic (Hz).
γ	Standstill efficiency factor.
$\gamma(q,n)$	Angular spatial separation between windings (radians).
h	Time harmonic number.
i(t)	General instantaneous current.
$i_1(q,t)$	Instantaneous stator current in phase q.
$i_2(q,t)$	Instantaneous rotor current in assumed phase q.
I	Peak phase current.
k	Integer 0,1,2,3,4.....
k_{cn}	Chording factor.
k_{dh}	Current waveform factor.
k_{sn}	Spread factor.
$k_{\omega n}$	$k_{sn} . k_{cn}$
$k'_{\omega n}$	Rotor winding factor - assumed to be unity.
λ	Time related phase displacement between $F_1(\theta)$ and $F_2(\theta)$.
lg	Width of airgap.
L'_2	Rotor inductance referred to stator.
mmf	Magneto-motive force.
μ_o	Relative permeability.
n	Stator space harmonic number.
N	Number of turns in one slot.

p	Fundamental pole number.
Ψ	Variable integer.
$\phi(q,h)$	Time related phase shift between phase currents.
$\bar{\Phi}$	Instantaneous value of nth harmonic flux wave in airgap.
q	Phase number 0,1,2,3,4.....Q-1.
Q	Total number of phases.
r_1	Stator resistance.
r_2'	Rotor resistance referred to stator.
r_m	Iron loss resistance.
s_1	Fundamental slip.
$s(h,n)$	Slip of rotor due to hth time harmonic and nth space harmonic.
t	Time variable.
T	Period of input waveform.
θ	Angular displacement around airgap (rad).
θ'	Rotor referred angular displacement (rad).
θ_r, θ_R	Fundamental rotor impedance angle (rad).
θ_{rn}	nth harmonic rotor impedance angle (rad).
ω_1	Fundamental stator frequency (rad/sec).
ω_2	Fundamental rotor frequency (rad/sec).
ω_s	Synchronous speed of rotor (rad/sec).
ω_r, ω_R	Rotor speed.
ω_{rn}	Radial velocity of nth space harmonic relative to rotor.
Wg	Airgap energy density at a particular point.
Wgt	Total energy in airgap.
x_1	Stator reactance.
x_2'	Rotor reactance referred to stator.
x_m	Magnetizing reactance.
ξ	Maximum time harmonic.
Z_{rn}	Rotor nth harmonic impedance.

Introduction.

Developments in the field of power electronics and real time microprocessor control of power electronic components have made available methods and techniques for controlling multiphase induction motors which were previously not viable. The ability to produce variable frequency multiple phase converters has meant that the induction motor can now be used in traction applications. When operating at lower frequencies, for a low phase number, e.g. 3-phase, torque pulsations are very noticeable. If the motor is rewound or reconnected to accommodate a larger number of phase windings and the number of converter phases is similarly increased, the frequency of the torque pulsations will be increased and their amplitude decreased (2). The phase currents will also be lower for the same output power.

It is the objective of this thesis to investigate the behaviour of a variable speed multiphase sqirrel cage induction motor and converter to determine the practicabilities of using them in an electric vehicle. The primary power source to drive the vehicle will be a set of series connected batteries; thus the converter will be a dc to ac inverter.

To enable the inverter and its control logic to remain simple and inexpensive, quasi-square wave voltage excitation of the winding was considered practical and amplitude variation of the quasi-square wave was implemented by chopper modulating it with a variable mark/space ratio pulse chain.

The author has made use of the terms square wave, quasi-square wave and modulated quasi-square wave when referring to applied voltages. To avoid confusion a diagramatic representation of each of these types of wave is shown overleaf.

Note that a quasi-square wave becomes such when the freewheel angle becomes greater than zero (if the freewheel angle is zero the wave is square).

As a result of the type of excitation waveform used, the phase or stator currents will be of a square or trapiziodal nature. This in turn also causes

the magnetic flux distribution in the airgap of the motor to take on a square or trapeziodal form. Normally when a motor is excited with sinusoidal voltages the magnetic flux distribution will resemble a distorted sine wave (15). Theoretically, the trapeziodal flux distribution causes a $4/\pi$ increase in torque compared to the sinusoidal distribution, although as will be seen later, this is negated by losses associated with the impulse function type magnetizing current which is drawn when square or quasi-square wave excitation is used

To simplify the initial investigation, chopper modulation was not used to obtain a variable voltage output. The adjustable supply voltage was developed by a dc generator. Subsequently when the general characteristics of the motor and inverter were known, chopper modulation was introduced

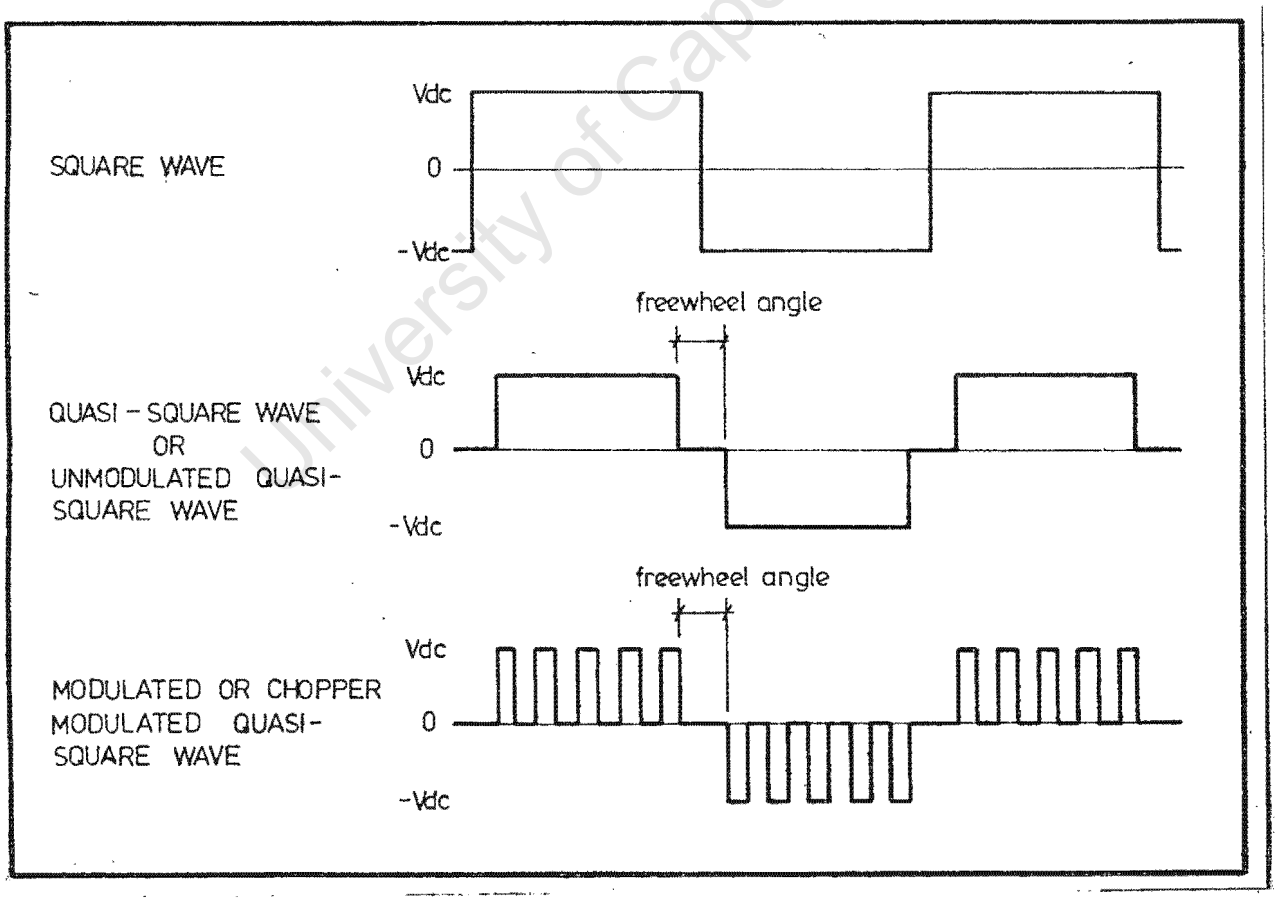

CHAPTER 1

Theoretical Analysis.

1.1 Airgap flux in a simplified induction motor.

When a multi-phase induction motor is excited with a set of polyphase sinusoidal voltages and currents, a fundamental sinusoidal flux wave is generated which rotates around the machine's airgap. Its rotational speed will be dependant on the frequency of the input current and the number of poles. If the number of phases and windings are infinite, only the fundamental sinusoidal flux wave would exist. However, as a result of the limited number of phases into which the coils are grouped, sets of harmonic waves will also be generated which have a detrimental effect on the performance of the machine (1). Chording of the windings is practised to alleviate the problem. To simplify the analysis harmonic flux components developed by the stator and rotor slots have been disregarded.

Torque producing current waveforms of a trapezoidal nature (refer section 1.2) are drawn by an induction motor when it is excited by square or quasi-square wave voltages. Each current time harmonic will develop a fundamental and a family of flux waves in the airgap of the motor. It is impossible to use chording to cancel all the unwanted components, a number of which, as will be shown later, produce reverse rotating fields. By increasing the number of phases, the more prominent detrimental components are reduced.

As a means of introducing the concept of a revolving flux field being a medium for transferring electrical to mechanical energy, in the form of a rotor producing torque, initially consider an infinite number of coils arranged symetrically around the circumference of the stator, each excited by a current;

$$i_q(t) = I\cos\left(\omega_1 t - \frac{2\pi q}{Q}\right) \quad Q \to \infty \; ; \; q=0,1,2\ldots Q-1 \qquad (1.1)$$

The ferro magnetic parts of the machine are assumed to be infinitely

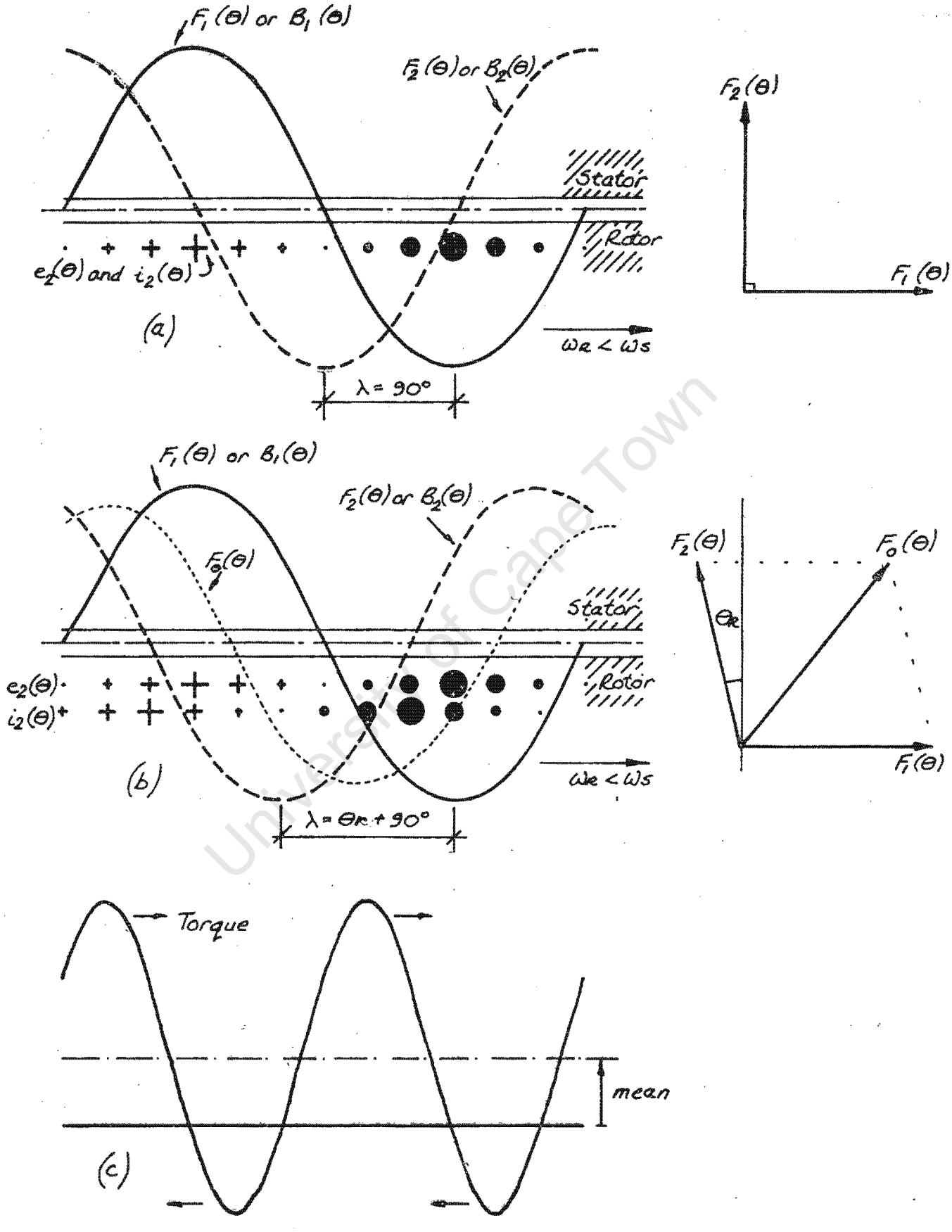

Figure 1.1 Airgap relations for induction motor. (a) Voltage, current & field relations for $(\omega_S - \omega_R)$ small. (b) Relations for $(\omega_S - \omega_R)$ relatively large. (c) Torque variations around airgap.

permeable and the airgap to be sufficiently small for the flux density across the airgap to be considered constant (3). Also, the magnetic field crossing the airgap links the rotor, as well as the stator windings, with no leakage (4), as indicated in figure 1.1a.

Figure 1.1a shows in development form the airgap, the stator mmf and the flux density distribution at a particular instant in time. The direction of the magnetic field movement is also shown with the rotor moving in the same direction, but at a lower velocity than the field. The induced voltages in the rotor conductors are shown as crosses and dots, with the size of the sign proportional to the instantaneous induced voltage. Thus, current flows in the rotor conductors with magnitudes determined by the induced voltages and the respective conductor impedance. The induced voltages and stator field move to the right with relative velocity ω_S with respect to the stator and $(\omega_S-\omega_R)$ with respect to the rotor. The stator conductors see source frequency, and the rotor conductors see a frequency dependant on relative velocity.

If $\omega_S=\omega_R$ (ie. slip=0) then the rotor frequency of the induced voltages and currents is zero. For the condition of small relative velocity (ie. slip tends to zero), the rotor currents are essentially in time phase with rotor voltages. Thus the crosses and dots in figure 1.1a represent the magnitude of both conductor voltage and current. Since the currents are distributed sinusoidally around the periphery of the rotor, they produce a sinusoidally distributed mmf wave in the airgap whose amplitude is space displaced from the current maximum by $\pi/2$ rad. (electrical). This rotor space distributed wave is shown as $F_2(\theta)$ and $B_2(\theta)$. As $(\omega_S-\omega_R)$ increases in magnitude, the rotor currents are no longer in time phase with the rotor induced voltages. They lag in time by the rotor impedance angle shown in figure 1.1b where;

$$\theta_r = \tan^{-1}(X_2/R_2) \qquad (1.2)$$

With both stator and rotor excited, the combined mmf F_1+F_2 produced by B_1+B_2 in the airgap gives a new sinusoidally distributed mmf F_o, which can be expressed as (5);

$$F_o(\theta)^2 = F_1(\theta)^2 + F_2(\theta)^2 + 2F_1(\theta)F_2(\theta)\cos\lambda \qquad (1.3)$$

1.2 Spatial mmf harmonics developed by time current harmonics in the airgap of a practical machine.

The mmf developed by a single full pitched stator winding which is being excited with a current i(t) can be expressed (appendix A.1) using Fourier series as;

$$F_1(\theta,t) = \frac{1}{2} Ni_1(t) \frac{4}{\pi} \sum_{n=1}^{\infty} \frac{1}{n} \sin n\theta \qquad (1.4)$$

$$n = 1,3,5,7.....$$

When the spread factor k_{sn} and chording factor k_{cn} are included, where;

$$k_{sn} = \sin(n\sigma/2)/(n\sigma/2)$$
$$k_{cn} = \sin(n\gamma/2)$$
$$k_{\omega n} = k_{sn}.k_{cn}$$

the developed mmf is given by;

$$F_1(\theta,t) = \frac{1}{2} Ni_1(t) \frac{4}{\pi} \sum_{n=1}^{\infty} \frac{k_{\omega n}}{n} \sin n\theta \qquad (1.5)$$

If there are Q phase-bands per pole, the spatial separation between each winding is;

$$\gamma(q,n) = 2\pi qn/Q \quad \text{where} \quad q = 0,1,2,3....Q-1$$

giving;

$$F_1(\theta,t) = \frac{1}{2} N \frac{4}{\pi} \sum_{q=0}^{Q-1} \sum_{n=1}^{\infty} \frac{k_{\omega n}}{n} i_1(q,t)\sin(n\theta-2\pi qn/Q) \qquad (1.6)$$

It can be seen in equation 1.6 that the input current has been additionally defined by the phase number q, where the phase shift between each current is;

$$\phi(q,h) = 2\pi qh/Q \qquad \text{where } q = 0,1,2,3....Q-1$$

Figures 1.2 show examples of the actual current waveforms obtained from machines under loaded and standstill conditions. These waveforms are of a

FIGURE 1.2

CURRENT WAVEFORMS OF 9-PHASE DRIVEN MOTORS : a) 5 HZ, 27 Nm, STANDSTILL; b) 5 HZ, 19 Nm, STANDSTILL; c) 5 HZ, 120 Nm, STANDSTILL

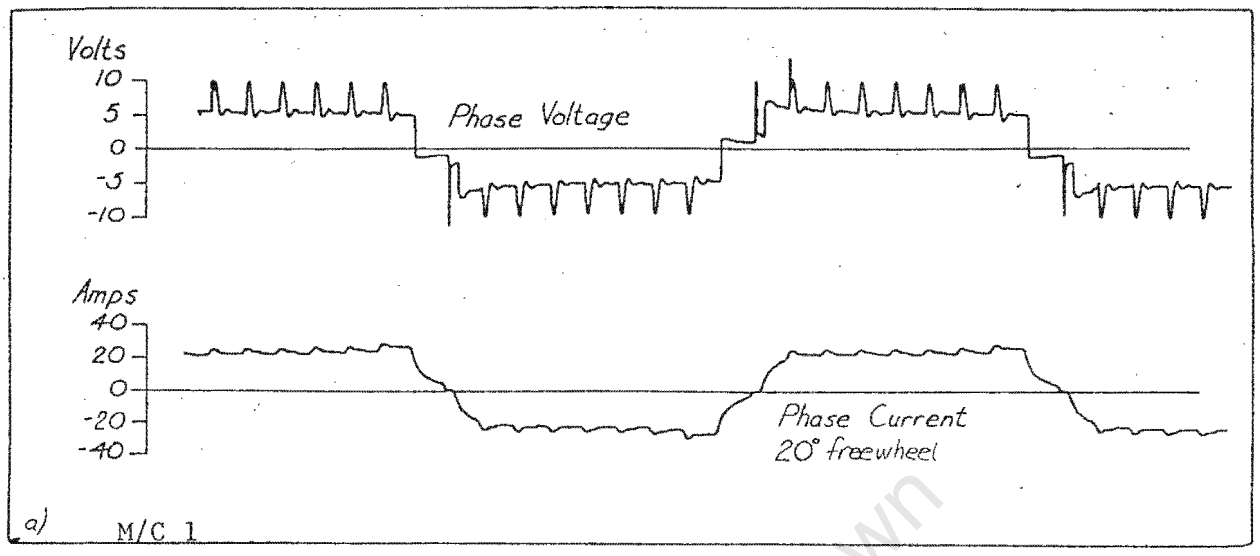

FIG 1.2a

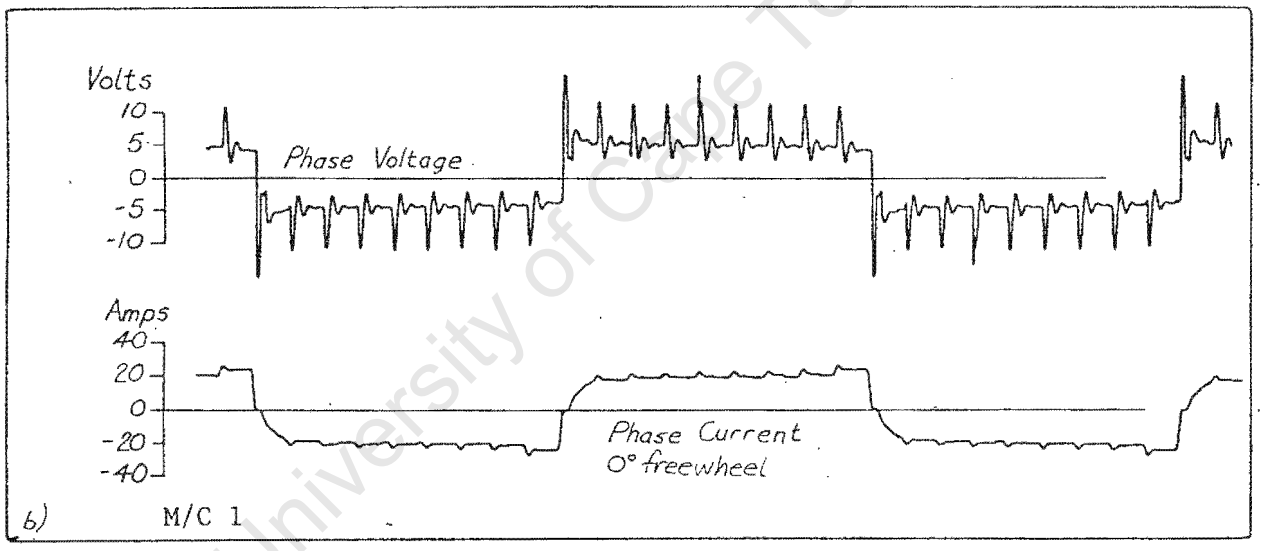

FIG. 1.2b

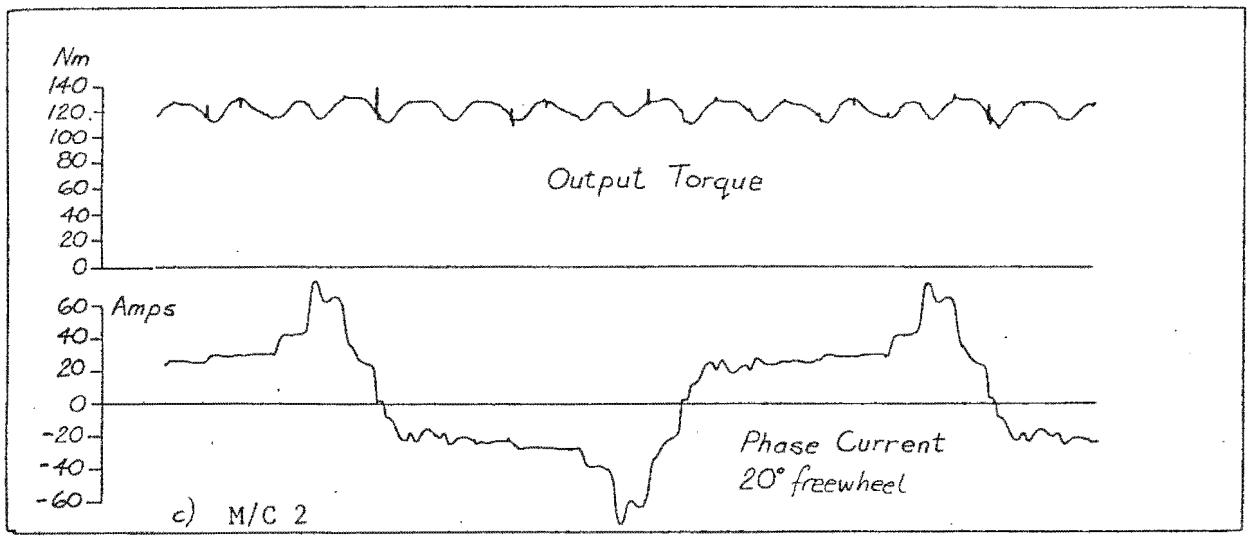

FIG. 1.2c

FIGURES 1.2 d, e & f

CURRENT WAVEFORMS FROM THE 9-PHASE CONNECTED TEST MOTOR UNDER LOADED CONDITIONS

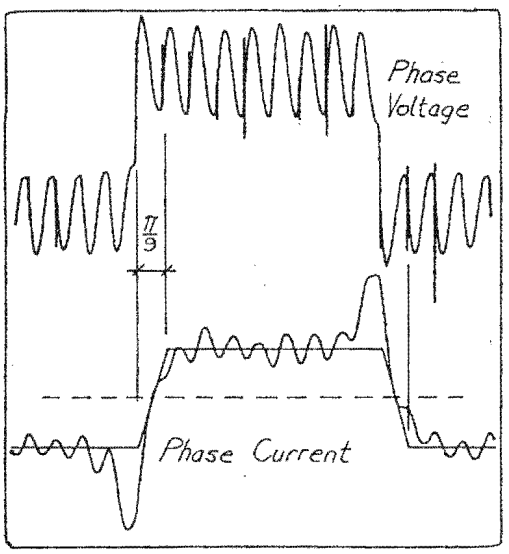

d) 9 Phase, 0° freewheel, 20 Hz

FIG 1.2d M/C 3

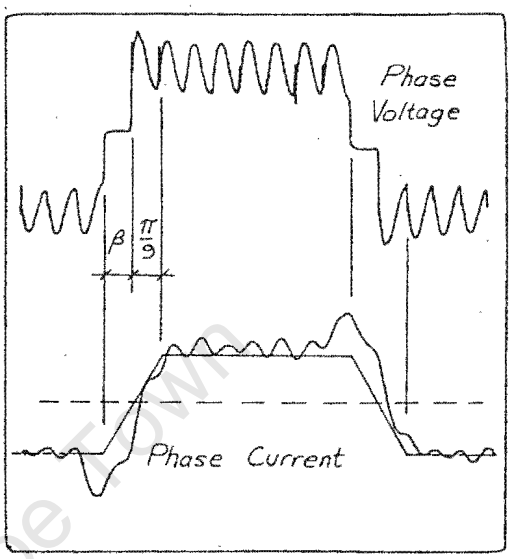

e) 9 Phase, 20° freewheel, 20 Hz

FIG 1.2e M/C 3

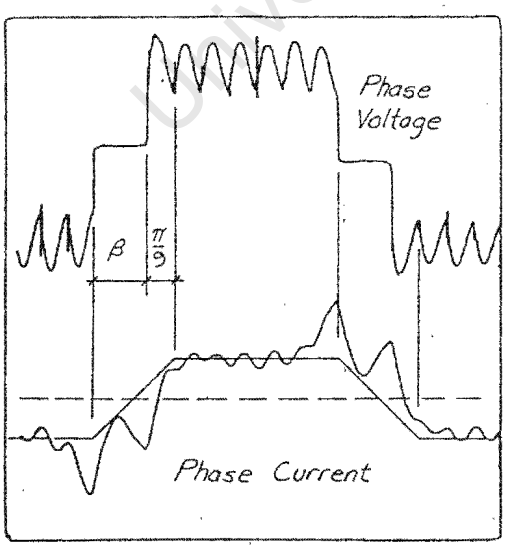

f) 9 Phase, 40° freewheel, 20 Hz

FIG 1.2f M/C 3

FIGURES 1.2 g, h, j & k

CURRENT WAVEFORMS FROM THE 3-PHASE CONNECTED TEST MOTOR UNDER LOADED CONDITIONS

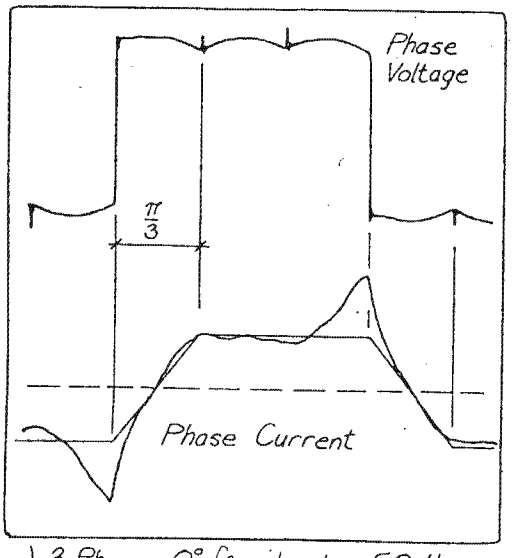

g) 3 Phase, 0° freewheel, 50 Hz

FIG 1.2g M/C 3

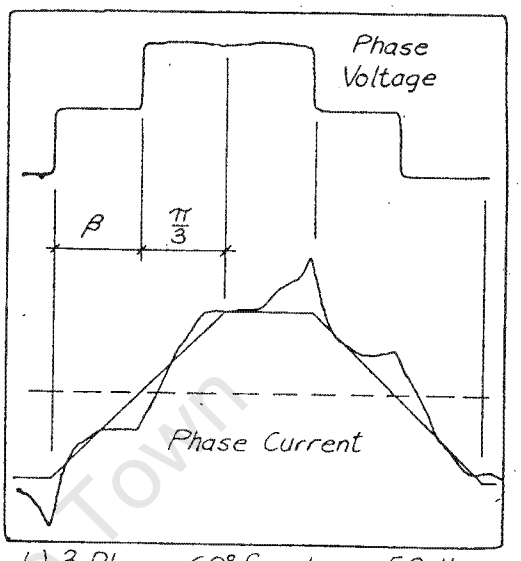

h) 3 Phase, 60° freewheel, 50 Hz

FIG 1.2h M/C 3

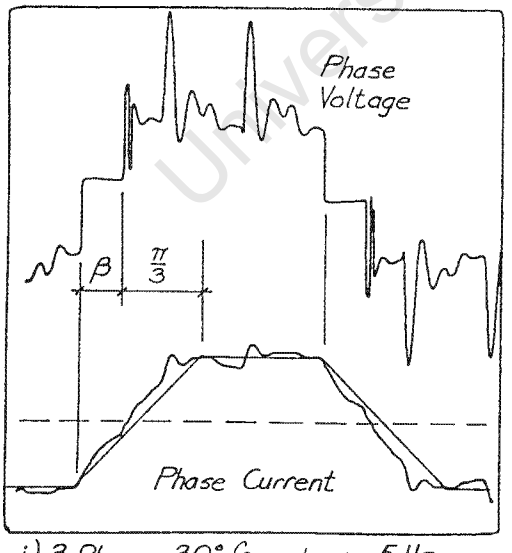

j) 3 Phase, 30° freewheel, 5 Hz Standstill.

FIG. 1.2j M/C 3

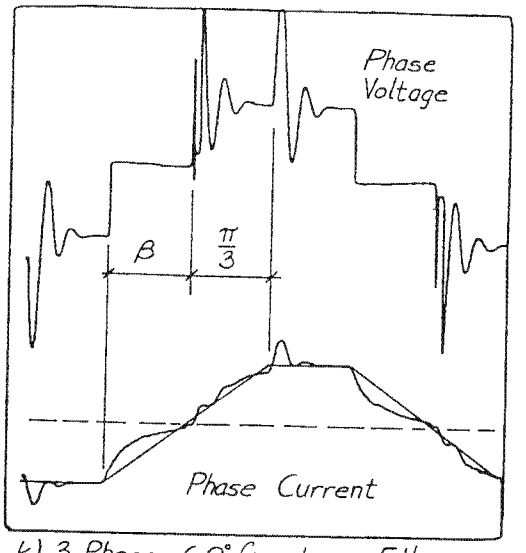

k) 3 Phase, 60° freewheel, 5 Hz Standstill.

FIG. 1.2k M/C 3

FIGURE 1.3

COMPUTER SIMULATED CURRENT WAVEFORMS WITH LIMITED HARMONICS

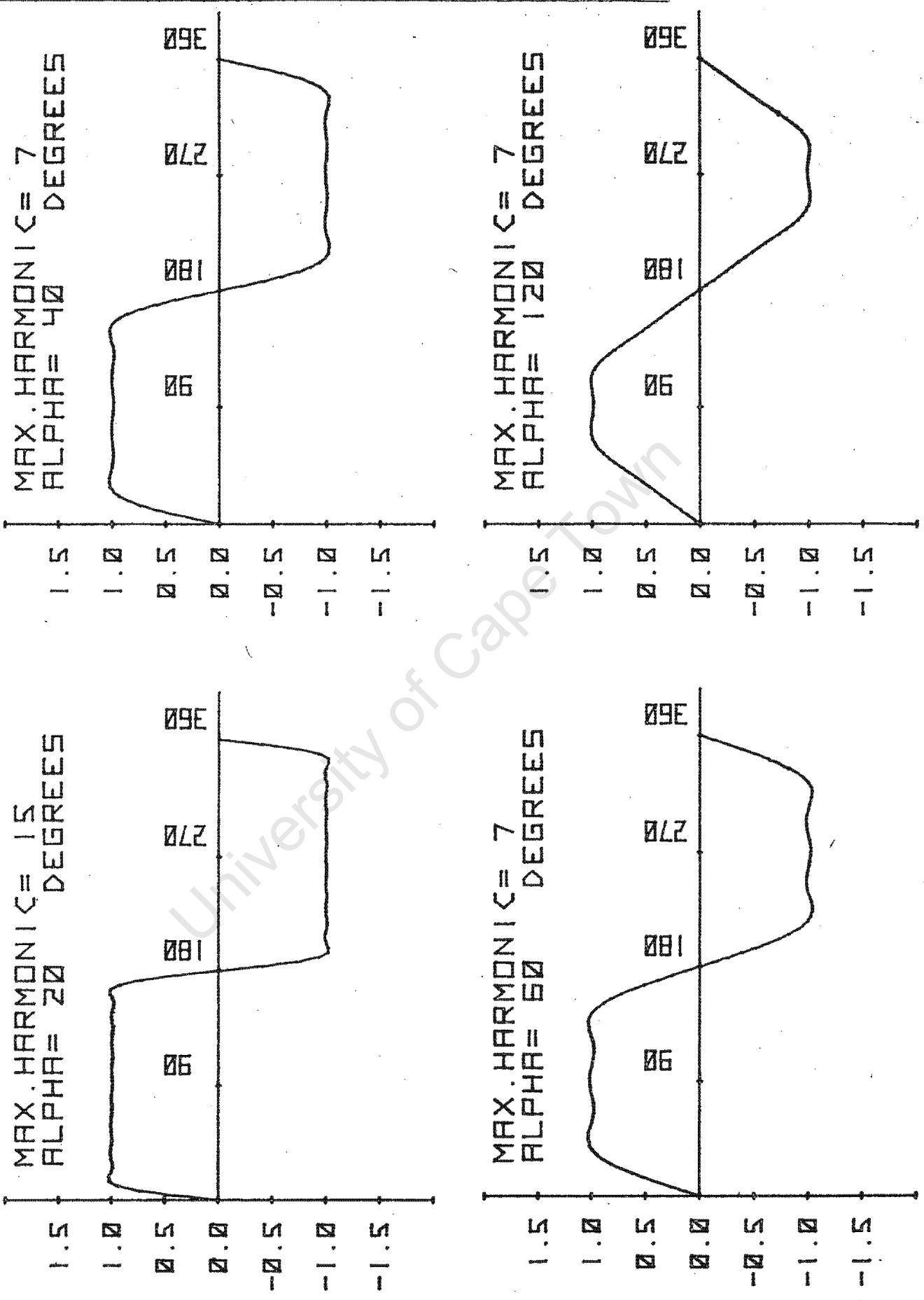

trapezoidal nature when the magnetizing current peak, which does not contribute towards the output power, is disregarded. By assuming the current to be trapezoidal with limited harmonics, see figure 1.3, a good approximation of the input current can be achieved. The Fourier representation of the input current is derived in appendix A.2 and shows that;

$$i_1(t) = \frac{4I}{\pi} \sum_{h=1}^{\xi} \frac{k_{dh}}{h} \sin h\omega_1 t \qquad (1.7)$$

where;

$$k_{dh} = \sin(h\alpha/2)/(h\alpha/2)$$

The phase current is therefore given by;

$$i_1(q,t) = \frac{4I}{\pi} \sum_{h=1}^{\xi} \frac{k_{dh}}{h} \sin(h\omega_1 t - 2\pi qh/Q) \qquad (1.8)$$

On closer inspection of figure 1.2;

$$\alpha \simeq \beta + \frac{\pi}{Q}$$

where β = underlap period of the voltage waveform.

The term π/Q is not entirely correct but it is a good approximation at low torques.

Introducing $i_1(q,t)$ into the mmf equation of 1.6 will give;

$$F_1(\theta,t) = \frac{1}{2} NI\left(\frac{4}{\pi}\right)^2 \sum_{q=0}^{Q-1} \sum_{n=1}^{\infty} \sum_{h=1}^{\xi} \frac{k_{\omega n} k_{dh}}{nh} \sin(h\omega_1 t - 2\pi qh/Q)\sin(n\theta - 2\pi qn/Q)$$

$$= \frac{1}{4} NI\left(\frac{4}{\pi}\right)^2 \sum_{q=0}^{Q-1} \sum_{n=1}^{\infty} \sum_{h=1}^{\xi} \frac{k_{\omega n} k_{dh}}{nh} \left\{\cos\left(h\omega_1 t - n\theta - \frac{2\pi q}{Q}(h-n)\right)\right.$$

$$\left. -\cos\left(h\omega_1 t + n\theta - \frac{2\pi q}{Q}(h+n)\right)\right\} \qquad (1.9)$$

Appendix A.3 shows that the trigonometric function of equation 1.9 can be modified to give, for a two pole machine (1,6,16);

$$\text{Stator developed mmf } F_1(\theta,t) = \frac{1}{4} NIQ\left(\frac{4}{\pi}\right)^2 \sum_{h=1}^{\xi} \frac{\mathcal{E}_{snh}}{nh} \cos(h\omega_s t - n\theta) \qquad (1.10)$$

where;

$$\mathcal{E}_{snh} = k_{\omega n}.k_{dh}$$
$$n = h \pm 2Qk$$
$$k = 0,1,2,3.....$$
$$h = 1,3,5,7.....\xi$$

This means that for every time harmonic h, which constitutes part of the phase current, a set of mmf space harmonics of value $h \pm 2Qk$ exist within the airgap. The period of the fundamental space harmonic is 2π radians.

If the input current approaches a square-wave the coefficient k_{dh} tends to unity, giving;

$$F_1(\theta,t) = \frac{1}{4} NIQ\left(\frac{4}{\pi}\right)^2 \sum_{h=1}^{\xi} \frac{k_{\omega n}}{nh} \cos(h\omega_s t - n\theta) \qquad (1.11)$$

And when the input current is sinusoidal, equation 1.10 is written;

$$F_1(\theta,t) = \frac{1}{4} NIQ\left(\frac{4}{\pi}\right) \sum_{n=-\infty}^{\infty} \frac{k_{\omega n}}{n} \cos(\omega_s t - n\theta) \qquad (1.12)$$

$$n = 1 \pm 2Qk$$
$$k = 0,1,2,3,4.....$$

So far only the mmf developed by the stator windings has been considered. However, for torque to be produced, the mmf distribution developed by the rotor must also be known.

The current induced in the bars of an ideal rotor is given by;

$$i_2(t) = e_2(t)/Z_{rn} \qquad (1.13)$$

where;

$$e_2(t) = -d\Phi_n/dt = -\frac{1}{\delta}.dF_1(\theta,t)/dt \qquad (1.14)$$

and therefore;

$$i_2(t) = -\frac{1}{\delta}.dF_1(\theta,t)/dt.(\underline{/\theta_{rn}}/|Z_{rn}|) \qquad (1.15)$$

Differentiating the stator developed mmf $F_1(\theta,t)$ of equation 1.10, remembering that a 90 degree phase shift is implicit within the differentiation, gives;

$$i_2(t) = K'I\sum_{h=1}^{\xi}\frac{\mathcal{E}_{rnh}}{n}\sin(h\omega_s t - n\theta - \theta_{rn}) \qquad (1.16)$$

where;

$$K' = \left(\frac{4}{\pi}\right)^2.NQ\omega_s/4\delta$$

$$\mathcal{E}_{rnh} = k_{\omega n}.k_{dh}/|Z_{rn}|$$

If the rotor rotates at a speed ω_r, the relative velocity of the nth harmonic, caused by a particular time harmonic h with respect to the rotor, will be (6);

$$\omega_{rn} = \frac{h\omega_s}{n} - \omega_r$$

Also, converting $i_2(t)$ to rotor referred coordinates using;

$$\theta' = \theta - \omega_r t$$

gives;

$$i_2(t) = K'I\sum_{h=1}^{\xi}\frac{\mathcal{E}_{rnh}}{n}\sin(n\omega_{rn}t - n\theta' - \theta_{rn}) \qquad (1.17)$$

Because the rotor currents cannot be represented as being continuous around the rotor circumference, due to the separate rotor bars, the term $n\theta'$ has been modified to $2\pi qn/Q$. Therefore;

$$i_2(q,t) \simeq K'I\sum_{h=1}^{\xi}\sum_{q=0}^{Q-1}\frac{\mathcal{E}_{rnh}}{n}\sin(n\omega_{rn}t - 2\pi qn/Q - \theta_{rn}) \qquad (1.18)$$

This shows that the rotor current is trapezoidal as expected.

The mmf developed by the rotor circuit is;

$$F_2(\theta',t) = \frac{1}{2}.\frac{4}{\pi}\sum_{q=0}^{Q-1}\sum_{m=1}^{\infty}\frac{i_2(q,t)}{m}\sin(m\theta'-2\pi qm/Q) \qquad (1.19)$$

And introducing $i_2(q,t)$ into equation 1.19 gives;

$$F_2(\theta',t) = K'\frac{2}{\pi}I\sum_{q=0}^{Q-1}\sum_{m=1}^{\infty}\sum_{h=1}^{\xi}\frac{\mathcal{E}_{rnh}}{mn}\sin(n\omega_{rn}t-2\pi qn/Q-\theta_{rn}).\sin(m\theta'-2\pi qm/Q) \qquad (1.20)$$

Equation 1.20 can be solved in a similar manner to equation 1.9 showing that;

$$F_2(\theta',t) = K'QI\sum_{h=1}^{\xi}\frac{\mathcal{E}_{rnh}}{mn}\cos(n\omega_{rn}t-m\theta'-\theta_{rn}) \qquad (1.21)$$

for $m = n \pm 2Ql \qquad l = 0,1,2,3.....$

$n = h \pm 2Qk \qquad k = 0,1,2,3.....$

$h = 1,3,5,7.....\xi$

If the mmf $F_2(\theta',t)$ is referred back to the stator co-ordinate system (6);

Rotor developed mmf $F_2(\theta,t) = K'QI\sum_{h=1}^{\xi}\frac{\mathcal{E}_{rnh}}{mn}\cos(\left[h\omega_s-n\omega_r\right]t-m\left[\theta-\omega_r t\right]-\theta_{rn})$ (1.22)

The rotating mmf waveform in the airgap of the motor is therefore made up of two separate mmf waveforms which are theoretically represented by equations 1.10 and 1.22.

1.3 Amplitude and velocity of the stator developed rotating mmf waves.

From equation 1.10, assuming a full pitched winding wound into two slots and excited with a trapezoidally shaped current waveform, the maximum p.u. amplitude of any mmf space harmonic n due to a time harmonic h is;

$$\text{Max. p.u. amplitude} = \left|\frac{k_{dh}}{nh}\right| \qquad (1.23)$$

Some harmonic mmf waves have been plotted in appendix A.4 for different instances in time. From these results table 1.1 can be deduced, which relates the velocity of a particular rotating mmf waveform with the space and time harmonics causing it.

Table 1.1 P.U. velocity of rotating mmf wave.

		Time harmonics h				
		1	3	5	7	9
	1	1	3	5	7	9
Space	3	1/3	1	5/3	7/3	9/3
Harmonics	5	1/5	3/5	1	7/5	9/5
n	7	1/7	3/7	5/7	1	9/7
	9	1/9	3/9	5/9	7/9	1

p.u. velocity ($\omega_s = 1$ p.u.)

This table shows that the rotational velocity of a particular space harmonic can be given by (6);

$$\text{rotational velocity} = \frac{h\omega_s}{n} \tag{1.24}$$

It should be noted, as shown in appendix A.4, that when n is negative the velocity is also negative, indicating that the particular harmonic is rotating in the reverse direction to the fundamental space harmonic and the rotor. All the reverse rotating harmonic components make up a negative sequence set.

If the slip of the rotor relative to the fundamental speed ω_s is s_1, the slip of the rotor relative to any non-synchronous harmonic can be given as;

$$\text{rotor slip} \quad s(h,n) = \left(\frac{h\omega_s}{n} - \omega_r\right)/\left(\frac{h\omega_s}{n}\right) \tag{1.25}$$

$$\omega_r = \omega_s(1 - s_1)$$

Therefore;

$$s(h,n) = 1 - \frac{n}{h}(1 - s_1) \tag{1.26}$$

The tabulation of equations 1.23, 1.24 and 1.26 is given in appendix A.5. For each time harmonic h of the stator current waveform, the following are given;

i) The set of mmf space harmonics which are developed in the airgap as a result of the time harmonic.

ii) The p.u. amplitude of each space harmonic, assuming that the trapezoidal current waveform was actually tending to a square wave. (This is impossible, but it does provide a convenient reference for comparing amplitudes due to a different number of supply phases).

iii) The p.u. rotational velocity of each space harmonic around the airgap with reference to the fundamental mmf harmonic velocity.

iv) The p.u. slip of the rotor relative to the particular space harmonic, assuming that the rotor's fundamental slip $s_1 = 0$.

Following the tables for 3 and 9 phases are graphs showing the variation in amplitude resulting from a change of freewheel period (also see figures 6.3 and 6.4). It should be remembered that the angle given in the graphs $\alpha = \beta + \pi/Q$.

1.4 Determination of p.u. torque.

According to Maxwell, the energy density at any point in the airgap is given by;

$$Wg = B_o^2/2\mu_o = F_o^2\mu_o/2lg = kF_o^2 \qquad (1.27)$$

$$k = \mu_o/2lg^2$$

The total energy in the airgap will be;

$$Wgt = Wg \times \text{Volume} = KF_o^2 \qquad (1.28)$$

$$K = (\mu_o \times \text{Volume})/2lg^2$$

For given currents, the torque developed can be stated as;

$$T = dWgt/d\lambda = K.d(F_o^2)/d\lambda \qquad (1.29)$$

The only term in equation 1.3 dependant on λ is $2F_1(\theta)F_2(\theta)\cos\lambda$, so that (4,5);

$$T = 2KF_1(\theta)F_2(\theta)\sin\lambda = 2KF_1(\theta)F_2(\theta)\cos\theta_r \qquad (1.30)$$

Substituting equation 1.10 and equation 1.22 into the torque equation 1.30, remembering that the phase shift between F_1 and F_2 has been taken account of in F_2, gives;

$$T(\theta,t) = K\,I^2 \sum_{h=1}^{\xi} \frac{\mathcal{E}_{rnh}}{mn} \cos(h\omega_s t - \omega_r t[n-m] - m\theta - \theta_{rn}) \cdot \sum_{h=1}^{\xi} \frac{\mathcal{E}_{snh}}{nh} \cos(h\omega_s t - n\theta)$$

$$= K\,I^2 \sum_{h=1}^{\xi} \frac{E_{nh}}{mn^2h} \cos(h\omega_s t - \omega_r t[n-m] - m\theta - \theta_{rn}) \cos(h\omega_s t - n\theta) \qquad (1.31)$$

where;

$$E_{nh} = \mathcal{E}_{rnh} \cdot \mathcal{E}_{snh} = (k_{\omega n} \cdot k_{dh})^2 / |Z_{rn}|$$

$$K = \frac{NQ^2\omega_s}{4\delta} \left(\frac{4}{\pi}\right)^2$$

The shaft output torque will be;

$$T(t) = \int_0^{p\pi} T(\theta,t)\, d\theta \qquad (1.32)$$

Because p, the number of poles, is an even number;

$$T(t) = 0 \quad \text{for } m \neq n$$

and there will only be a real solution when $m = n$ (6). That is, a torque can arise only if for a certain stator harmonic of the order $n = \Psi$ there exists within the rotor spectrum a harmonic m also equal to Ψ. This means that a torque can only be produced by harmonics having an equal number of pole pairs (16). The output torque will therefore be (6);

$$T(t) = KI^2 \sum_{h=1}^{\xi} \frac{E_{nh}}{\Psi^3 h} \int_0^{p\pi} \cos(h\omega_s t - \Psi\theta - \theta_{rn}) \cos(h\omega_s t - \Psi\theta)\, d\theta \qquad (1.33)$$

and the solution is;

$$T(t) = \frac{K}{2} I^2 \sum_{h=1}^{\xi} E_{nh} \frac{p\pi}{\Psi^3 h} \cos\theta_{rn} = \text{Constant for constant slip.} \qquad (1.34)$$

$\Psi = m = n \qquad m = n \pm 2Ql \qquad n = h \pm 2Qk$

$l = 0,1,2,3.... \qquad k = 0,1,2,3.... \qquad h = 1,3,5,7....\xi$

$$\theta_{rn} = \tan^{-1}(s2\pi f\, nL_2'/r_2')$$

Equation 1.34 shows that contribution to the output torque by space harmonics Ψ of a higher order become negligible.

Using the proviso that m must equal n for a torque to be produced, one may deduce, with the aid of the tables in appendix A.5, the relationships between time, stator and rotor harmonics required for this torque production. These are;

i) Each current time harmonic h, produces a range of stator space harmonics rotating in the airgap of the order $n = h \pm 2Qk$.

ii) For a stator space harmonic of value $n = \Psi$, there exists more than one rotor space harmonic m of the same value, i.e. $m = \Psi$ ($m = n \pm 2Ql$).

iii) Each of the rotor space harmonics of the value $m = \Psi$ are developed as a result of a stator space harmonic of the value $n = h(n) \pm 2Qu$.

$h(n)$ = time harmonic causing the original stator space harmonic $n = h \pm 2Qk$.

$u = 0,1,2,3$ .....

For example, a three phase machine has a stator space harmonic rotating in the airgap of order n = 1, which is caused by the time harmonic h = 1. The rotor also develops a number of space harmonics of the order m = 1, one of which is a direct result of the harmonic n = 1. The other rotor space harmonics of value m = 1 are caused by stator space harmonics of the order $1 \pm 6u$, i.e. n = ...-17,-11,-5,1,7,13,19 .....

The rotational velocity of each of the rotor space harmonics from equation 1.24 is;

$$\text{Velocity} = h\omega_s/n = h\omega_s/m \qquad \text{for } m = n = \Psi$$

Therefore, if rotor and stator developed space harmonics have the same pole-pair number, they will also have the same rotational velocity , thus enabling them to react with each other and produce torque.

1.5 Magnetizing current.

Magnetizing current flowing through the stator produces the mmf which is required to develop the flux enabling the rotor to produce torque as a function of slip.

In the case of a sinusoidally excited motor, the magnetizing current will lag the applied voltage by 90 degrees. It will also be sinusoidal provided the stator and rotor are not magnetically saturated. Assuming that saturation does not take place, the relationship between magnetizing current $i_m(t)$ and back emf e (t) is:

$$e(t) = -\frac{N^2}{\delta} \cdot \frac{di_m(t)}{dt} \qquad (1.35)$$

Figure 1.4a shows that peak magnetizing current occurs when $de(t)/dt = max.$ i.e. at the zero volts cross-over point.

When square or quasi-square wave voltages are used to excite the motor, the induced magnetizing current becomes a chain of alternatively positive and negative impulse functions $\delta(t)$ as shown in figures 1.4b and c. Magnetizing power can only be drawn from the supply in small 'gulps' and the amplitude of the current impulse function is directly proportional to the amplitude of the voltage step and its harmonics depend on its duration.

In practice the motor cannot support this type of current waveform and the step increase and decrease of the impulse function is modified to become exponentially increasing and decreasing (see figure 1.4d). The fact that the magnetizing current starts to exponentially increase before the voltage step occurs is due to the coupling between the phases. A theoretical analysis has been performed (14), using a coupled circuit model and impedance matrix, which predicts the phase current waveform shape. Figure 1.5 shows one of the waveforms obtained from this computer simulation, from which the magnetizing current peaks can be clearly seen.

FIG. 1.4

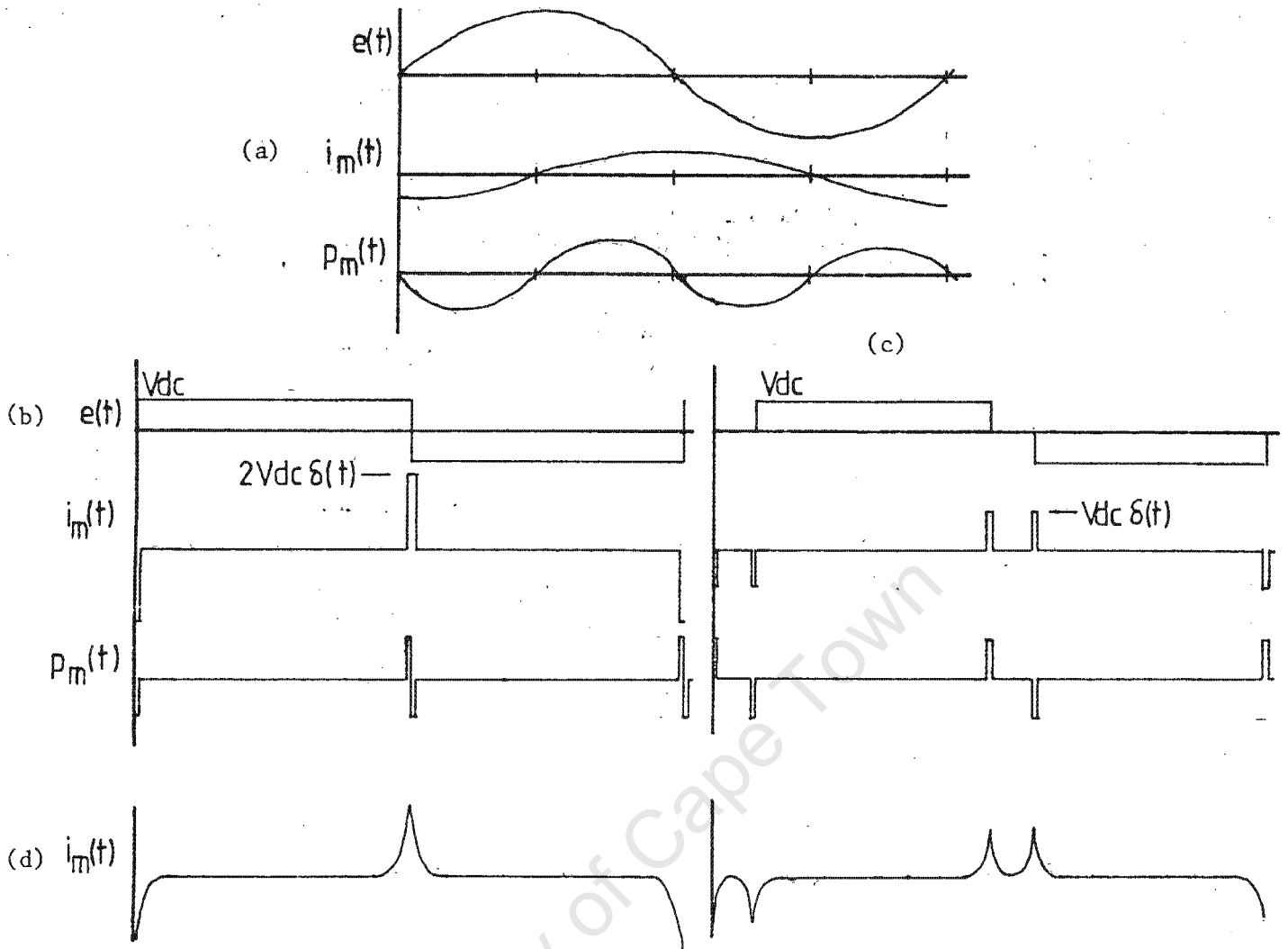

FIG. 1.4 Theoretical no-load magnetizing current and power for (a) Sinusoidal (b) Squarewave and (c) Quasi-square wave excitation

FIG. 1.4d No-load magnetizing current in practice.

FIG. 1.5 Computor simulated current waveform.

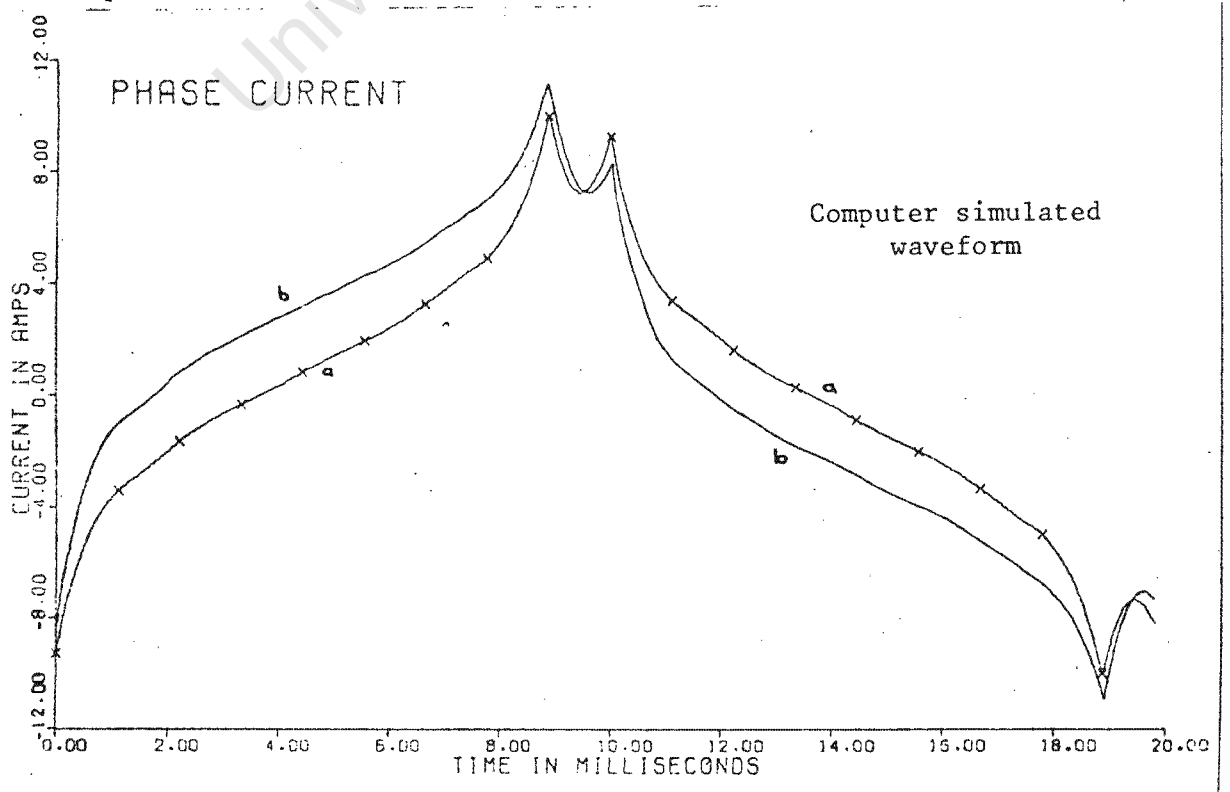

FIG. 1.5 CURRENT WAVEFORM FOR 50 Hz, 26V WITH A SLIP OF (a) 0% (b) 5%

1.6 Conclusions drawn from theoretical results.

Theory has shown that for quasi-square wave voltage excitation, the torque produced at the output shaft of a motor is given by;

$$T(t) = \frac{K_1}{2} I_{tr}^2 \sum_{h=1}^{\xi} E_{nh} \frac{p\pi}{\psi^3 h} \cos \theta_{rn} \qquad (1.36)$$

For a sinusoidally applied voltage waveform, the output torque can be calculated to be;

$$T(t) = \frac{K_2}{2} I_{si}^2 \sum_{n=1 \pm 2Qk} E_n \frac{p\pi}{\psi^3 h} \cos \theta_{rn} \qquad (1.37)$$

Where;

I_{tr} = Peak value of trapezoidal current.

I_{si} = Peak value of sinusoidal current.

$K_2 = (\pi/4)\ K_1$

$E_n = K_{\omega n}^2 / |Z_{rn}|$

If it is assumed that the fundamental component of the trapezoidal current will give the same performance as the sinusoidal current, one can then determine the effect upon the output torque of the additional trapezoidal harmonics. The difference in number of phases is taken into account in the terms K_1 and K_2, the difference in pole number (if applicable) in p and chording and spread factors are assumed equal for various phase combinations.

The torque variation resulting from the additional harmonics will therefore be given by;

$$\Delta T(t) = \frac{K_1}{2} I_{tr}^2 p\pi \left(\sum_{h=3}^{\xi} E_{nh} \cos \theta_{rn} \cdot \sum_{h=3}^{\xi} \frac{1}{\psi^3 h} \right) \qquad (1.38)$$

Of primary importance is the term $1/\psi^3 h$. The amplitude of this term has been tabulated in table 1.2 and shows how many and to what extent the airgap space harmonics are affected by the phase number Q. For simplification the rotor 'back emf' space harmonic components m have been ignored. Table 1.2 was constructed using information contained in appendix A.5.

A few points should be noted;

(i) Earlier in this chapter the maximum time harmonic component of the

FIGURE 1.6

3-PHASE HARMONIC TORQUE-SPEED CURVES

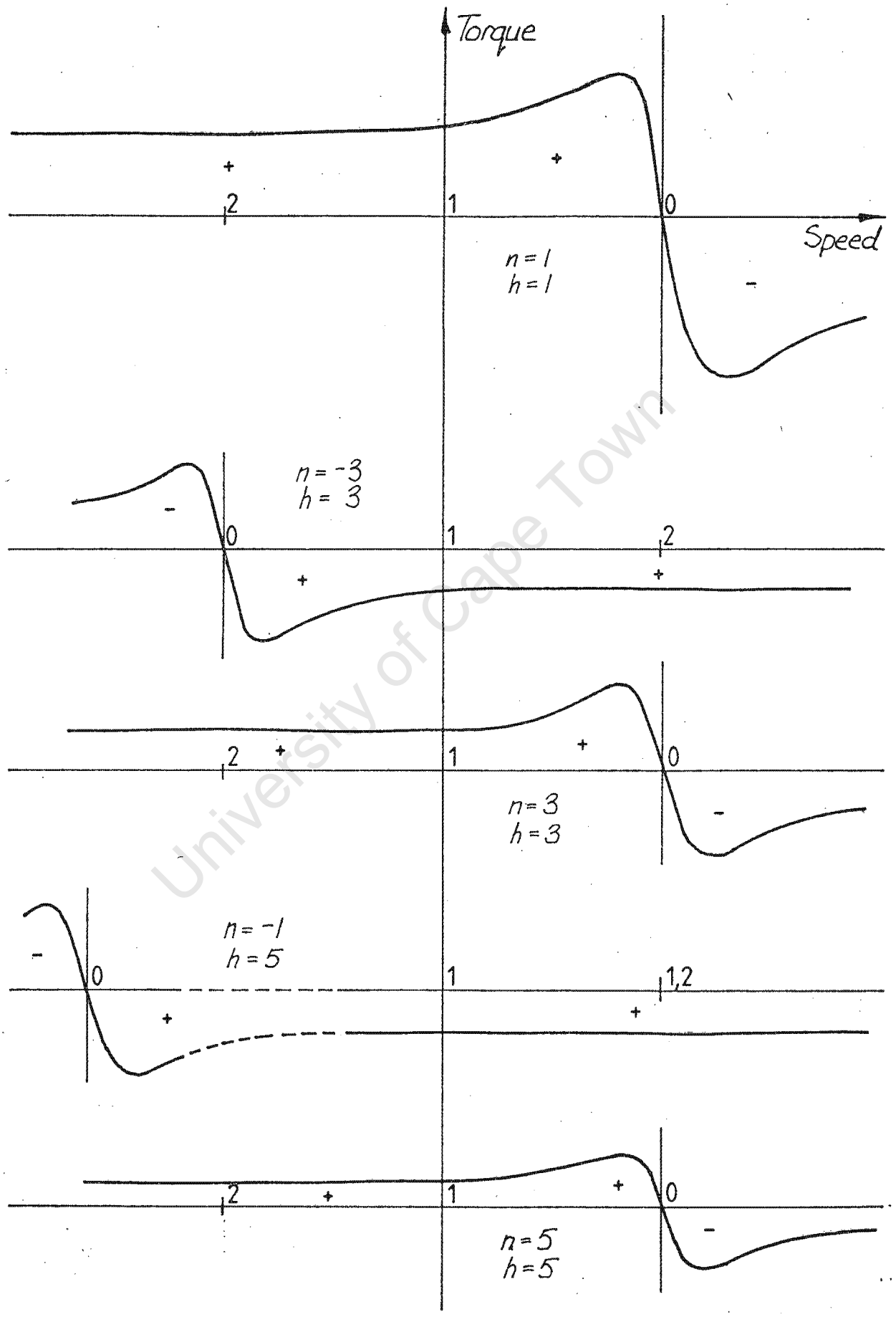

Not to scale.

TABLE 1.2

SPACE HARMONIC SLIP AND AMPLITUDE FOR A 3-POLE PAIR MACHINE

Q=3	n=-7		n=-5		n=-3		n=-1		n=1		n=3		n=5		n=7	
h	x	slip	x	slip	x	slip	x	slip	x	slip	x	slip	x	slip	x	slip
3					0,012	2,00					0,012	0				
5	0	2,4					0,2	1,2					0,002	0		
7			0,001	1,71					0,143	0,86					0	0
9					0,004	1,33					0,004	0,67				

Q=5																
3	0,001	3,33									0,012	0				
5			0,002	2,0									0,002	0		
7					0,005	1,43									0	0
9							0,111	1,11								

Q=7																
3											0,012	0				
5													0,002	0		
7	0	2,0													0	0
9			0,001	1,56												

Q=9																
3											0,012	0				
5													0,002	0		
7															0	0
9																

Q=11																
3											0,012	0				
5													0,002	0		
7															0	0
9																

$x = 1/\psi^3 h$

input current waveform was discussed. A value of h=9 has been chosen as a practical figure.

(ii) The value of slip given in table 1.2 is that of the rotor relative to the particular space harmonic. Negative space harmonics produce torques rotating in the opposite direction to the rotor and therefore result in negative torques. Figure 1.6 show torque-speed curves of some of the harmonics involved in a 3 phase system. Note the inverted curves of the negative sequence harmonics.

(iii) Although appendix A.5 shows theoretically that negative slip values do exist, in practice they are inneffective as a result of the low magnitude time harmonics and large slip. Only positive slip values are present and this indicates that regenerative harmonics do not occur in the normal motoring mode.

From table 1.2 it can be seen that for the 3 phase excited test motor with its winding configuration and connection, negative torque producing space harmonics exist which theoretically preclude the use of 3 phase quasi square wave excitation. It should be noted that the 3rd and 9th time harmonics are zero sequence components and provided they are not excited, produce no torque. They do, however, produce losses unless a freewheel period is chosen so that α = 120 deg., which effectively reduces these components to zero. A nine phase system's first zero sequence time harmonic is the 9th which has limited influence on the output because of its high harmonic number and, as will be shown later, draws very little power from the supply.

As the phase number Q is increased, and due to the limitation of the order of time harmonics considered, the number and amplitude of the significant positive and negative asynchronous space harmonics decreases.

Once a 9 phase system is reached, only positive synchronous torques of any significance remain and of these only the 3rd and the 5th have a positive effect on the output.

It has, with these facts in mind, become apparent that a 9 phase system should be tested. A 9 phase motor also provides an additional bonus in that as a result of the winding configuration, the motor, by external reconnection, can be easily converted to three phase operation.

CHAPTER 2.

General Description of System.

2.1 Description of circuit and measuring equipment used.

Figure 2.1 show the electrical and mechanical interconnections of the test system. The 9-phase test motor (a standard frame GEC 15 KW sqirrel cage induction motor rewound) is mechanically coupled to a HBM torque tranducer which has an accuracy of 0.2% and a maximum torque of 200 Nm. The torque transducer is in turn mechanically coupled to a Siemens 50 KW, 400 V, 50 Hz induction motor which is used as a brake.

A dc supply for the 9-phase dc to ac inverter is obtained via a motor-generator set, with the dc generator capable of supplying 500 A at 440 Vdc. A 600 KVA star connected alternator feeding through a 6.6 KV to 400 V, core type, 3-phase transformer provides the brake motor with power. The alternator is also part of a motor-generator set whose rotational speed is controlled by a phase controlled ac to ac converter.

The test motor excitation is supplied by a 9-phase dc to ac inverter which, by reprogramming the digital controller, is capable of supplying square waves or quasi-square waves of various freewheel angles to the motor. Reprogramming will also allow 3-phase square or quasi-square waves to be chosen.

Electrical measurements were taken at the dc input to the inverter and the ac input to the test motor. The dc measurements used moving coil instruments with an accuracy of 0.5% while the ac measurements were taken on a Marek power/volts/amps analyser which has an accuracy of 0.5% for frequencies between 0 and 50 KHz. For both dc and ac current measurements calibrated shunts were used. To avoid induced emf's in the ac ammeter's shunt connection a coaxial line high frequency shunt was used. AC measurements in any phase could be taken by selecting, on a multiposition voltage switch, the particular phase neutral and then plugging the shunt into circuit.

FIG. 2.1 Electrical and mechanical interconnections of test system.

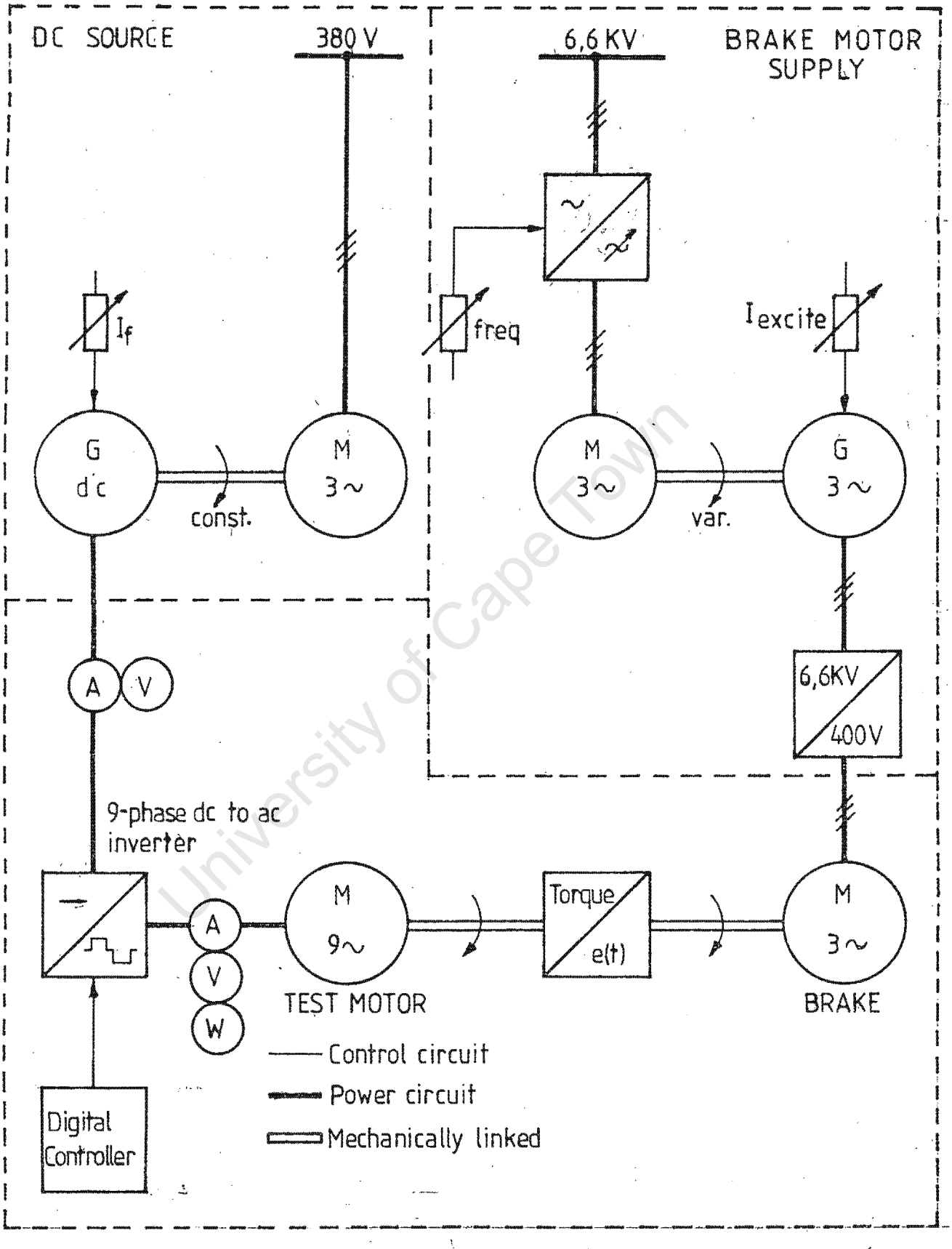

2.2 The type of dc to ac inverter used.

Square or quasi-square voltage waves, suitably phase shifted to accommodate driving a 9 phase induction motor, are obtained by using nine dc to ac force commutated transistorized bridge inverters. The switching signals for the four transistors in each bridge are developed by a logic controller, described later, which enables the bridge inverter to operate at variable frequency and the desired voltage which is obtained by chopper modulating the output waveform from each bridge.

Figure 2.2 shows an idealized bridge inverter circuit. The ESM 1000 npn power switching transistors (produced by Thompson CSF) have a Vceo = 100 V and Ic = 150 A. Peak collector current is 200 A and saturated gain 10.

As a result of the high base current (it was envisaged that the peak collector current would rise to 100 A therefore a base current of 10 A was required), and the fact that all the transistors are npn, small transformer isolated base drive units were used for each transistor. The base drive unit is switched on and off directly by logic signals from the controller.

Two types of over current protection were used to protect the bridge inverter and control circuitry. Firstly water fuses were found to successfully protect the ESM 1000 power transistors if short circuit conditions accidently occurred. The author has performed extensive tests on this type of fuse (8) and found it essential to select the correct diameter fuse wire for the particular operating conditions. Fuse wire sizes are given in reference 8. Water fuses were placed in the dc supply lines to each bridge inverter and thus, on failure, disconnected the dc supply from the bridge.

A further overcurrent combined with over voltage protection circuit was used to switch the logic controller off in the event of those conditions occurring. The circuit diagram is given in appendix B.2.

2.3 Digital controller specifications and operation.

It was felt that a microprocessor based controller would require too much

Figure 2.2

a) Idealized bridge inverter circuit.

b) Equivalent circuit representation of motoring and regeneration with chopper modulation.

Figure 2.3

a) Phase voltages for all nine phases with a set freewheel period ie. when output is zero.

b) 1/9 mark-space ratio taken at a selected time during a cycle. Note the inneffective interlacing at the quasi-square wave change over points.

c) 3/9 mark-space ratio.

d) The time delay which can be set at the logic controller to account for switching on and off delays of the ESM 1000.

Figures 2.2 a and b

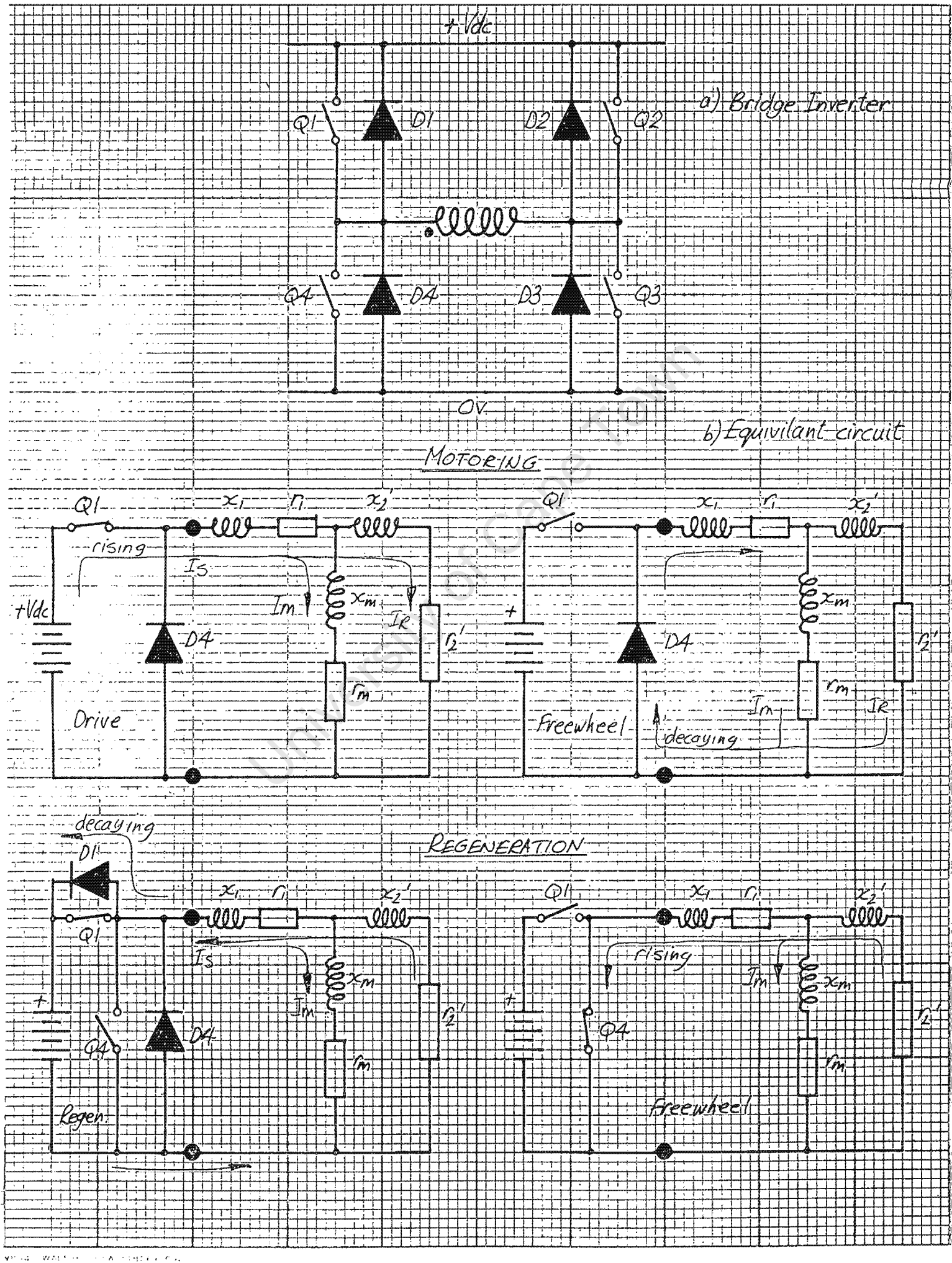

Figure 2.3 a,b,c and d

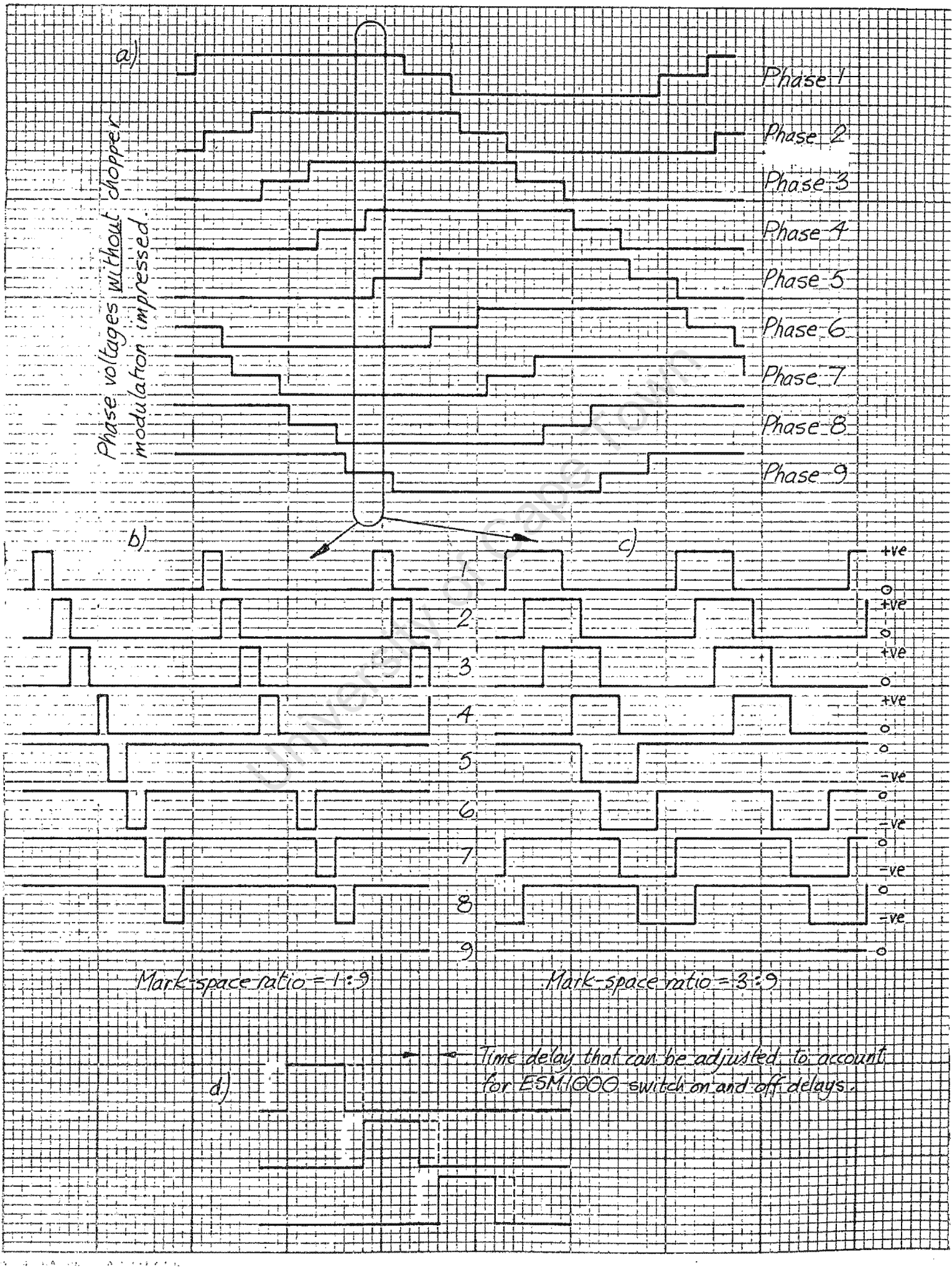

development time and in fact be unneccessarily complex for the type of experimentation required. A pure logic controller with no feedback and limited operator run mode controls was constructed.

Selection of the type of waveform, i.e. square or quasi-square, is by programming the controller's RAM. Although the controller was designed specifically for 3-phase and 9-phase operation any number of phases between 1 and 9 can be chosen. However, due to the type of design used, there are small inherent timing errors when operating in the 4, 5 or 8-phase mode.

Once the controller has been switched to its run state, the operator has control over frequency (which is continuously variable between 0.1 and 100 Hz), mark-space ratio of chopper modulation signals (which is variable in 9 steps between 0/9 to 9/9) and forward or reverse operation of the motor (selector switch).

The circuitry was designed around the 7400 series 5 V logic family and a MCM6810 MOSFET RAM. Output buffers to the base drive units supply 12 V logic signals.

2.4 Reasons for using interlaced chopper modulation of the excitation waveform and its effect on regeneration.

There are two basic reasons for introducing interlaced chopper modulation into the system. The first and the most obvious is to provide an effective variable voltage supply from a fixed dc source by varying the mark-space ratio of the chopping signal. The second reason is to provide control over current regeneration back into the dc supply when the motor is being driven or being braked. To reduce the amplitude of the current spike drawn from or supplied to the dc source when each transistor switches on or off, interlacing was added. This means that when one phase is being switched on, another, at the same time, is being switched off to produce a continuous supply current.

For a 9 phase bridge inverter the number of mark-space ratio steps required to obtain interlaced chopping is 9. That is, mark-space ratios of between 0/9 to 9/9 should be available. Figure 2.3b shows the sequence of chopping

for a 1/9 mark-space ratio, whereas 2.3c is for a 3/9 mark-space ratio. Figure 2.3d also shows the preset variable time delay that was introduced so that ESM 1000 switching delays could be accommodated.

Although in previous experiments (7) the chopping frequency was synchronized with the main applied running frequency, it was felt that better efficiencies could be obtained if the chopping frequency was made constant and not synchronized. This, as will be shown later, did allow higher motor efficiencies but as shown in figure 2.3, caused the interlacing to be ineffective at the quasi-square wave change over points.

It was also desirable to produce a system whereby the induction motor could operate between its motoring and regeneration regions without changing the switching sequence of the bridge inverter. This was possible by using a system developed by Malengret (7) and modified by Scrooby (11). The bridge inverter therefore operates in the following manner.

Referring to figure 2.2a, during the first half cycle Q3 remains on all the time. Q1 and Q4 will alternate on and off according to a set mark-space ratio. Remember that at low motoring speeds, to avoid saturation, the mark-space ratio must be low, e.g. 1/9, to give a low effective phase voltage, and at high motoring speeds it will be high e.g. 8/9. During low speed motoring operation Q1 will switch on for short time periods causing a current to flow through the winding in a positive direction via Q3. During the off period of Q1 the current will decay via the freewheel loop Q3 and D4. If, however, during that half cycle the motor were to start regenerating, the current through the winding would immediately change direction and regenerate into the supply through diodes D1 and D3. The current would decay but more energy can be obtained by shorting out the windings for a period and then again allowing it to regenerate through D1 and D3. The motor is magnetized during the time it is connected to the battery. Because the motor is rotating at a low speed, it is necessary to short the winding for a longer time than the regenerative period. Q4 serves this purpose and provides a freewheel path via D3 for the transfer of energy from the rotor to the stator leakage reactance, which is seen as an increase in stator phase current. Figure 2.2b indicates this sequence with the aid of an equivalent circuit.

Conversely, at higher speeds the mark-space ratio would be high, e.g. 8/9, and during regen. the freewheel or shorting periods would be respectively short.

If the motor continues regenerating into the second half of the cycle, Q2 and Q4 switching on will cause a reverse voltage to be placed across the winding, thus causing the current to again invert and now flow in the positive direction. From figure 2.2a it can be seen the Q2, Q3 and Q4 are now the operating transistors and regeneration will now take place through diodes D2 and D4.

CHAPTER 3

The Test Motor.

3.1 Calculation of machine winding parameters.

The motor used to perform the test described in this chapter was originally a standard GEC, 3 phase, 15 Kw, squirrel cage induction motor. It has 54 slots and was wound to give 6 poles and therefore a synchronous speed of 1000 rpm at 50 Hz. Its chording factor was given as 0.94, which means that each phase winding was chorded down from 9 to 7 slots. The spread of each phase winding was over 3 slots, giving, a spread factor of 0.955. Appendix B.3 shows the winding arrangement. The machine specifications gave the number of turns per coil as 14, for 380 volt, delta connection, with a maximum phase current of 35 amps.

The maximum no-load flux per pole can be derived using the following formula (13);

$$\text{Emf/pole-pair/phase, } E = 4.44 f N' \Phi_m g K \qquad (3.1)$$

where
- N' = conductors per slot
- $N = N'/2$ = turns per coil (for a double layer winding)
- f = frequency
- Φ_m = maximum no-load flux per pole
- g = coils/pole-pair/phase
- $K_\omega = K_s . K_c$
- K_s = spread factor
- K_c = chording factor

Therfore;

$$380/3 = 4.44 \times 50 \times (2 \times 14) \times \Phi_m \times 3 \times 0.955 \times 0.94$$

$$\Phi_m = 7.56 \times 10^{-3} \text{ Webers}$$

The winding parameters of a 9 phase 6 pole motor can now be determined. So as to avoid unwanted space harmonics, each coil's pitch was set at 180 deg. (electrical), that is, the chording factor is unity. For a 6 pole 54 slot machine the spread factor will also be unity. The winding arrangements for the 9-phase machine are shown in appendix B.4. The dc voltage obtained from the battery source is 72 volts, thus giving, for a quasi-square wave with freewheel angle of 31.4 degree (see section 6.2), a fundamental harmonic voltage of 62.4 volts rms. If 60 volts rms is taken as the optimum voltage at 50 Hz, that is, at a rotational speed of 1000 rpm, the last calculation can be performed in reverse to give the number of turns necessary to correctly flux the machine. Therefore:

$$60/3 = 4.44 \times 50 \times (2 \times N) \times 7.56 \times 10^{-3} \times 1 \times 1 \times 1$$

number of turns N = 6

3.2 Modified test motor specifications.

The specifications for the new machine can now be written:

Make of motor	GEC - DZ180L frame	
Speed (sync)	1000 rpm at 50 Hz	
Power rating	15 KW	
No. of slots	54	
No. of poles	6	
Skew	1:54	
	9-phase	3-phase
Chording factor	1	1
Spread factor	1	0.960
Slots/pole/phase	1	3

3.3 Motor equivalent circuit.

Open and short circuit tests (ref D.4) were performed with the motor excited by 3-phase pure sinusoidal waveforms. These tests were done at 5,10,20,40 and 50 Hz to determine the linearity of the equivalent circuit over this frequency range. Referring to the results in figure 3.1, the primary and secondary referred inductance L_1+L_2' and the magnetizing inductance L_m remain fairly constant over the range with deviations from their mean values of 14% and 7% respectively. The equivalent iron loss resistance R_m, however, varies by a factor of more than 20 over the operating range and the referred rotor resistance R_2' by a factor of 3.

The variation in R_m indicates that the iron losses are approximately inversely proportional to the frequency between 20 and 50 Hz. However, below 20 Hz this relationship does not apply and as frequency is reduced towards 5 Hz the iron losses become disproportionately larger. The variation in R_2' is probably a result of reduced transformer action between stator and rotor windings/bars at low frequencies and the value determined for low frequencies is probably incorrect.

The determination of equivalent circuit values by actually measuring each harmonic quantity supplied to a quasi-square wave excited machine provides another view. Figures 3.2 and 3.3 show the results of these tests at fundamental frequencies of 20 and 40 Hz. Table 3.1 compares the fundamental frequency equivalent circuit values to the values obtained in the 3-phase sine wave tests.

Table 3.8 overleaf gives the equivalent circuit comparisons for the 9-phase quasi-square wave excited motor and the 3-phase sine wave excited motor. Note that the 3-phase values have been divided by 3 because a 3-phase winding is made up of 3 9-phase windings. This is not entirely valid due to the different winding configuration, magnetic coupling, etc., but will suffice for a general overview.

freq Hz	Vph rms
5	18
10	36
20	72
40	144
50	180

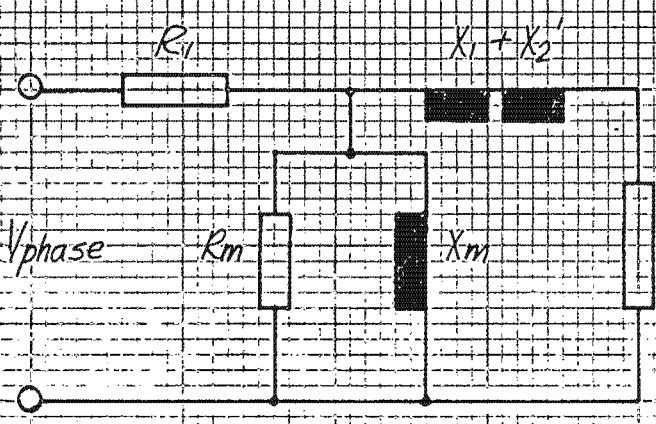

3-Phase sinusoidal equivalent circuit

	R_1 Ω	R_m Ω	R_2' Ω	X_1+X_2' Ω	L_1+L_2' mH	X_m Ω	L_m mH
5 Hz	0·174	2·82	0·082	j0·143	4·55	j0·775	24·7
10 Hz	0·174	7·81	0·103	j0·208	3·31	j1·410	22·4
20 Hz	0·174	22·9	0·116	j0·442	3·52	j2·590	20·6
40 Hz	0·174	57·6	0·220	j0·825	3·29	j5·360	21·3
50 Hz	0·174	60·0	0·257	j1·008	3·21	j6·473	20·6

Figure 3.1 Equivalent circuit of motor when connected for 3-phase operation and excited with pure sinusoidal waveforms. (ref D.4)

harm.	Vin rms
1	17.1
3	5.1
5	2.5
7	0.9

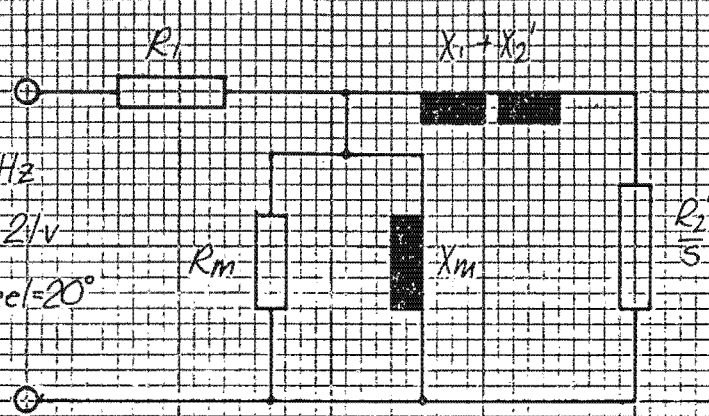

9 Phase quasi-square wave equivalent circuit

	R_1 Ω	R_m Ω	R_2' Ω	X_1+X_2' Ω	L_1+L_2' mH	X_m Ω	L_m mH
Fundamental 20Hz	0.058	10.44	0.045	j0.123	0.97	j1.46	11.6
3rd harm. 60Hz	0.058	3.09	0.080	j0.797	2.11	j0.53	1.40
5th harm. 100Hz	0.058	2.40	0.273	j2.940	4.68	j0.48	0.76
7th harm 140Hz	0.058	7th harmonic regeneration occuring					

Figure 3.2 Equivalent circuit of motor when connected for 9-phase operation and excited with 20 Hz quasi-square waves. (ref D.11.1) Harmonic analyzer was used to determine circuit parameters.

harm.	Vin rms
1	36v
3	10.3v
5	4.7v
7	1.6v

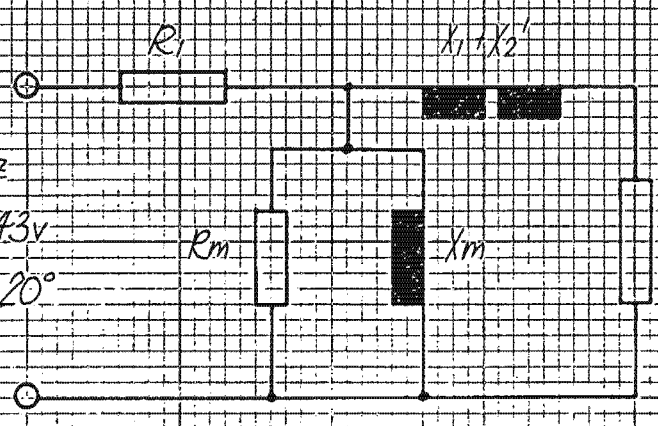

9-Phase quasi-square wave equivalent circuit

	R_1 Ω	R_m Ω	R_2' Ω	X_1+X_2' Ω	L_1+L_2' mH	X_m Ω	L_m mH
Fundamental 40Hz	0.058	18.30	0.044	j0.279	1.11	j2.78	11.06
3rd harm. 120Hz	0.058	11.92	0.065	j1.556	2.06	j1.03	1.36
5th harm. 200Hz	0.058	5.42	0.174	j5.126	4.08	j1.07	0.85
7th harm. 280Hz	0.056	7th	harmonic	regeneration	occurring		

Figure 3.3 Equivalent circuit of motor when connected for 9-phase operation and excited with 40 Hz quasi-square waves. (ref D.11.2) Harmonic analyzer was used to determine circuit parameters.

Table 3.8.

9-phase fundamental quasi-square wave and 3-phase sinusoidal equivalent circuit comparisons.

	Freq.= 20 Hz		Freq.= 40 Hz	
	Modified 3-phase	Fundamental 9-phase	Modified 3-phase	Fundamental 9-phase
R_1	0.058	0.058	0.058	0.058
R_m	7.63	10.44	19.2	18.3
R_2'	0.039	0.045	0.073	0.044
X_1+X_2'	0.148	0.123	0.275	0.279
L_1+L_2'	1.17	0.97	1.097	1.110
X_m	0.86	1.46	1.79	2.78
L_m	6.87	11.6	7.10	11.06

The values compare favourably except for X_m and L_m, which, because of the form of magnetizing current developed by the quasi-square voltage excitation, will be erroneous for 9-phase values.

CHAPTER 4.

The Bridge Inverter Power Unit.

4.1 Bridge inverter operation.

All 9 bridge inverters are supplied from the same D.C. supply rail which is kept constant at 72 volts (i.e. simulating 6 x 12v batteries in series) or in fact any other voltage depending on the particular experiment. The bridge inverter circuit diagram is shown in figure 4.1a. As stated, the saturated gain of the transistors Q1 - Q4 is approximately 10, requiring a base drive current of 10 amps for a maximum collector current of 100 amps. The base drive inverters, whose on/off state is dependent on the status of the signal lines S1, S2, S3 and S4, provide the relatively high current at a low voltage. Figure 4.1b shows typical switching signals, as well as the resulting output waveform. Freewheel diodes are placed across each transistor, as well as snubber networks (RCD), which provide an alternative current path when the transistor switches off. A full design analysis is given in reference 8 and it has therefore not been considered necessary to delve too deeply into the design criteria aspect of the system.

The operation of the bridge inverter when supplying quasi-square waves is as follows:-

With reference to figure 4.1, when signal lines S1 and S3 switch high, Q1 and Q2 switch on, and allow current to flow through the winding in a positive direction. The ability of the bridge to freewheel is essential to realize quasi-square waves. Therefore, after a set time, in this example's case 51/126 of the cycle time, Q1 is switched off and as a result of the inductive nature of the winding the current will not cease to flow immediately, but will circulate through the components Q3 and D4. The voltage developed across the winding when Q1 and Q3 are on is $Vdc-(2 \times Vce_{sat})$ and when Q1 switches off it will be Vce_{sat} + Vdiode which is effectively zero.

To allow a safety margin between Q3 switching off and Q2 and Q4 switching on

Figure 4.1a Power switching bridge inverter circuit diagram.

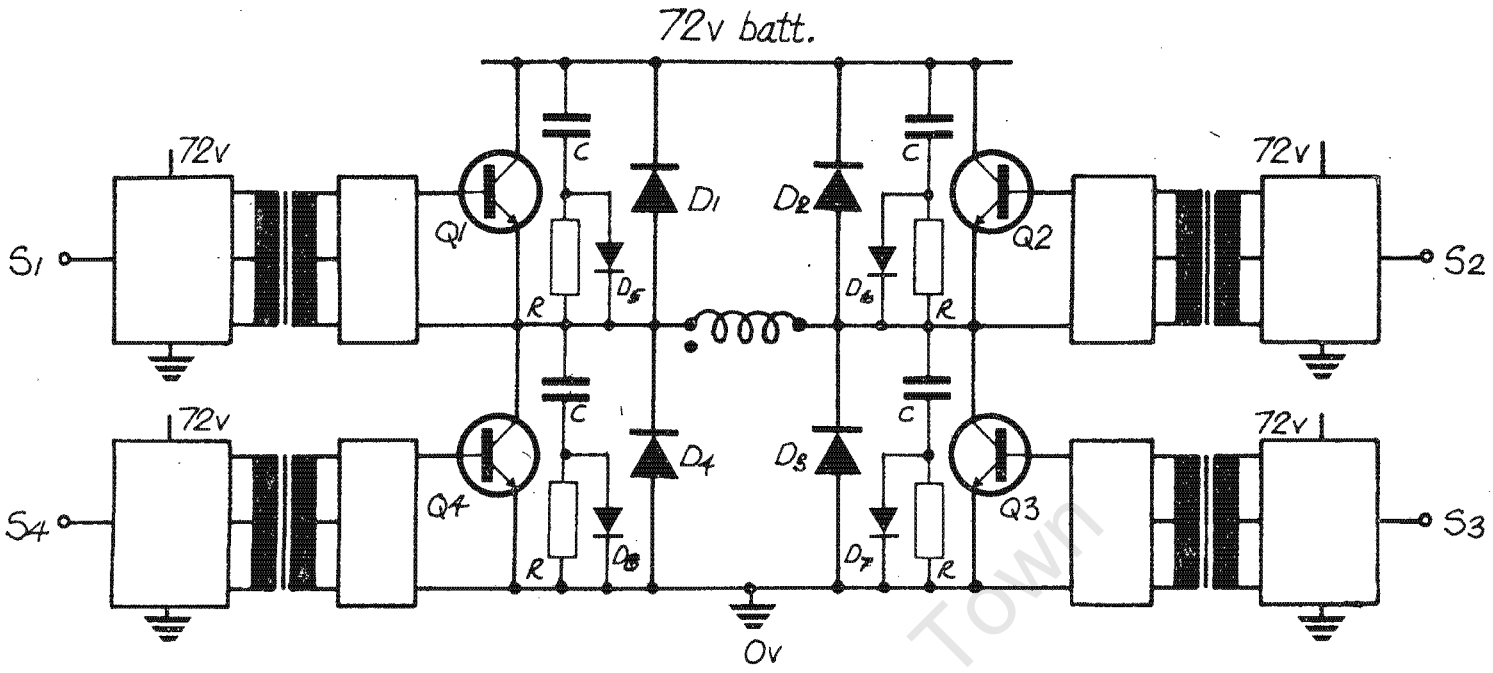

Figure 4.1b Switching signals of bridge inverter.

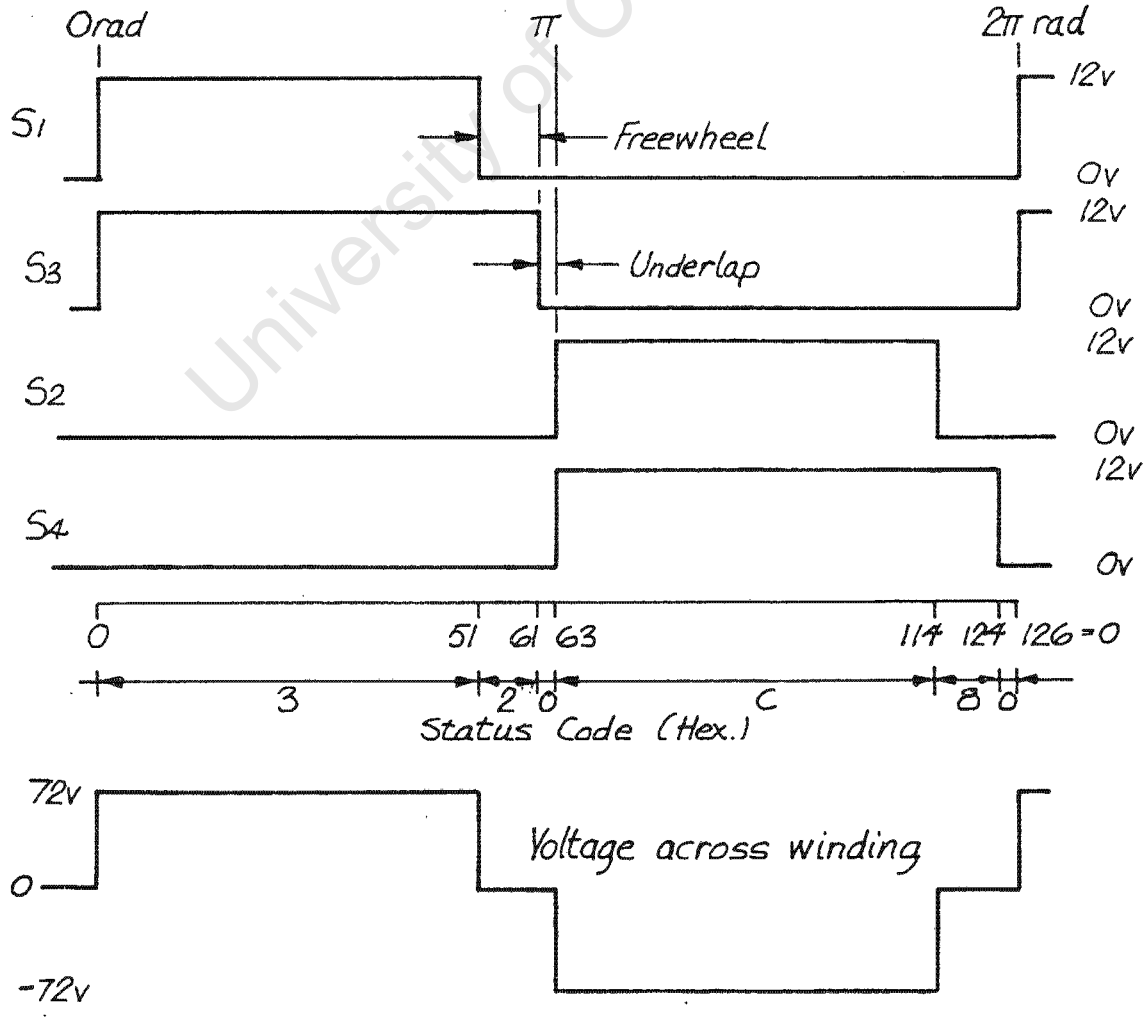

VOLTAGE AND CURRENT WAVEFORM DURING 1Hz LOCKED ROTOR TEST. NOTE LOW VOLTAGE DURING UNDERLAP REGENERATION

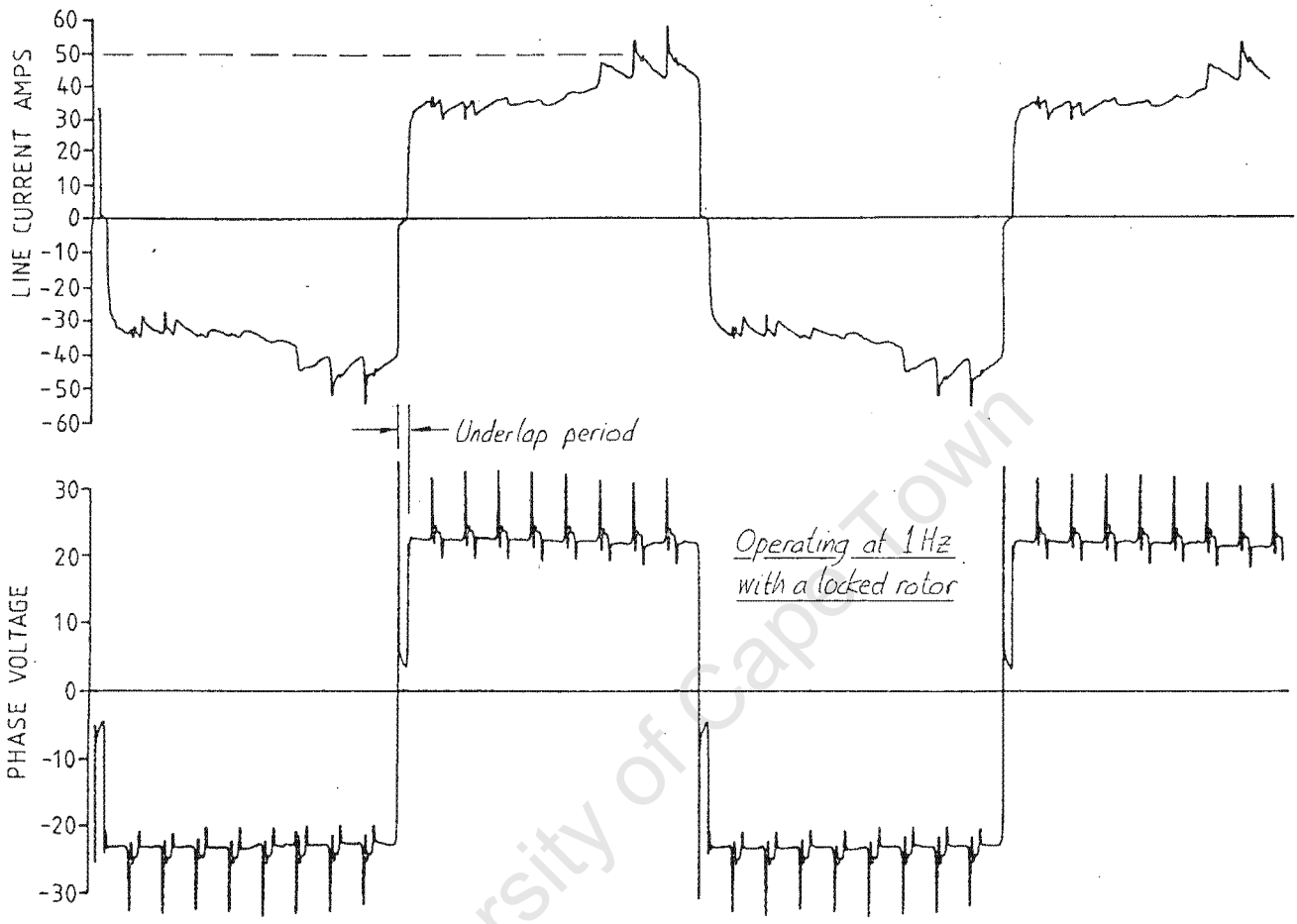

FIG 4.2a

VOLTAGE AND CURRENT WAVEFORM DURING 50 Hz NO-LOAD TEST. NOTE HIGHER VOLTAGE DUE TO DIODE VOLTAGE DROPS DURING UNDERLAP REGENERATION

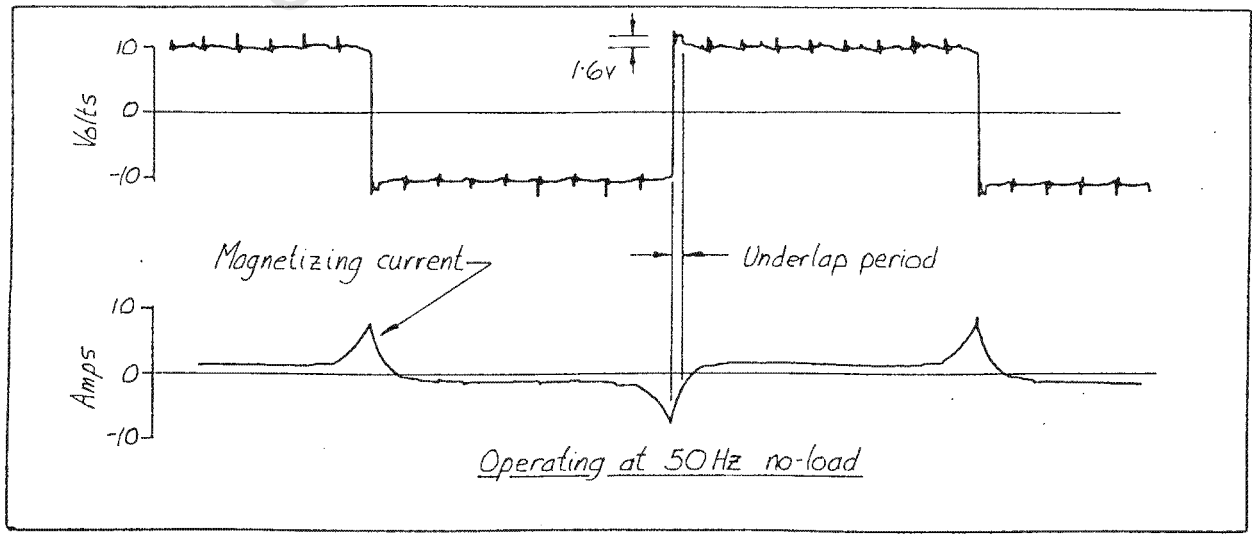

FIG 4.2b

SWITCHING CHARACTERISTICS OF THE ESM 1000 POWER SWITCHING TRANSISTOR IN LOADED AND NO-LOAD CONDITION

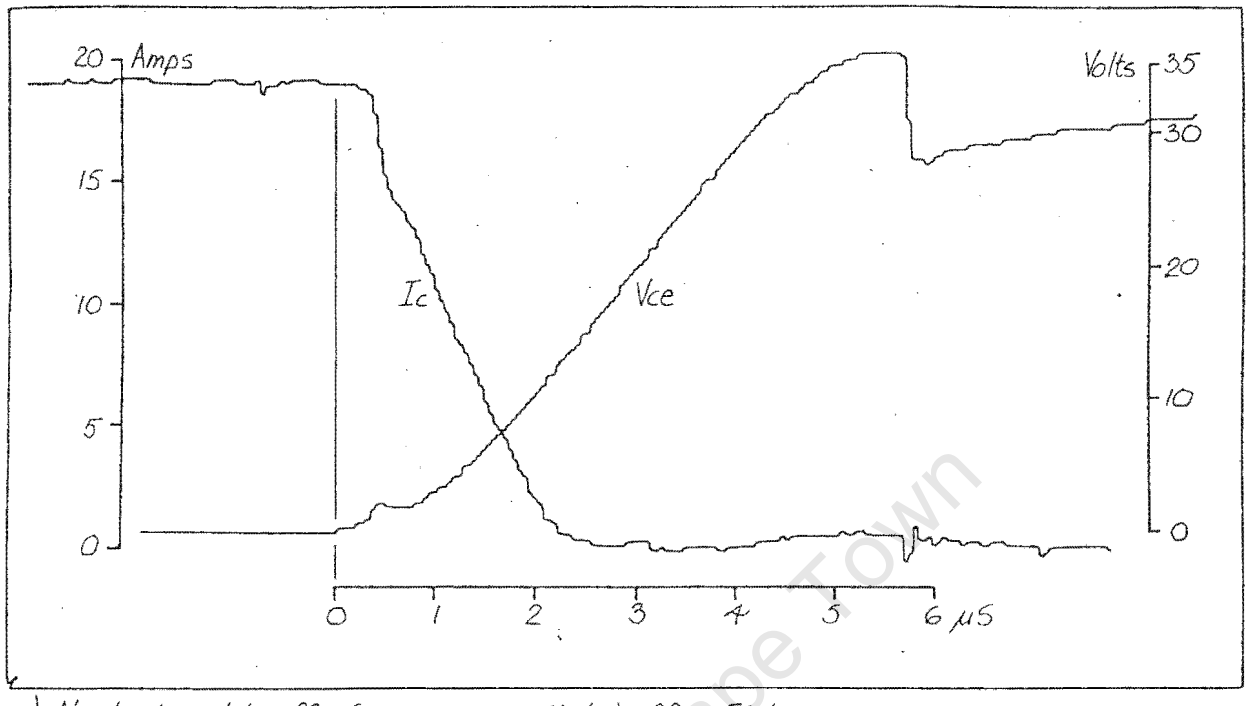

a) No-load switch-off of ESM1000, Vdc(in) = 22v, 50Hz.

FIG. 4.3a

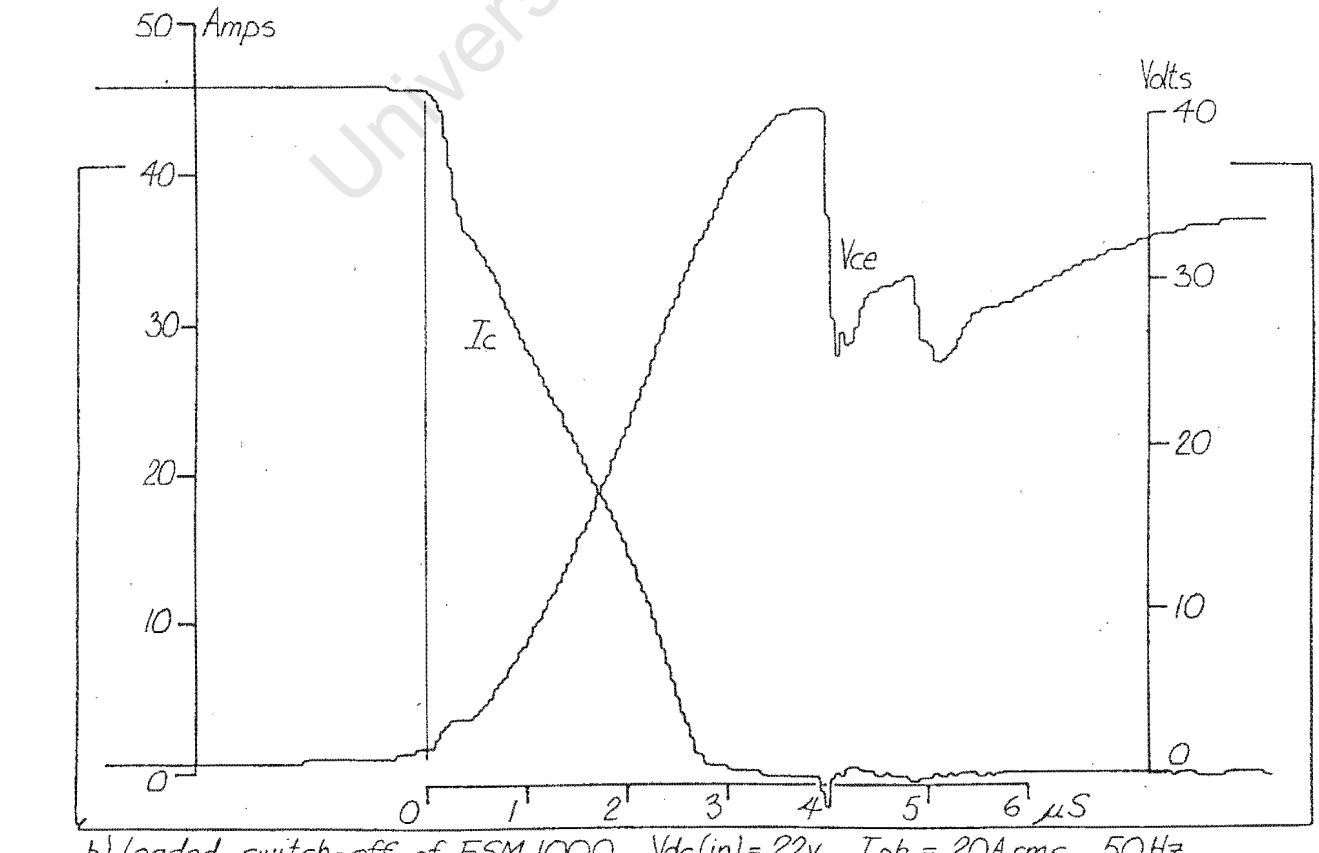

b) Loaded switch-off of ESM 1000, Vdc(in) = 22v, Iph = 20A rms, 50Hz.

FIG 4.3b

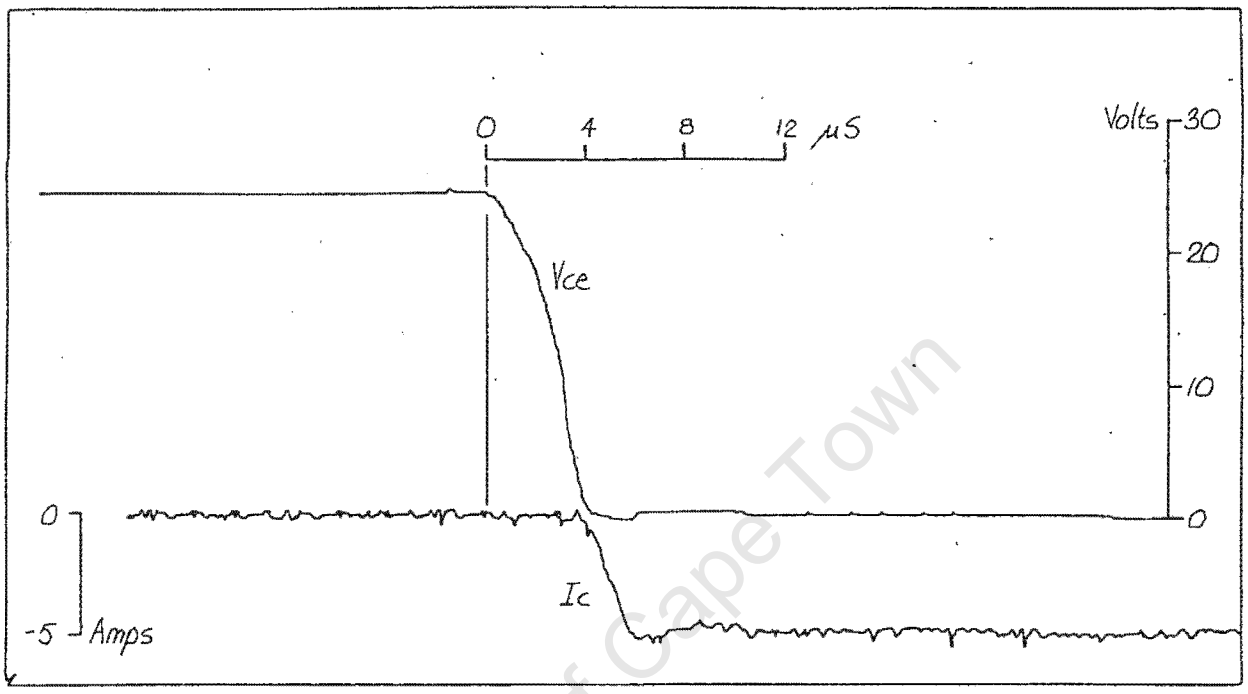

c) No-load switch-on of ESM 1000 , Vdc (in) = 22v , 50 Hz.

FIG 4.3c

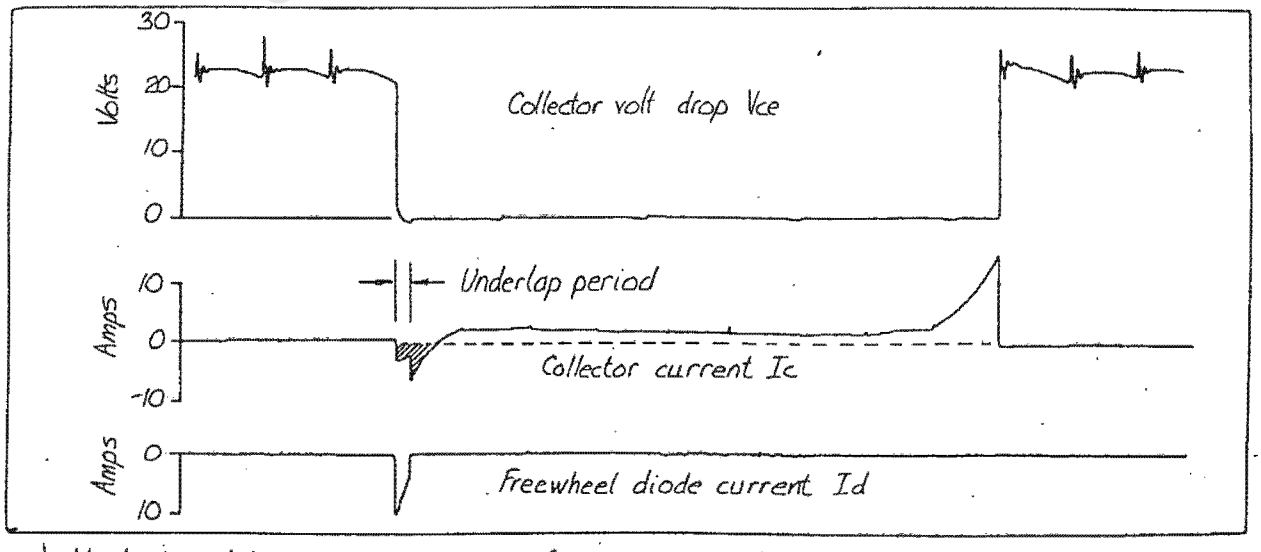

d) No-load switching characteristics of ESM 1000 with Vdc = 22v.

FIG 4.3d

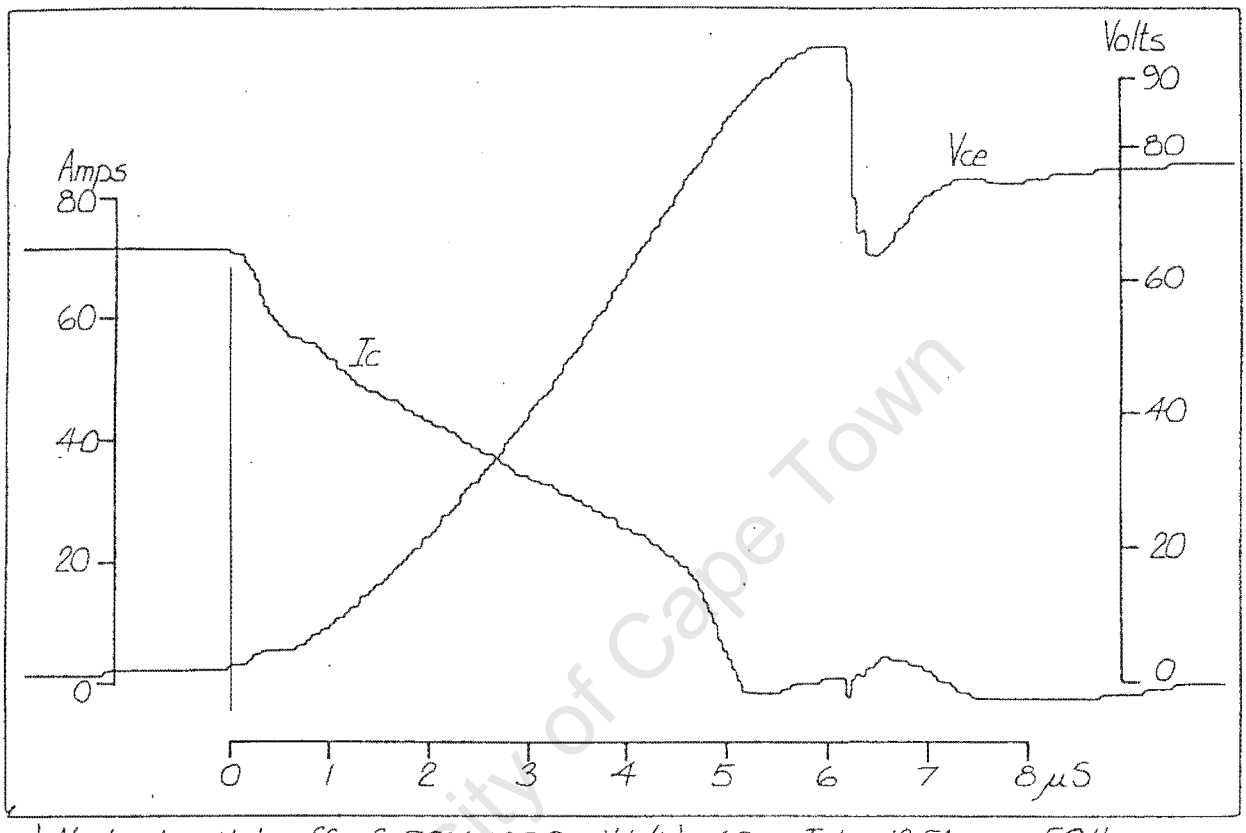

e) No load switch-off of ESM 1000, Vdc(in) = 60v, Iph = 13·5A rms, 50Hz.

FIG 4.3e'

at the end of half a cycle, a short underlap period is introduced. During the underlap period all the transistors are off, and if there is still current circulating through the phase winding in the positive direction, regeneration back into the supply will occur through D2 and D4. This will normally happen for all frequencies above 10 Hz and will cause the voltage across the phase winding to invert to -(Vdc + 2Vdiode). The waveform example shown in figure 4.1b is for a lower frequency than 10 Hz.

At the end of the underlap period Q2 and Q4 switch on and immediately the current flowing through the winding will start to decrease and reverse with the voltage impressed upon it being -(Vdc - 2Vdiode). After a short time the current will flow in the negative direction. The same switching procedure is repeated at the end of the cycle, but now Q2 switches off first and allows freewheel through Q4 and D3. This is followed by another short period of underlap during which current is again regenerated back into the supply through diodes D1 and D3.

Figures 4.2a & b show recordings of current and voltage waveforms at 1 Hz and 50 Hz with a zero freewheel angle for a double cage induction motor which was investigated initially. Note the regenerative voltage at 1 Hz and 50 Hz during underlap.

Figures 4.3a,b,c,d & e show the switching signals across the ESM 1000 power switching transistor under loaded and no-load conditions. Figures 4.3a,b,c & d are shown with supply voltage set at 22vdc, whereupon 4.3e has the supply voltage set at 60vdc. Comparing 4.3a and 4.3e indicates the effect that the increase in supply voltage has on the switching times. As will be shown later, the magnetizing peak current is related linearly to the supply voltage (saturation neglected) and the maximum current indicated in figures 4.3a,b,c & e is in fact a peak as shown in figure 4.3d. The overlap of current and voltage during switch-off has been optimized with the use of a snubber network. It should be remembered that the snubber network will discharge when the transistor switches on again, which can cause a current spike through the transistor, thus the reason for optimization and not minimization. If, as is the actual case, the quasi-square waveform is chopper modulated at 1.2 KHz, the switch-off losses in the transistor can be calculated. Using the waveform of figure 4.3e it was calculated that the switching losses at no-load would be approximately 3 watts. On load this

will probably rise to approximately 4.5 watts per ESM 1000 transitor.

Figure 4.3d shows that the ESM 1000 operates effectively in the reverse bias mode. During underlap when all transistors are off, the diode adjacent to the transistor under consideration conducts the regenerative current back into the supply. More importantly, even though the base drive current is off, the transistor still conducts a proportion of the regenerative current from emitter to collector. It should be noted, however, that the diode in its conducting condition is actually causing a reverse bias to be placed across the collector-emitter junction of the ESM 1000. As soon as the base signal appears, the transistor takes up the full current in the reverse direction and continues to conduct it until it decays through zero and reverts to the normal collector to emitter flow.

The usual transistor construction allows for a larger base-emitter region than base-collector region to cope with the current ib + ic. However, the ESM 1000 appears to be operating in this inverted manner quite successfully. The ESM 1000's emitter geometry is a star pattern with the emitter lug welded at the centre of the star. This pattern maximizes the emitter periphery and reduces $V_{ce\,sat}$ and probably as a result of its diffused planer construction, also allows large reverse currents to flow.

4.2 Base drive inverter.

As a result of the power switching transistors in the bridge inverter all being NPN type, it becomes necessary to provide floating drives for their bases. Figure 2.1a shows that the emitter junctions of Q1 and Q2 do not remain at a fixed potential, but vary between zero and Vdc volts.

To provide the required isolation and driving capability, a self-driven oscillator is used (see figure 4.4). Its on/off control is via the field effect transistor T3 switching the oscillators supply line on and off. The oscillator runs at approximately 25KHz and has a measured efficiency of 69.5% with 9.5 amps (mean) base drive current flowing. The total power loss in each oscillator is approximately 13.6 Watts with a third of that, i.e.

4.5Watts, lost in the secondary rectifying diodes. By using Schottky diodes, the latter loss can probably be halved.

With the advent, however, of more powerful FET's, which can replace the ESM1000 power transistors used at present, direct drive using opto-isolating techniques will be possible. This will result in minimal power loss in the driving circuit.

Figures 4.6a,b and c show the collector voltage and current waveforms developed in the self driven oscillator when approximately 9.4 amps are drawn from the secondary. An increase in load current through the ESM1000 power transistor does not change the relative levels of the waveforms noticeably, but does cause the oscillator frequency to increase very slightly.

Figures 4.7a and b show the voltage applied across the base emitter junction of the ESM1000 transistor and the current into its base. The saturated gain of the ESM1000 is 10. The drop in base current, resulting from the inverter and rectifying diodes switching characteristics, does not, in fact, affect the current carrying capabilities of the ESM1000 to any extent because of the base-emitter capacitance. As a result of the waveshape of the motor load current, the maximum rms current usually drawn is around 50 amps with only the magnetizing current peak exceeding this for short periods. Thus, only during brief periods of the current waveform's cycle will there be additional power loss in the ESM1000.

4.3 Reduction in base drive current.

As a result of the large losses occurring because of the 10 amp base drive current requirement, it was decided to study the effects on the ESM 1000 power transistor when this current was reduced to 5 amps.

Figures 4.8a,b,c and d show the effect on the base-emitter voltage drop Vbe for a reduced drive current. The voltage increase across the base-emitter junction for a collector current of 90 amps is 0.23 volts and 0.25 volts for 5 amp and 10 amp drives respectively. The power loss in the base-emitter junction of the ESM 1000 at 5 amp drive will be approximately

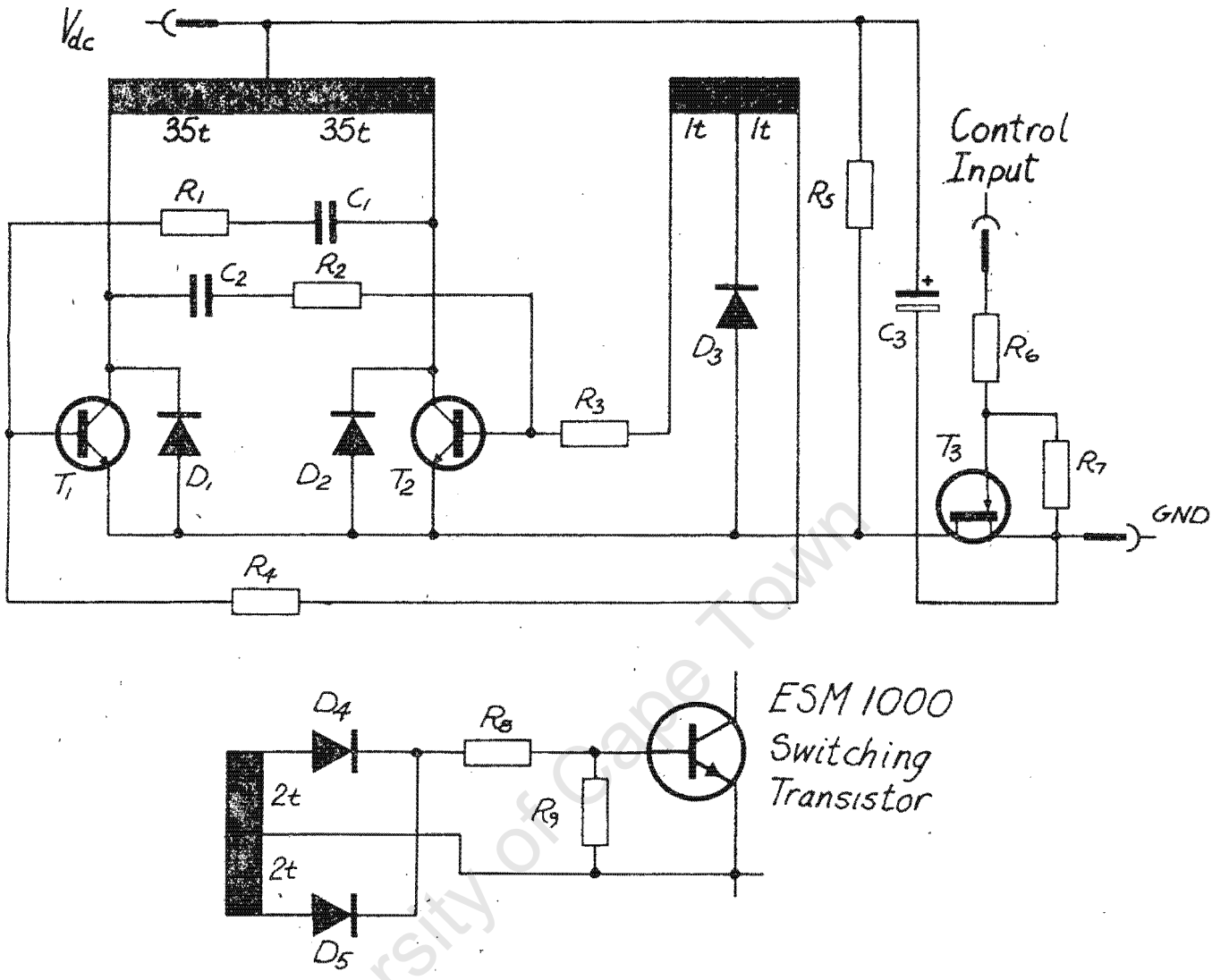

Winding data: Primary 2x35 turns x 3 strands. 0.125mm dia.
Secondary 2x2 turns x 20 strands, 0.224mm dia.
Feedback 2x1 turn x 1 strand, 0.125mm dia.
Transformer ferroxcube pot core type FX2240

Components:

T_1, T_2 - TIP49 (350v, 1A)	
T_3 - BUZ30 (200v, 4.5A)	
D_1, D_2, D_3 - MR816	D_4, D_5 - MR822
R_1, R_2 - 1K5 $\frac{1}{2}$W	R_3, R_4 - 15 $\frac{1}{4}$W
R_5 - 270K $\frac{1}{4}$W	R_6 - 150 $\frac{1}{4}$W
R_7 - 150K $\frac{1}{4}$W	R_8 - 0.38 (31.8cm x 22SWG Eureka wire)
R_9 - 0.68 2W	
C_1, C_2 - 1nF	C_3 - 4.7uF (100v electrolitic)

Figure 4.4 Floating base drive circuit diagram.

FIG. 4.6

SWITCHING DETAILS OF THE BASE DRIVE INVERTER SWITCHING TRANSISTORS T1 & T2

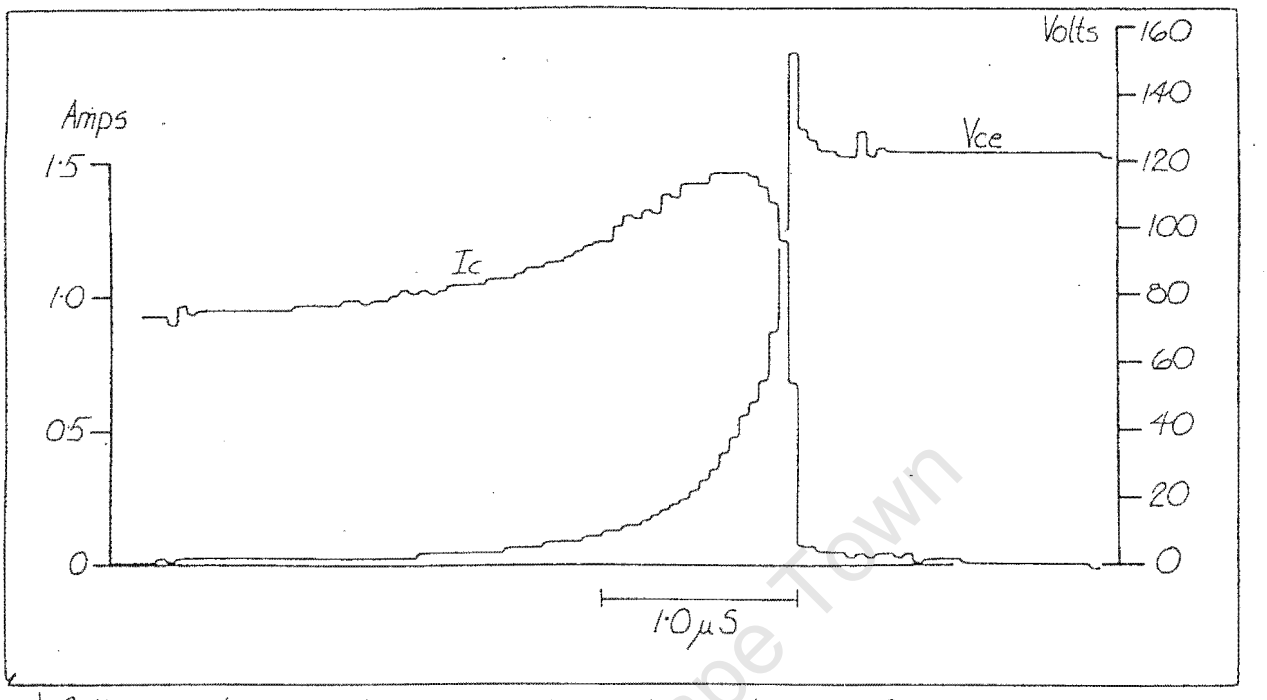

a) Collector voltage and current – transistor switching off

FIG 4.6a

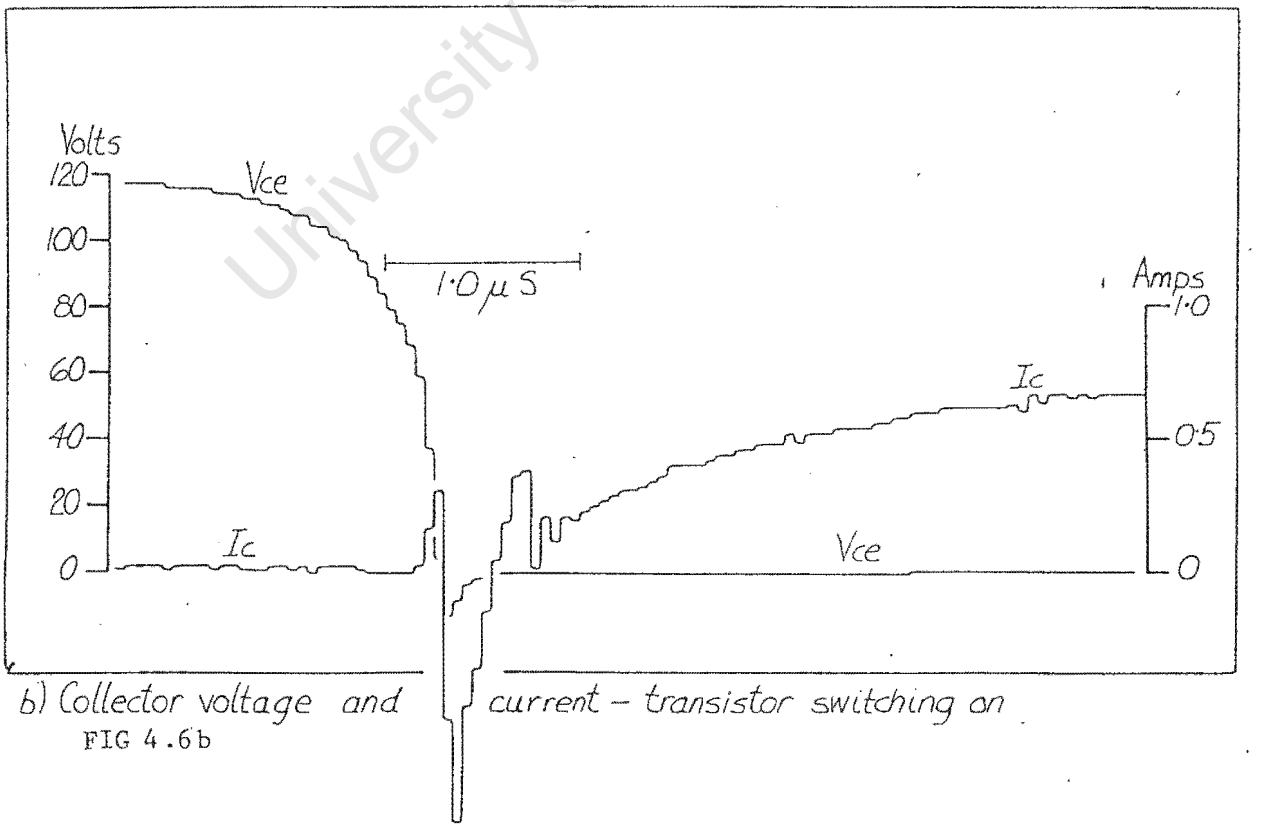

b) Collector voltage and current – transistor switching on

FIG 4.6b

FIG. 4.6

SWITCHING DETAILS OF THE BASE DRIVE INVERTER SWITCHING TRANSISTORS T1 & T2

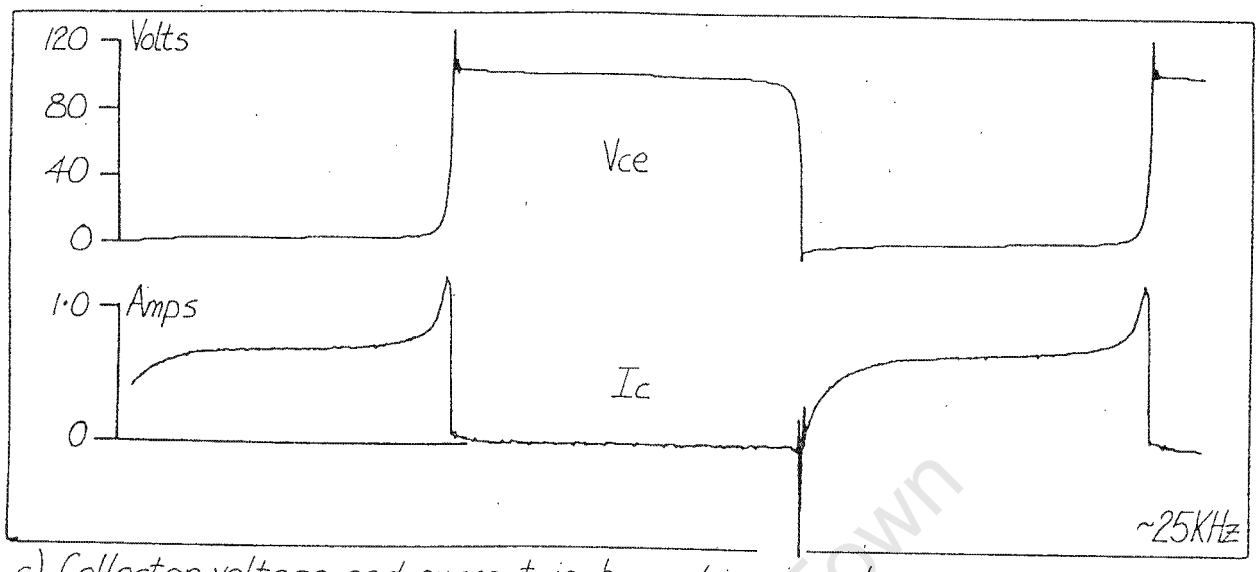

c) Collector voltage and current in base drive inverter

FIG 4.6c

FIG 4.7

VOLTAGE AND CURRENT SUPPLIED BY BASE DRIVE INVERTER TO ESM 1000 POWER TRANSISTORS BASE-EMITTER JUNCTION

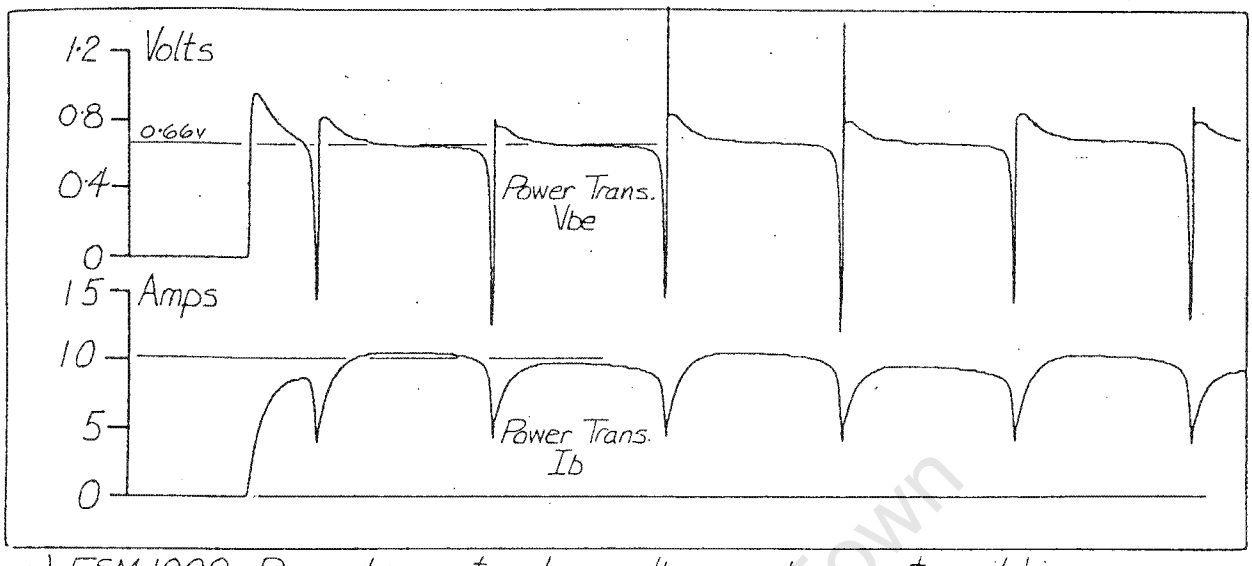

a) ESM 1000 Power transistor base voltage and current - switching on

FIG. 4.7a

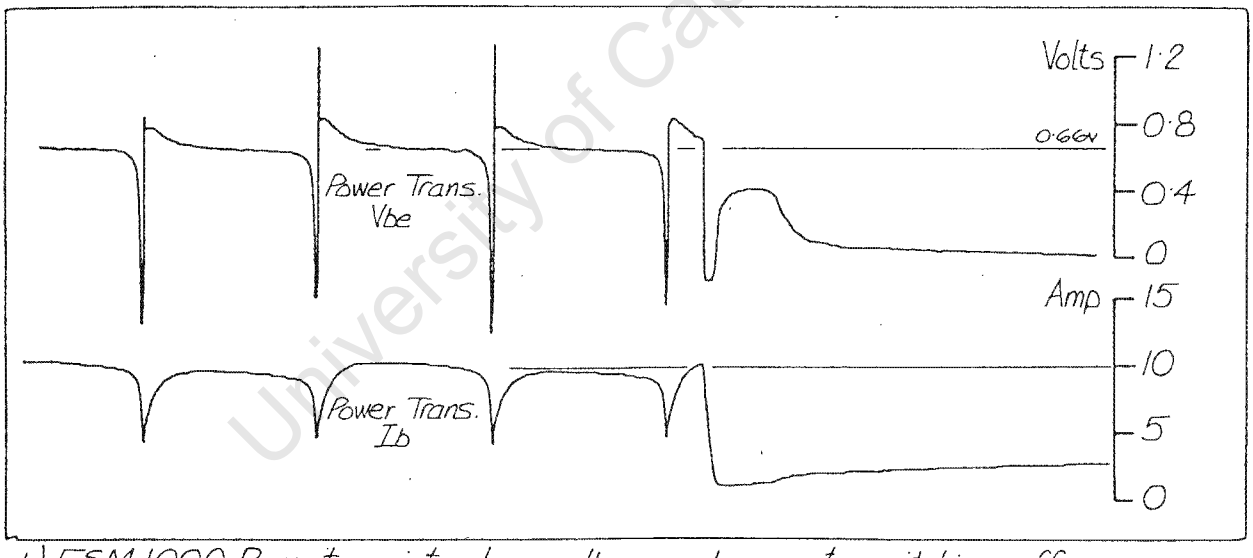

b) ESM 1000 Power transistor base voltage and current - switching off

FIG 4.7b

0.91 x 5 x 0.5 = 2.28 watts against 0.97 x 10 x 0.5 = 4.85 watts for 10 amp drive. The saving in power by decreasing the base drive current by half is 2.6 watts per transistor.

However, as a result of this decreased drive, additional power is lost between the collector-emitter regions during periods of high collector current. Figures 4.9a,b,c,d,e and f show the variation in collector-emitter voltage drop Vce_{sat} for various load currents Ic. The plot of Vce_{sat} is inverted due to the collector junction being used as the reference point. For collector currents of 50 amps or less, there is only a very small difference in Vce_{sat} between the 5 amp and 10 amp driven transistor. The 10 amp driven transistor has a saturated voltage drop which is 0.2 to 0.3 volts less than the 5 amp driven transistor.

For Ic > 50 amps i.e.magnetizing current, that is not the case. During these current excursions, with a 5 amp base drive, the ESM 1000 attempts to limit the collector current. It is at this point that the 25 KHz ripple caused by the base drive waveform (see figure 4.7),is impressed upon the normal saturation voltage waveform as shown in figures 4.9c and e. This in itself is not serious, and experimentally the increased power loss cannot be noticed, due to the reduced base-emitter power drop. However, regions of local heating could possibly form within the transistor, which over a period of time will cause premature failure. Typical figures for power lost in the nine phase bridge inverter are given in section 7.3.

4.4 Switching delays between logic control and power transistor.

Typical switching times are shown in figures 4.10a,b,c and d with the test motor being driven at 50Hz under no-load and loaded conditions. The results show that the switching on time delay increases from 1.9μS to 2.2μS in the loaded condition and the switching off time delay increases from 21μS to 23μS. Approximately 50% of the switching off time delay in both no load and loaded conditions is taken up by the base drive oscillator switching off. The variation in switching delays should not affect the control of the bridge inverter or detract from the interlacing discussed in section 2.4. Problems can be experienced with response times to overload conditions. For normal motor overloads the electronic protection circuit inhibiting the controller

FIG. 4.8

BASE-EMITTER VOLTAGE DROP Vbe OF ESM 1000 SWITCHING TRANSISTOR FOR 5A AND 10A BASE DRIVE CURRENTS AT NO-LOAD i.e. COLLECTOR CURRENT = 0

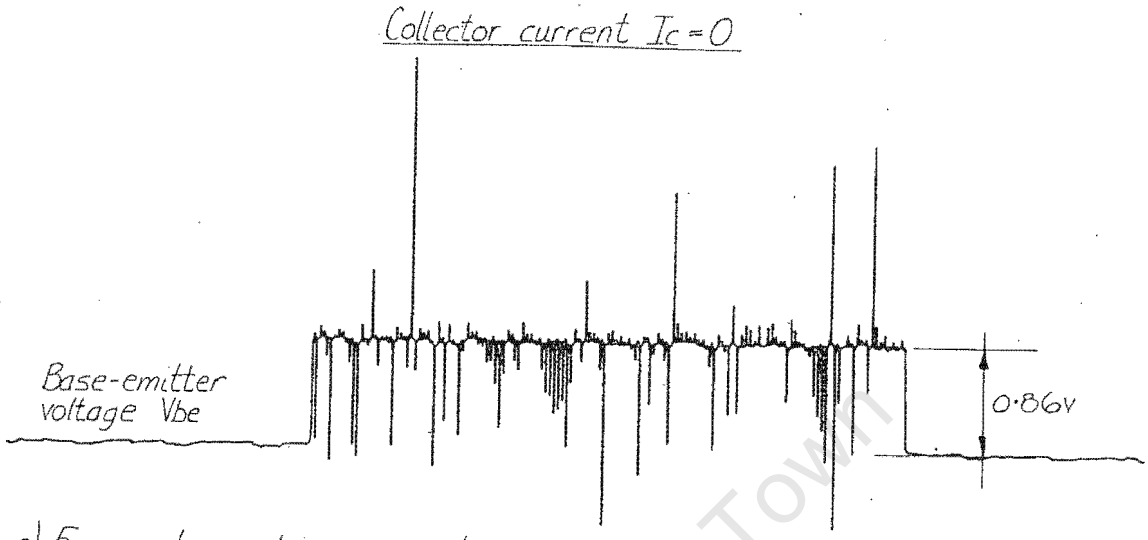

a) 5 amp base drive current

FIG. 4.8a

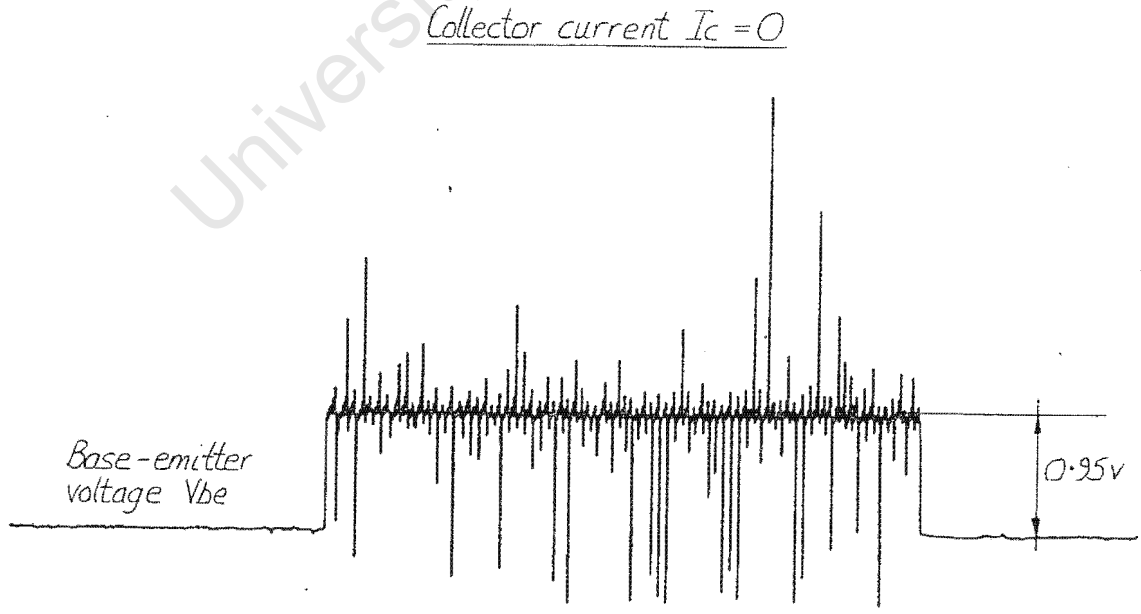

b) 10 Amp base drive current

FIG. 4.8b

FIG. 4.8

BASE EMITTER VOLTAGE DROP Vbe OF ESM 1000 SWITCHING TRANSISTOR FOR 5A AND 10A BASE DRIVE CURRENTS UNDER LOADED CONDITIONS

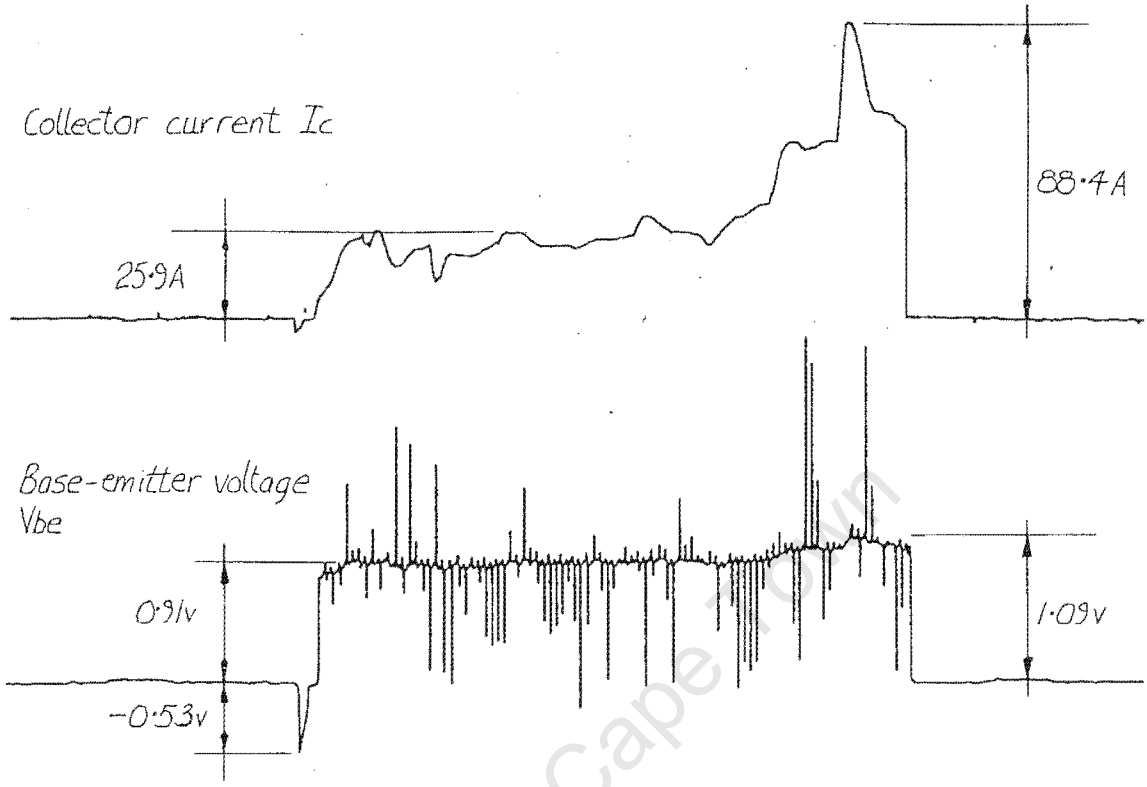

c) 5 amp base drive current

FIG 4.8 c

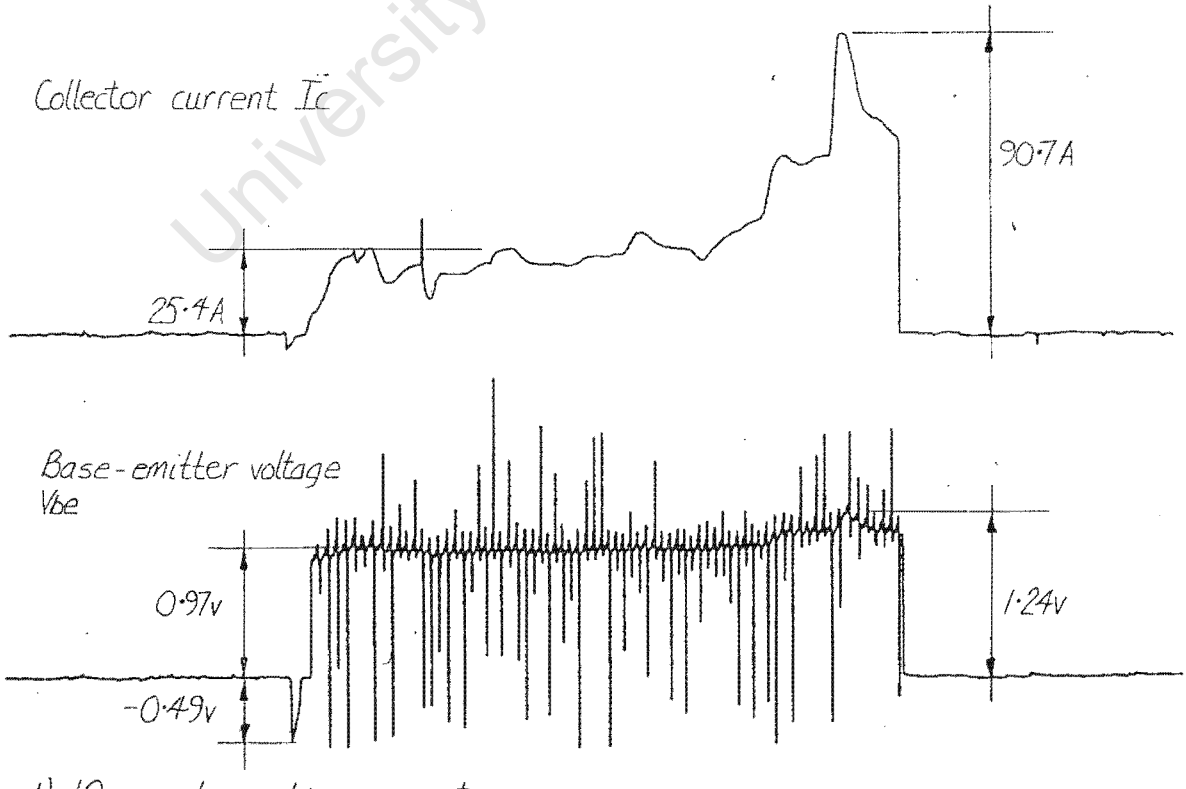

d) 10 amp base drive current

FIG 4.8d

FIG. 4.9

COLLECTOR-EMITTER SATURATION VOLTAGE Vce_{sat} ACROSS ESM 1000 SWITCHING TRANSISTOR FOR BASE DRIVE CURRENTS OF 5A AND 10A

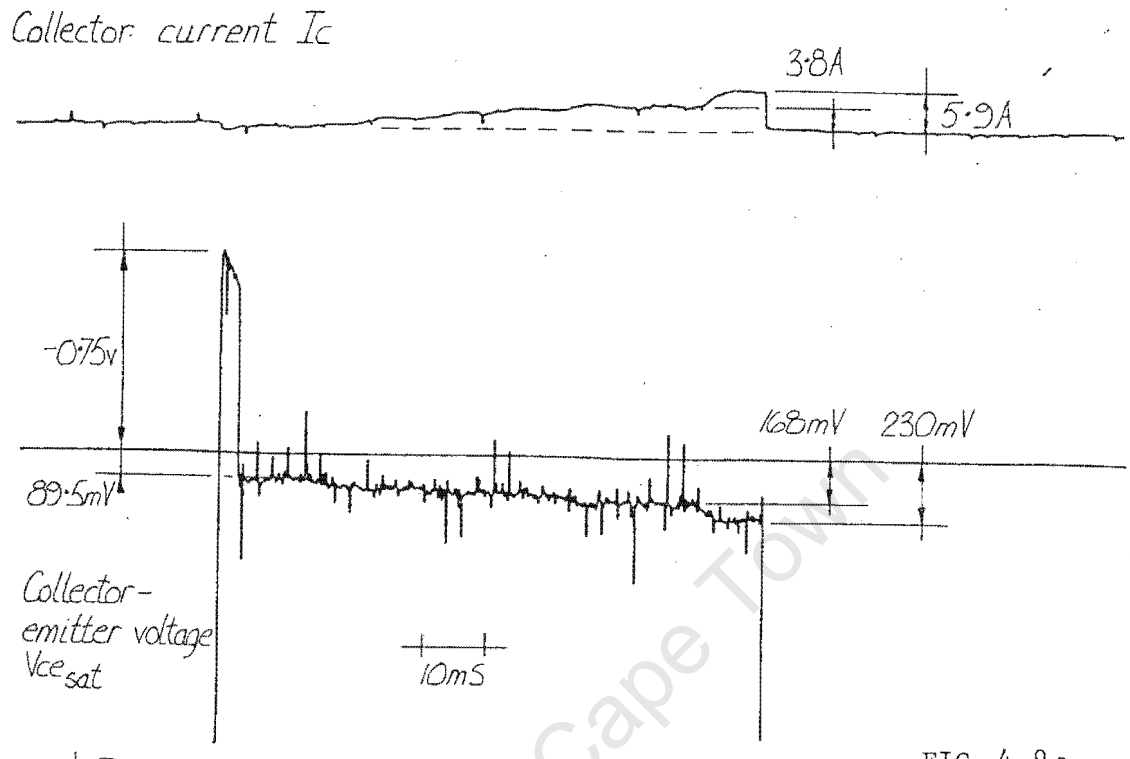

a) 5 amp base drive current

FIG. 4.9a

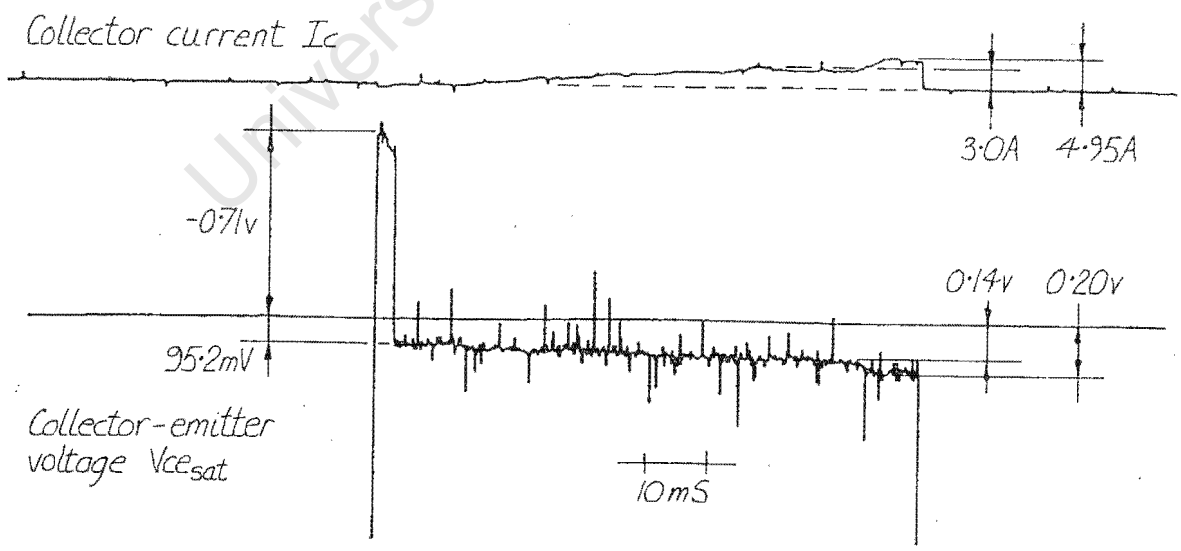

b) 10 amp base drive current

FIG. 4.9b

FIG. 4.9 COLLECTOR-EMITTER SATURATION VOLTAGE Vce_{sat} ACROSS ESM 1000 SWITCHING TRANSISTOR FOR BASE DRIVE CURRENTS OF 5A AND 10A

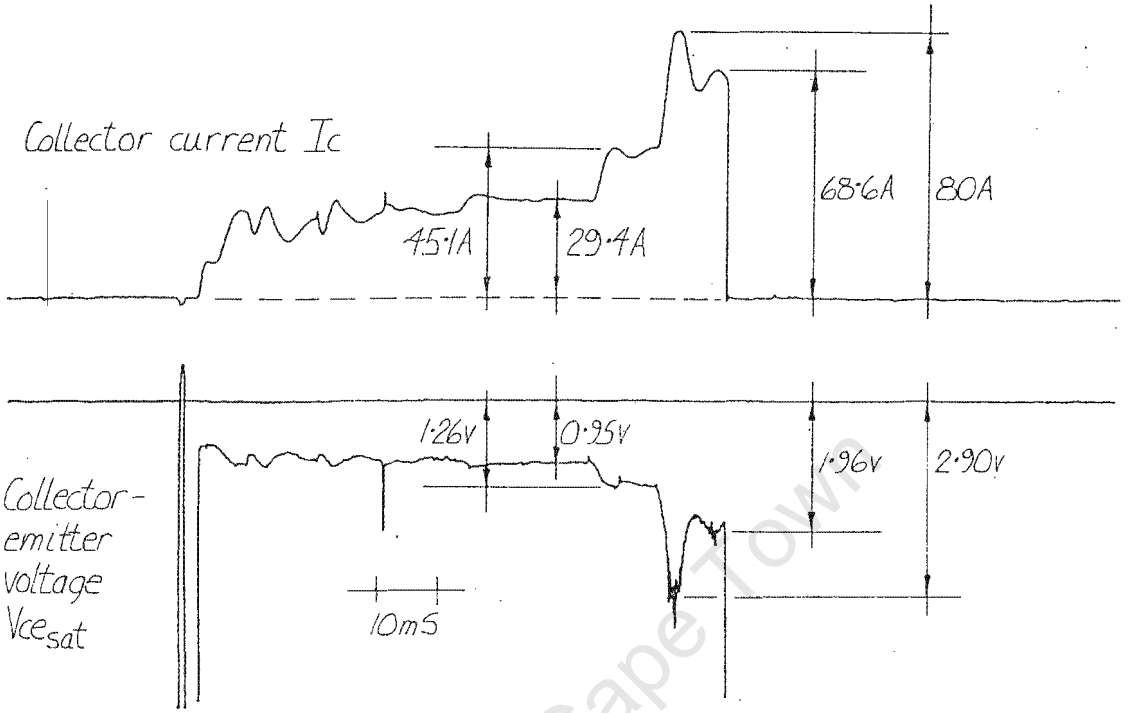

c) 5 amp base drive current

FIG 4.9 c

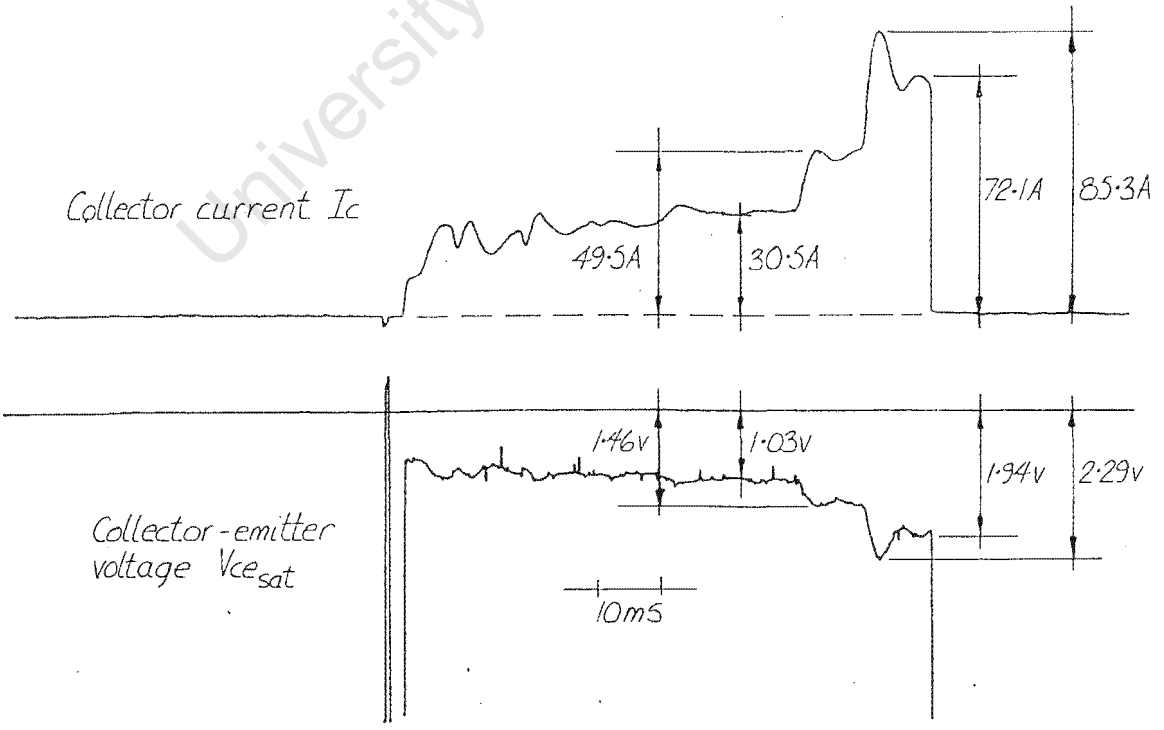

d) 10 amp base drive current

FIG 4.9 d

FIG. 4.9

COLLECTOR-EMITTER SATURATION VOLTAGE Vce_{sat} ACROSS ESM 1000 SWITCHING TRANSISTOR FOR BASE DRIVE CURRENTS OF 5A AND 10A

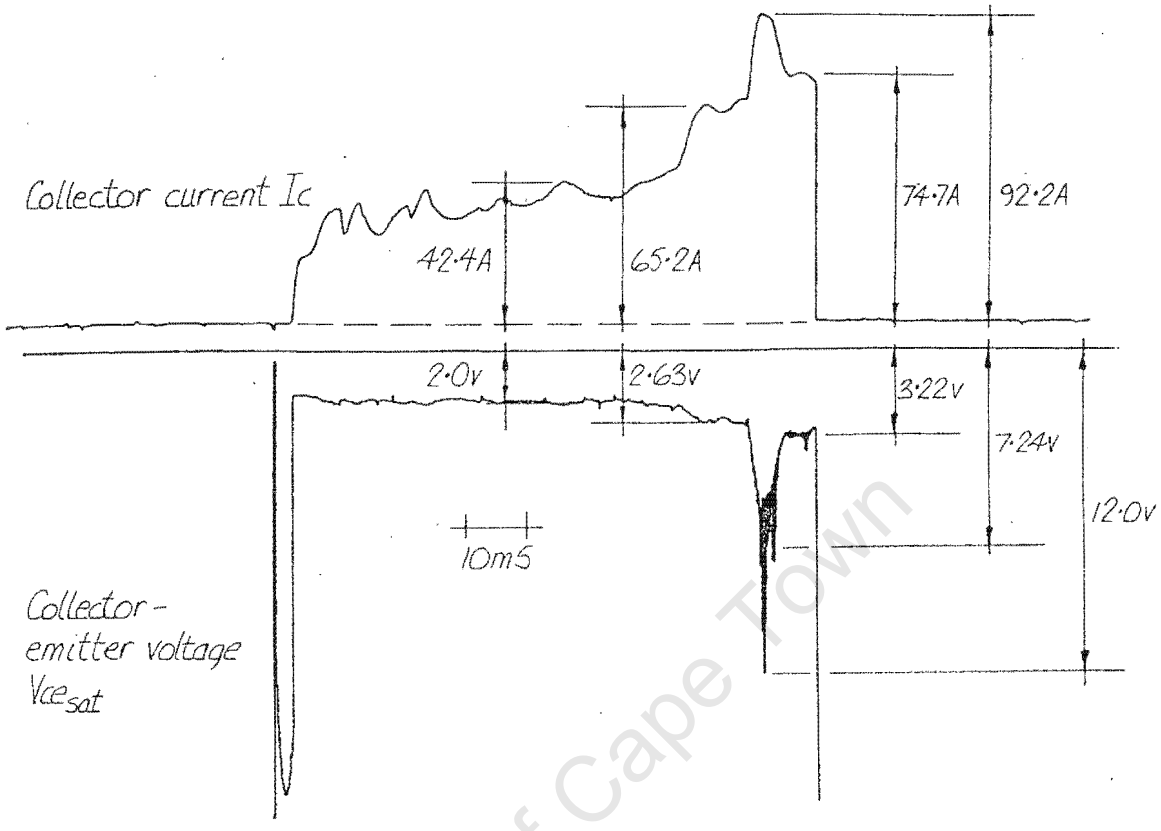

e) 5 amp base drive current

Fig. 4.9 e

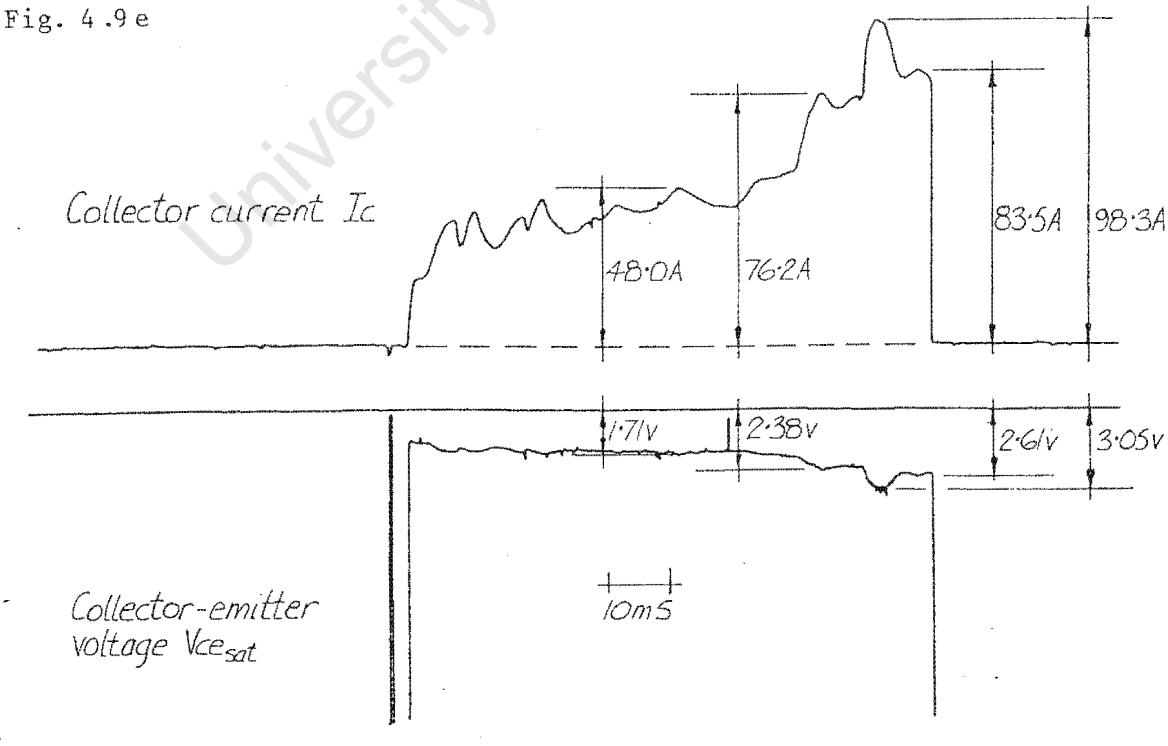

f) 10amp base drive current

Fig. 4.9 f.

will be adequate. In the case of component failure, to avoid further damage, correctly calibrated water fuses (8) were successfully used.

It has been shown (8) that the base charge storage time, when switching off, can be reduced by supplying a negative base drive. The negative drive can be produced by placing an inductance in series with the base-emitter resistor R9 (see figure 4.4). However, for normal to large collector currents, the reduction in delay time was not appreciably large enough to warrant introducing inductance into the circuit.

4.5 Operation of the snubber network.

The snubber network is a cheap but successful way to protect power transistors from failure due to too high currents when switching off. The capacitance C, see figure 4.1a, forms the basis of the network with a diode and resistor added to avoid high energy discharges through the capacitance when the transistor switches on. Figures 4.11a and b show the action of the circuit. As a result of the addition of the snubber network, the load current through the winding remains approximately constant over the switching period 't'. That is, the current through the transistor decreases and the current through the capacitor increases in such a way that their sum remains approximately constant. It has been shown (10) that the following formulae can be used to assist determining the values C and R:-

$$C \geq Ic_{max} t \; / \; Vce_{max} \text{ farads} \qquad R \leq t_1 / 4C \text{ ohms}$$

FIG. 4.10

LOADED AND NO-LOAD SWITCHING DELAYS BETWEEN CONTROL LOGIC INSTRUCTION AND ESM 1000 POWER TRANSISTOR REACTION. (ON LOAD THE TORQUE PRODUCED WAS 17.2 Nm FOR A rms PHASE CURRENT OF 20.4A AND THE ROTOR SLIP WAS 4.2% OR 42 rpm WITH AN INPUT OPERATING FREQUENCY OF 50 Hz.

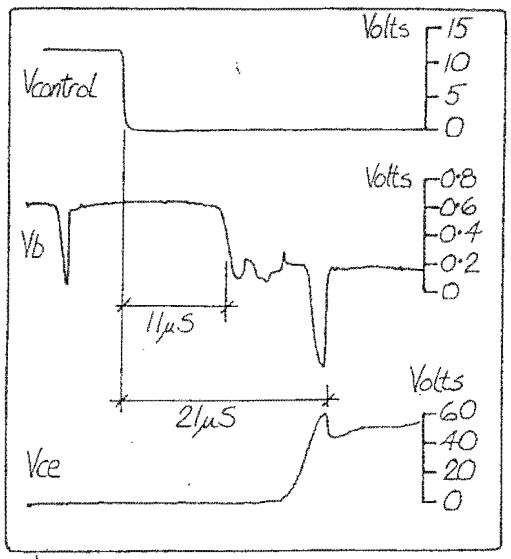

a) Switching off delay at 50Hz no-load

FIG. 4.10a

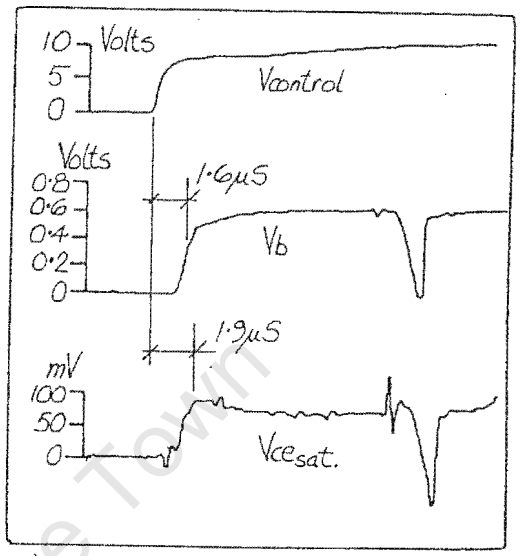

b) Switching on delay at 50Hz no-load

FIG. 4.10b

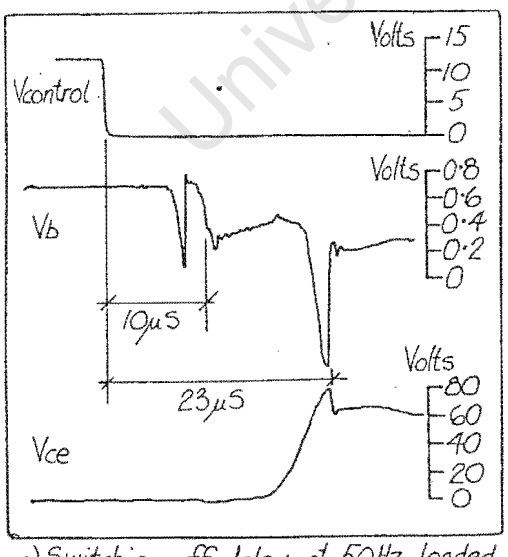

c) Switching off delay at 50Hz loaded

FIG. 4.10c

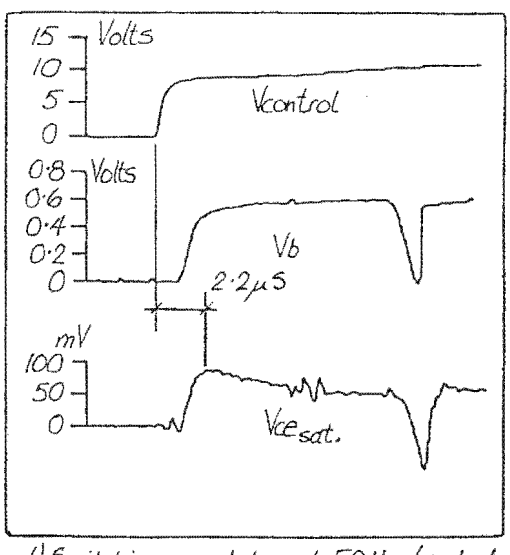

d) Switching on delay at 50Hz loaded

FIG. 4.10d

FIG. 4.11

CURRENT DRAWN BY SNUBBER CIRCUIT WHEN ESM 1000 POWER SWITCHING TRANSISTOR SWITCHED OFF.

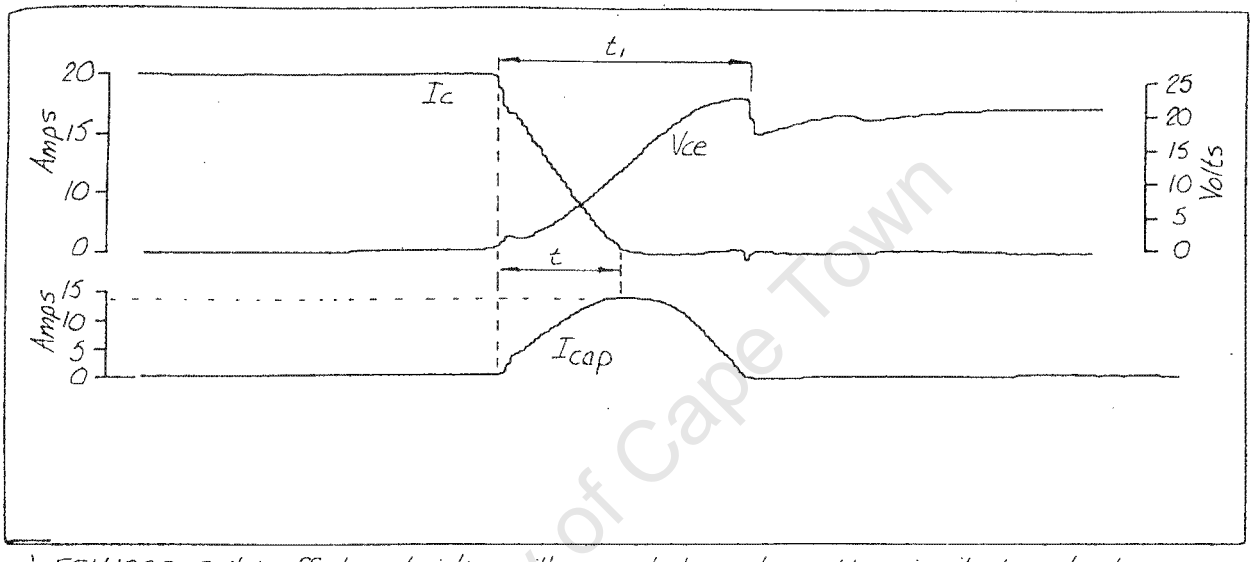

a) ESM1000 Switch-off characteristics with current drawn by snubber circuit at no-load.

FIG. 4.11a

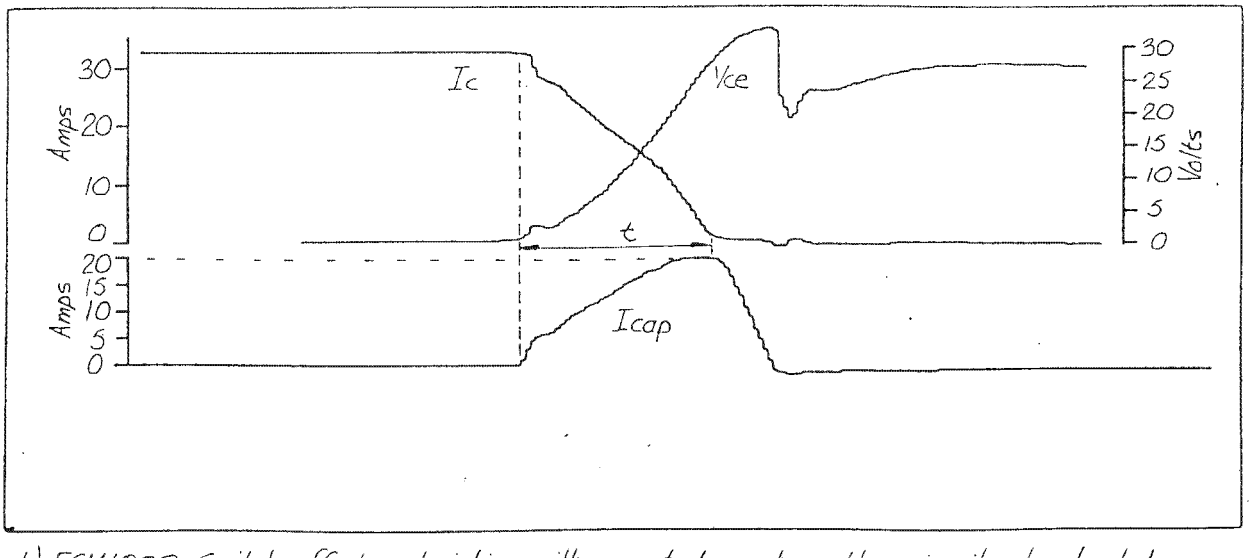

b) ESM1000 Switch-off characteristics with current drawn by snubber circuit when loaded.

FIG. 4.11b

CHAPTER 5.

The Inverter Digital Controller.

5.1 Bridge inverter logic control.

Figure 5.1a shows an example of the four signals required to operate one bridge inverter and supply, in this case, a quasi-square wave to its phase winding. For 3 phase operation these four signals are repeated, but phase shifted from the original set by $2\pi/3$ and $4\pi/3$ radians respectively for each of the other two phases. Similarly, for a 9 phase system each set of four signals will be phase shifted by $2\pi/9$ radians from each other.

One cycle, i.e. 2π radians, has been subdivided into 126 'time units'. The number 126 was chosen because it is divisible by 3 and 9, thus enabling exact phase shifting to be implemented for 3 and 9-phase operation. Figure 5.1b shows the form of storage used, i.e. an array, with the storage element being a MCM 6810AL Random Access Memory. Row one of the memory contains the 'times' at which changes occur in the status of the four control lines of phase 1 bridge inverter. What the four control lines change to is determined by which column the 'time' is placed in. Row two contains the 'times' at which changes occur in the status of the four control lines of phase 2 bridge inverter. As can be seen phase 2 "times" are phase shifted by 126/9 = 14 'time units' from phase 1. The same phase shift is repeated for the other seven phases (or rows). By decoding the column and row address lines separately as well as reading the data in the array, one can obtain, using the minimum of storage space, enough information to produce square or quasi-square waves at the bridge output terminals.

This system of storage allows between 1 and 9 phase operation to be selected by reprogramming the random access memory chip. Also, it lends itself to producing non-symmetrical waveforms and more importantly allows grouping of windings without physical connection of the winding so that pole amplitude modulation (12) can be implemented.

The logic controller has been constructed using DIN standard plug in cards

FIG. 5.1

A) TYPICAL LOGIC SIGNALS WHICH CONTROL THE FOUR TRANSISTORS IN A BRIDGE INVERTOR

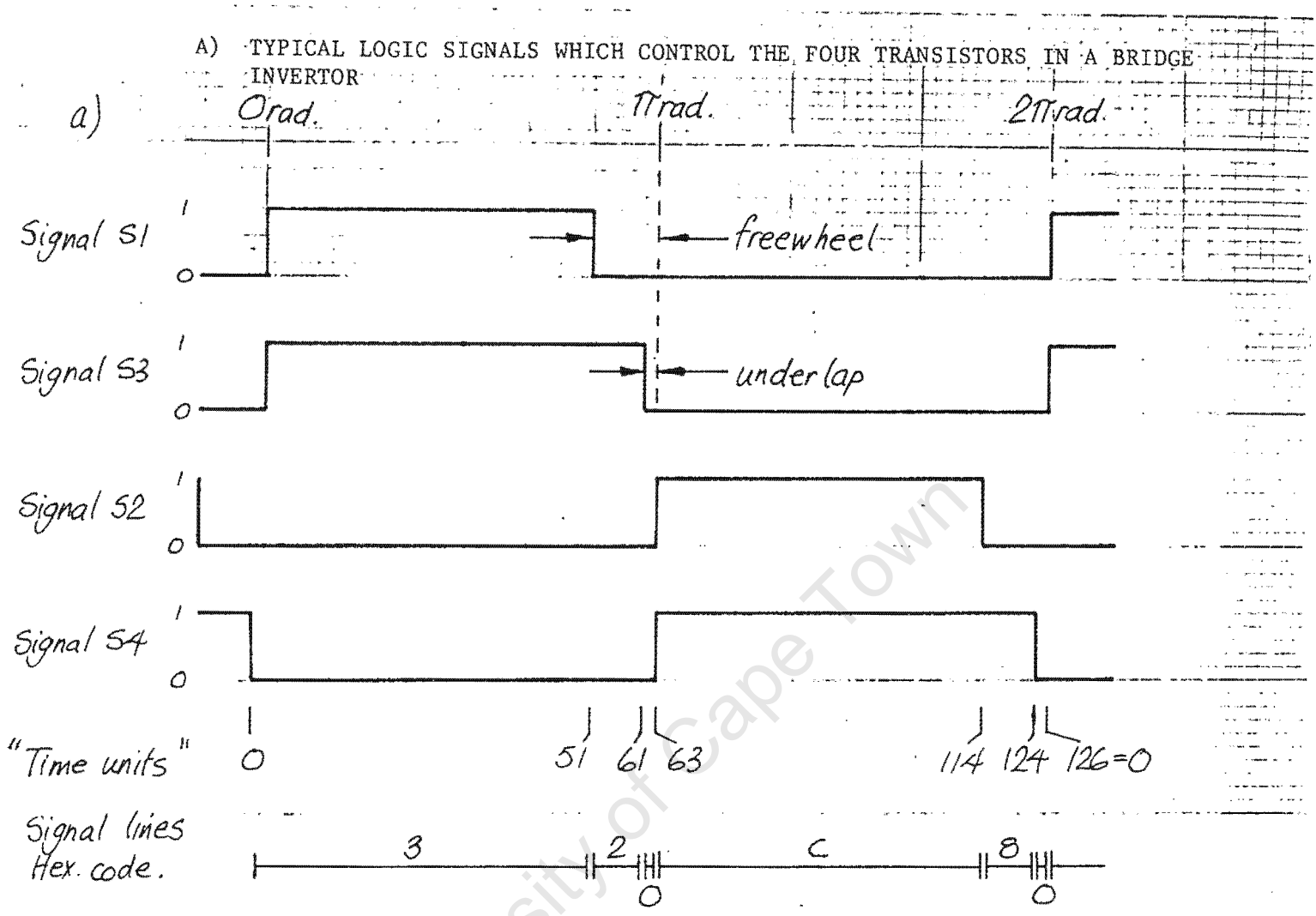

B) FORMAT OF MEMORY STORAGE IN MCM 6810 RANDOM ACCESS MEMORY. NOTE THAT HEXIDECIMAL NUMBERS ARE STORED, NOT DECIMAL

Phase	Signal code	0→3	3→2	3→0, 2→0	0→C	C→8	C→0, 8→0
	1	0	51	61	63	114	124
	2	14	65	75	77	2	12
	3	28	79	89	91	16	26
	4	42	93	103	105	30	40
	5	56	107	117	119	44	54
	6	70	121	5	7	58	68
	7	84	9	19	21	72	82
	8	98	23	33	35	86	96
	9	112	37	47	49	100	110
	Windings undergo:	+ve bias	freewheel	underlap	-ve bias	freewheel	underlap

Memory storage format in Logic Controller

with integrated components wire wrapped onto the cards. A fascia panel contains four programming toggle switches, three operating controls and nine output sockets for separate plug in signal line connections to each bridge inverter.

The programming switches are:-

i) Program/Run
ii) Read/Write
iii) Memory Enable/Disable
iv) Memory Address Step/Reset

The operating controls are:-

i) Applied frequency 10 turn potentiometer
ii) Forward/Reverse selector
iii) Mark-space ratio selector switch

Additional preset controls situated on cards:-

i) Chopping frequency preset potentiometer
ii) Interlacing delay preset potentiometer

In all, six cards are used and they contain:-

i) Memory and master control circuits
ii) Manual program circuitry
iii) Mark-space and interlacing circuit
iv),(v),(vi) Output switching and buffer circuits

The operation of the logic controller is described briefly to enable servicing to be performed. The logic circuit diagrams are given in appendix B.1.

5.2 Memory and control circuit.

The 'output frequency control clock' oscillates at 126 times the applied output frequency which is set via potentiometer R4. The clock signal CC drives a binary 'control counter' which automatically resets to zero after the count of 125. This counter provides the continuously repeating 1 cycle of 'time units' as shown in figure 5.1a.

At the beginning of each clock pulse CC (in fact on the +ve going edge) a 1 MHz signal is allowed to drive an 'address counter'. This counter sequentially addresses the random access memory and after scanning all memory words, 54 in all, resets and inhibits the 1 MHz signal. Therefore, each time the control counter counts up, the random access memory is scanned once within a period of 36μS.

The data lines of the RAM (DA0 to DA6) are fed to a comparator into which the 'control counter' outputs (CC0 to CC6) are also fed. Therefore, if during a memory scan one of the stored 'time units' equals the 'time unit' set on the 'control counter', a signal CC=DA is passed to the phase decoder.

While the memory is being scanned by the 1 MHz 'address counter', further operations are taking place. Three of the address lines are being decoded to give the four control lines switching codes S1 to S4 required by each bridge inverter. At the same time the other four address lines are being decoded to indicate to which phase a change in control line status must occur. However, only when the signal CC=DA is received by the 'phase decoder' will the decoder pass the information on to the output buffers via L1 to L9.

The address lines (AD0 to AD6) and the data lines (DA0 to DA6) of the RAM are fed back to the LED display on the programming keyboard.

5.3 Manual program circuit.

The keyboard used is a hexidecimal type and at every keystroke the binary code for that particular key is set up on the four input lines. After the input lines are set, a control pulse is received from the keyboard that will latch the information into one of the D-type quad buffers. On the next keystroke, via the action of the JK flipflop, the information will be stored into the other quad D-type buffer. The information storage will alternate between the two quad buffers as more keys are pressed.

During programming the read/write toggle switch must be in the write position. After each data entry the spring loaded 'step' toggle switch must be pressed so that the address counter is incremented.

5.4 Mark-space and interlacing circuit.

This circuit is driven by an asynchronous clock (with respect to the main control clock CC) which has a frequency range of 3.6 KHz to 9 KHz set by a preset potentiometer R9. The pulses produced by this clock are constant width negative pulses 10μS long. The clock drives two counters which in turn feed four binary to decimal decoders. The four decoders provide all the necessary signals to produce the variable mark-space ratio chopper modulation.

Although the counters IC5 and IC8 are running synchronously, their counts will be different at any particular time. This is achieved by feeding back a reset pulse DELSYNC from one counter to the other with the reset pulse being derived from the signals C1 to C9 such that 'phase shifting' between the two counters is varied by selecting one of these signals.

Signals A1 to A9 are slightly delayed behind B1 to B9, and D1 to D9 delayed behind C1 to C9. Referring to figure 5.2, this delay allows an underlap period within each bridge inverter to account for the ESM 1000 power transistor switching delays.

The time delay mentioned in section 2.4, which will limit switching surges in the dc supply, and also shown in figure 2.3d, can be achieved by delaying the output of pulses C1 to C9 and D1 to D9 via potentiometer R4. Referring to figure 5.2, the effect of this is seen to be the advancing or retarding of the trailing edge of the chopper modulated waveform. Because the leading edge remains stationary, the inter-phase delay is introduced. This can be seen much more closely in figure 2.3b.

When a mark-space ratio of 0/9 (or no output from bridge inverter) is required, the A and B pulses are inhibited via CLR5. This in turn causes both Q1 and Q2 to switch off and Q3 and Q4 to remain on, effectively giving zero signal across the winding. If the selector switch is adjusted to give a mark-space ratio of 9/9, pulses C and D are now inhibited via CLR8 and therefore no modulation of the basic quasi-square wave is performed.

FIG. 5.2

TIMING SIGNALS FOR PHASE 1 USED TO ACHIEVE A 3/9 MARKSPACE RATIO CHOPPER MODULATION OF A QUASI SQUARE OUTPUT WAVEFORM

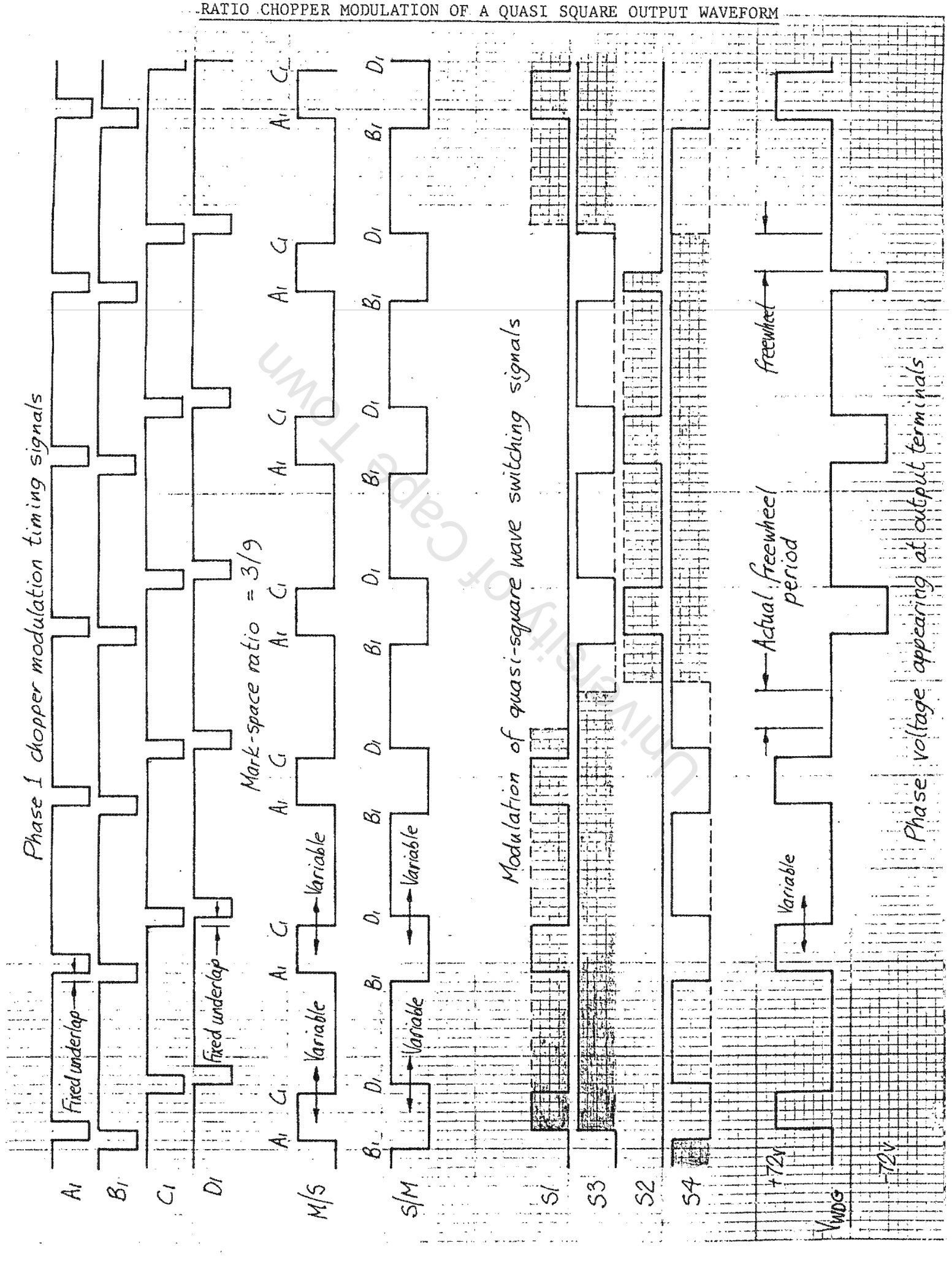

5.5 Output switching and buffer circuit.

As the memory is scanned by the 1 MHz 'address counter', the four code lines S1 to S4 continuously and sequentially change and set up the square or quasi-square switching codes. These are fed via a common bus to nine quad D-type flipflops (three per board). When a 'time unit' stored in the memory corresponds to a 'time unit' on the 'control counter', a pulse will be sent to one of the quad latches. The position of the 'time unit' in the memory, see figure 5.1b, will determine which latch gets loaded and also what data it is loaded with.

The mark-space and space-mark pulses shown in figure 5.2 are developed by the set/reset flipflops on the output boards. Chopper modulating pulses A1 to A9 and C1 to C9 enable the mark-space waveform to be developed with A's setting the flipflops and C's resetting them. The space-mark waveform is developed in a similar manner using B1 to B9 and D1 to D9.

The four outputs to phase 1 bridge have been denoted S1A, S1B, S1C and S1D. The boolean logic to achieve the correct switching of transistors Q1 to Q4, bearing in mind that the output drivers are of the inverting type, is as follows:-

$$S1A = \overline{\overline{S1} + \overline{M/S}} \qquad S1B = \overline{\overline{S2} + \overline{M/S}}$$

$$S1C = S3 + S/M \qquad S1D = S4 + S/M$$

The over current/voltage (90V) protection circuit output is fed to this board so that if the phase current or voltage rises too high, all outputs are immediately clamped to zero volts. As mentioned earlier, this will not protect the ESM 1000 power transistors against short circuits, due to signal delays being inherent in the system,but it will protect against normal motor overloading etc.

CHAPTER 6.

System Optimization and Behaviour.

6.1 Optimum fluxing of machine excited with chopper modulated quasi-square waves.

When referring to optimum fluxing, the author means that the machine is excited such that the magnetic circuit is slightly saturated.

The induction motor was designed so that it would be optimally fluxed if, at a frequency of 50 Hz, a sinusoidal voltage of 60 volts rms was applied to each 9-phase winding. No-load curves were obtained for the motor operating in the 3-phase sinusoidal mode ie. three sets of windings joined in series as per circuit shown in appendix B.4. Figure 6.1 shows these curves for the motor excited at frequencies of 5,10,20,40 and 50 Hz. Using the assumption that applied voltage is proportional to frequency will give the results shown in table 6.1 which were derived from figure 6.1

Table 6.1 Applied phase to neutral rms voltage and phase current at a particular frequency for a 3-phase system.

Frequency Hz	Applied volts = 3 x f x 60/50 volts	Measured phase current amps
5	18	24.0
10	36	26.5
20	72	28.0
40	144	27.5
50	180	27.5

These results reinforce, as a result of the approximately constant magnetizing currents, the statement that applied voltage be assumed proportional to frequency.

FIG. 6.1 (Ref D.4)

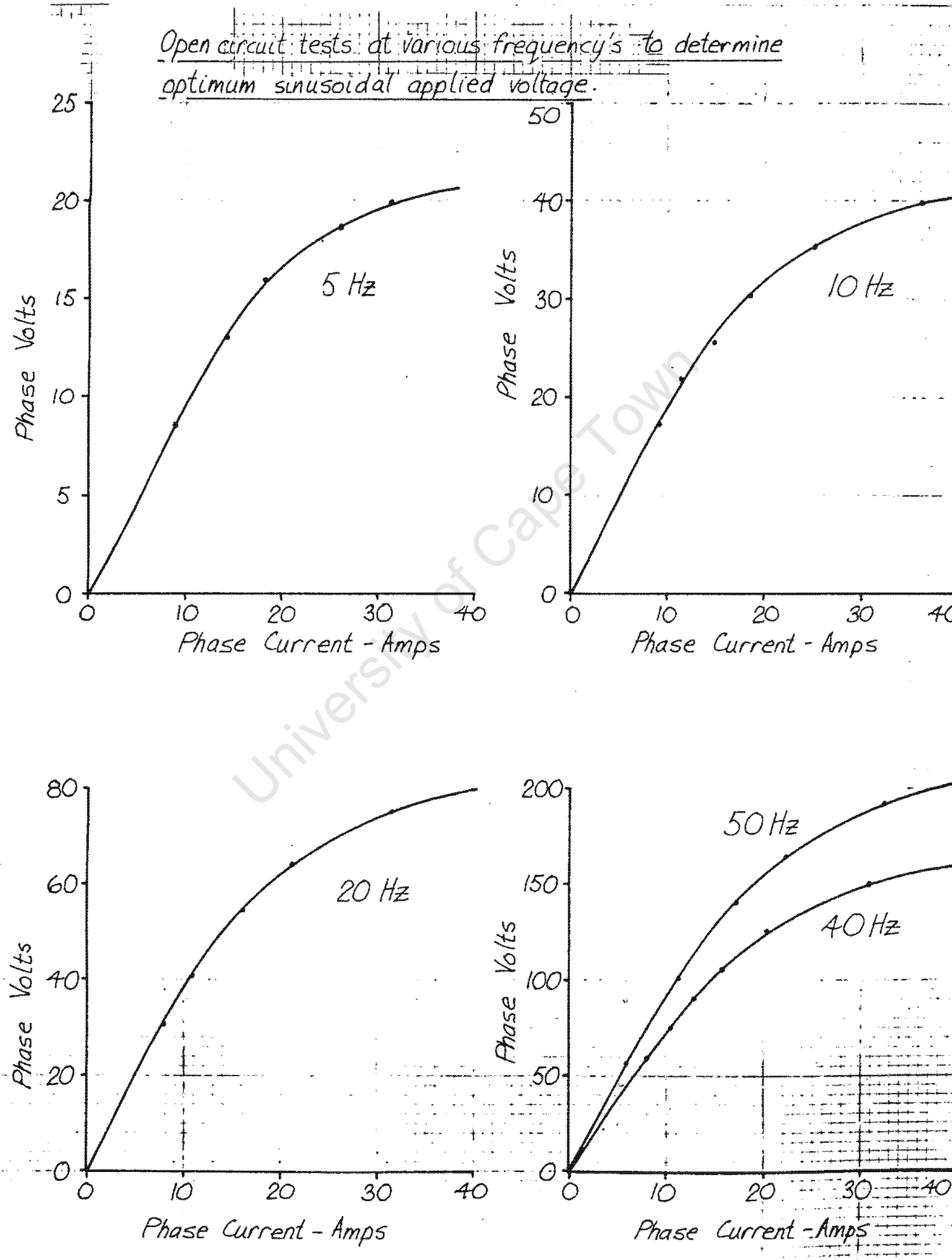

FIG 6.2 (Ref D.5)

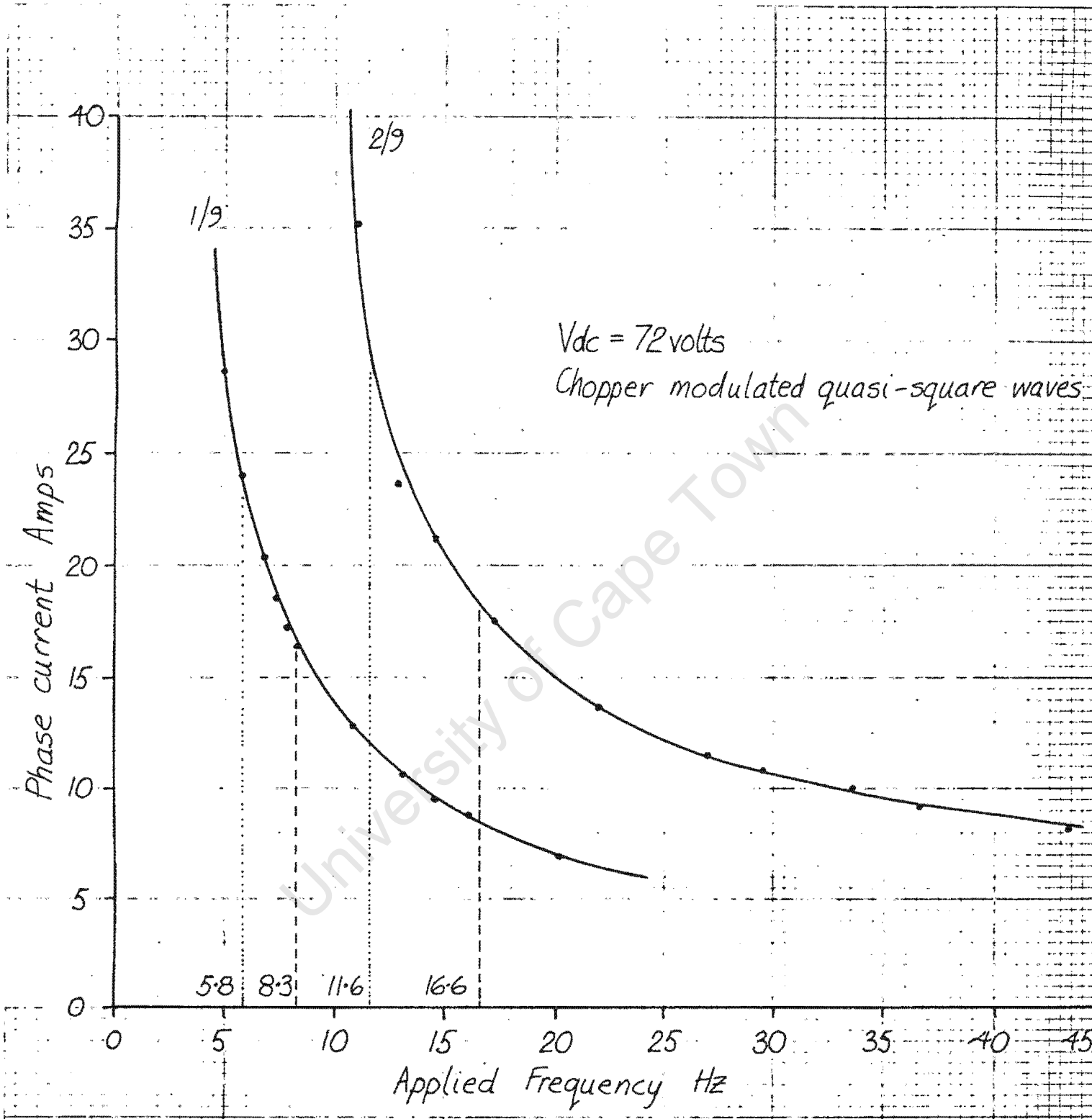

Open circuit tests at mark-space ratio's of 1/9 and 2/9 to determine saturation effects.

When chopper modulated quasi-square waves are used, the picture becomes more complex. Theoretically it was shown in chapter 1 that the majority of the output power was derived from the fundamental component of the phase current. In other words, the fundamental component of the applied voltage can, very approximately, be considered the main factor affecting magnetizing flux within the machine. The Fourier analysis of the quasi-square wave gives the rms value of the fundamental voltage as:

$$V_1 \text{ rms} = \frac{1}{\sqrt{2}} \cdot \frac{4 V_{dc}}{\pi} \sin((\pi - \beta)/2) \qquad (6.1)$$

When the quasi-square wave is modulated with a variable mark/space ratio waveform, where the ratio varies between 1/9 and 9/9, the applied dc voltage becomes an effective mean value giving a fundamental value of:

$$V \text{ rms} = \frac{u}{9} \cdot \frac{1}{\sqrt{2}} \cdot \frac{4 V_{dc}}{\pi} \sin((\pi - \beta)/2) \qquad (6.2)$$

$$u = 1,2,3....9$$

And with the proportionality condition between applied voltage and frequency it can be said that:

$$\text{Operating frequency, } f = \frac{50}{60} \cdot \frac{u}{9} \cdot \frac{1}{\sqrt{2}} \cdot \frac{4 V_{dc}}{\pi} \sin((\pi - \beta)/2) \qquad (6.3)$$

Tests performed to determine the saturation effects at set mark/space ratios, ie.frequency was reduced while a particular mark/space ratio remained constant and phase current was monitored, indicated that the calculated operating frequency was causing oversaturation of the machine. Figure 6.2 gives the results obtained for two mark/space ratios of 1/9 and 2/9. The lower frequency marked on each curve are those calculated from equation 6.3. It should be noted that were the induction motor to operate with a mark space ratio of 2/9 at a frequency of 11.6 Hz, a drop in frequency of only 1 Hz would cause the phase current to rise from 29 amps to over 40 amps, an increase of more than 25%.

Equation 6.3 was modified to give more realistic frequencies which would also take into account the effect on saturation of the other harmonics in the quasi-square waveform. Therfore:

$$\text{Modified operating frequency, } f = \frac{60}{50} \cdot \frac{u}{9} \cdot \frac{1}{\sqrt{2}} \cdot \frac{4V_{dc}}{\pi} \cdot \sin((\pi - \beta)/2) \quad (6.4)$$

Giving:

Table 6.2 Operating frequency for a 9-phase chopper modulated quasi-square waveform.

Mark/space ratio	Operating frequency, Hz
1/9	8.3
2/9	16.6
3/9	25.0
4/9	33.3
5/9	41.6
6/9	49.9
7/9	58.2
8/9	66.6
9/9	74.9

The calculated frequencies given in the last table indicate the lower limit that can be safely used without oversaturating the machine. The frequencies for each mark/space ratio setting can be raised, but it should be remembered that this will cause a decrease in peak torque. Therefore, at a mark/space setting of 1/9, a frequency range 8.3 Hz and higher may be used and at a setting of 2/9 the range is 16.6 Hz and higher.

6.2 Optimizing freewheel angle for maximum efficiency.

Load tests were performed on the test motor and locked rotor tests on two other motors to determine at which freewheel angle the motor operates most efficiently.

The efficiency curves for the test motor connected for 9 phase operation are shown in figure 6.3. Definite increases in efficiency of up to 6% can be seen to occur when the freewheel angle is increased from 0 deg. to approximately 30 deg. With the applied voltage kept constant at 20 volts (20v causes the test motor to be fully fluxed at 20Hz) and for a particular torque, it was noticed that as maximum efficiency was reached, a minimum slip was achieved. Results show that for a particular torque the decrease in slip is approximately 30% for a 0 deg. to 30 deg. freewheel change.

The locked rotor tests for the other motors (both with deep bar rotors) are shown in figure 6.4. These results plot the ratio of useful torque-producing power absorbed by the rotor versus input power to the stator windings, which can be written as;

$$\gamma = \frac{P_{rotor}}{P_{in}} \times 100\% = \frac{T\omega_1}{P/2} \cdot \frac{100\%}{P_{in}} \qquad (6.5)$$

These tests were done with the motors over-fluxed, i.e. applied voltage higher than prescribed for full flux, which probably accounts for the well defined curves. From figures 6.4a,b and c as torque is increased, so does the required freewheel angle for maximum efficiency. This is not apparent in figure 6.3. For a torque increase of 10 to 50 Nm, the freewheel angle needs to be changed from 25 to 30 degrees.

Further analysis is required to determine the exact reason for this variation. A set freewheel angle of 31.4 degrees (11 controller 'time units' - see section 5.2) has been chosen for the 9 phase tests, thus giving close to optimum efficiency over most of the working range of the motor.

Figure 6.4d shows that the freewheel angle for maximum 3 phase efficiency is approximately 55 degrees.

Figure 6.3 Efficiency curves derived from 9-phase load tests performed on the test motor to obtain optimum freewheel angle when the motor is excited by a fixed 20 Hz quasi-square wave.(ref D.3)

Figure 6.4 9-phase standstill tests performed on;

a) Motor 2 at 5 Hz, 50 Nm (ref D.10) and motor 3 at 5 Hz, 10 Nm.
b) Motor 2 at 10 Hz, 40 Nm.(ref D.10)
c) Motor 2 at 20 Hz, 30 Nm.(ref D.10)
d) Motor 3 at 20 Hz, 20 Nm (3-phase operation).

Efficiency curves derived from 9 phase load tests performed on motor 1 to obtain optimum free wheel angle when the motor is excited by a fixed 20 Hz quasi square wave (ref D.3)

Figure 6.3

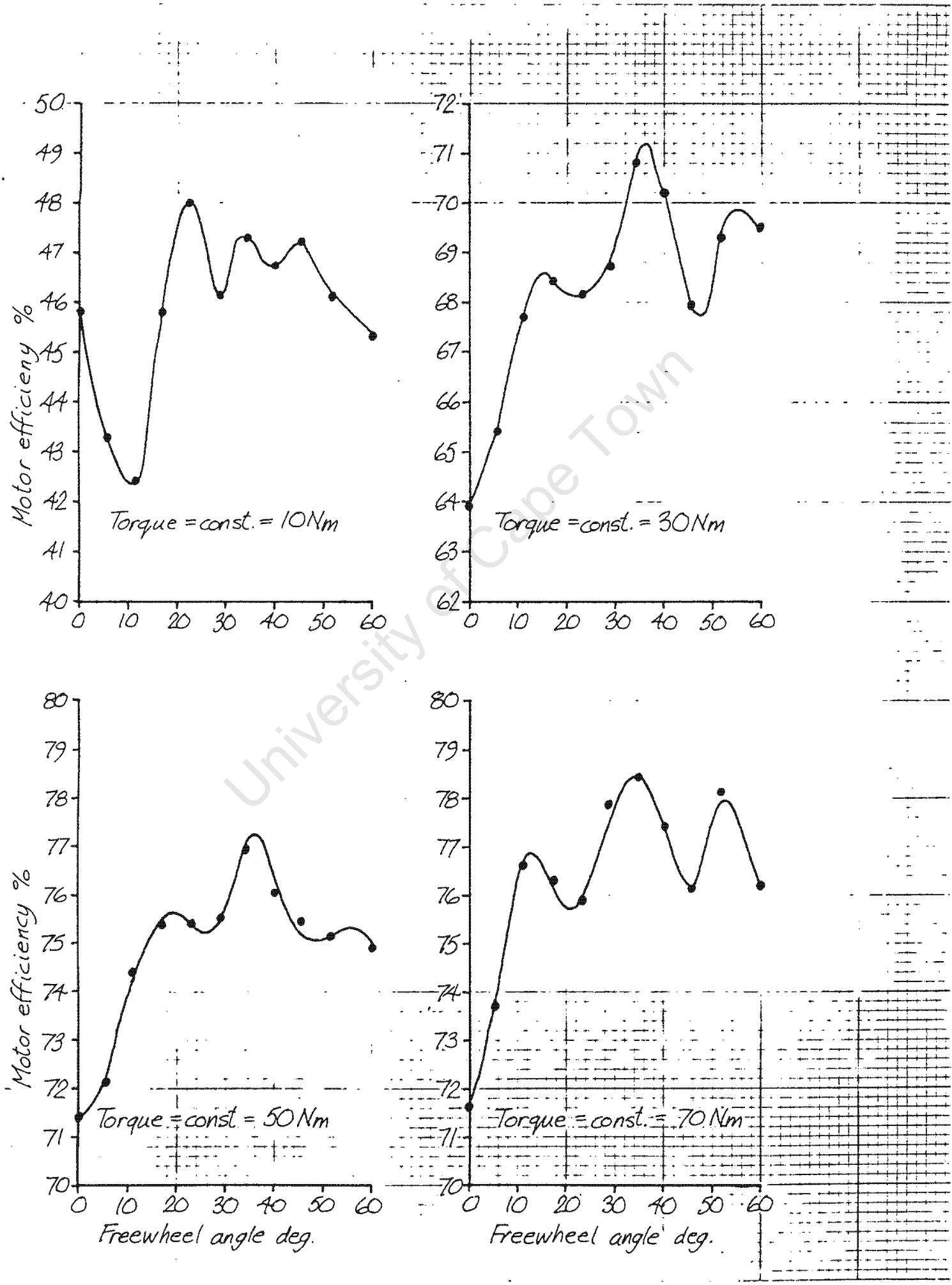

FIGURE 6.4

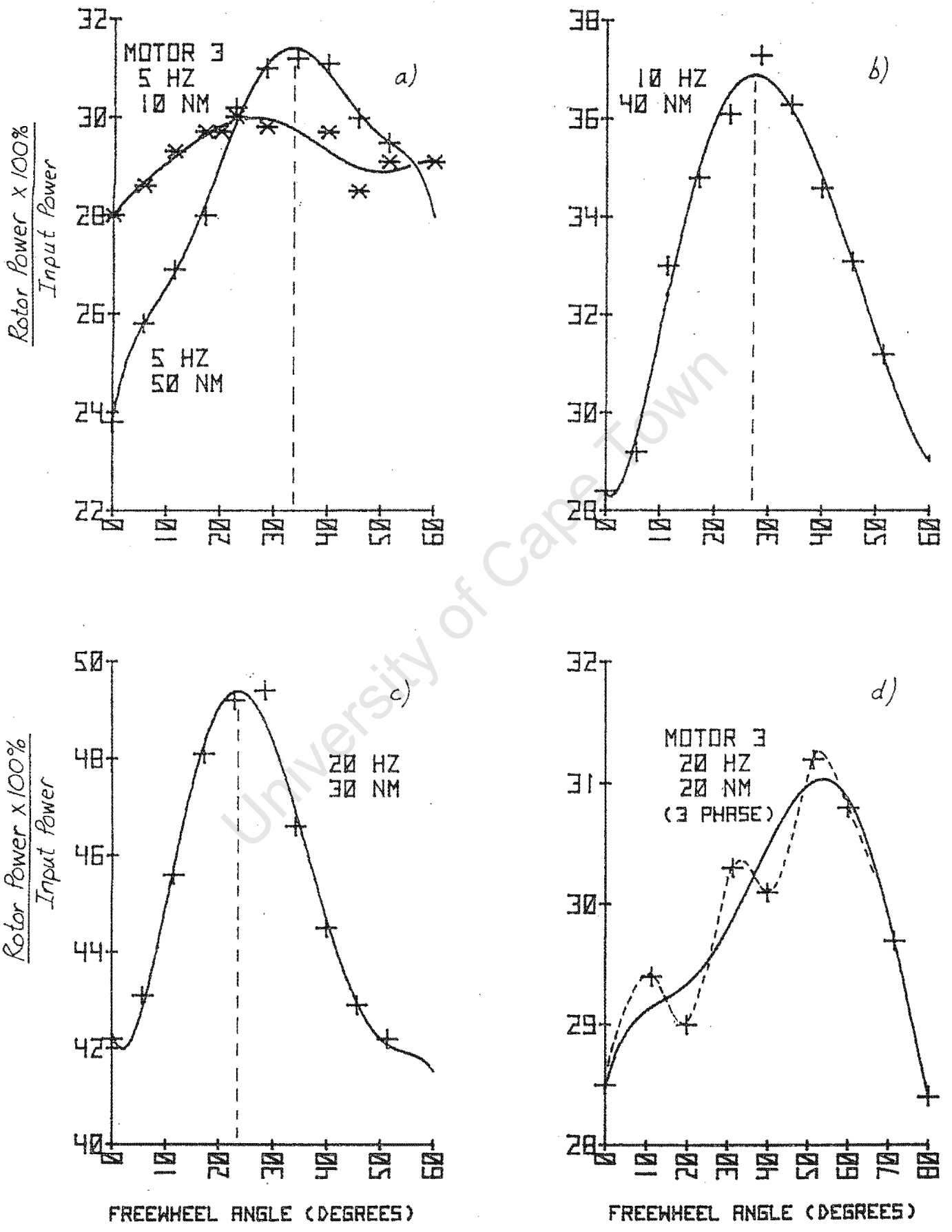

6.3 Determining the most effective chopper modulation frequency.

Load tests were performed under the following conditions:-

Waveform = quasi-square. 31.43 deg. freewheel
Applied frequency = 8.3 Hz, 10 Hz
Phase voltage = 21vrms, 10vrms
Mark-space ratio = 1/9 , 5/9
Chopping frequency = variable

With the motor operating at 10 Hz and a mark-space ratio of 5/9, load curves were obtained for various chopping frequencies. These results are shown in figure 6.5a. From figure 6.5b, where peak efficiency is plotted against chopping frequency, the most efficient performance will be achieved with a chopping frequency of approximately 1.2 KHz. Malengret (7) chose f(chopping) = 800 Hz at an applied frequency of 12.5 Hz. His chopping frequency, however, varied proportionally to the applied frequency.

Further tests showed that if the applied frequency was reduced below 10 Hz and the chopping freqency was also decreased the torque output would increase. In particular at an applied frequency of 8.3 Hz (and mark-space ratio = 1/9) the chopping frequency was reduced from 1.2 KHz to 240 Hz. This caused a peak torque increase of 5 Nm, but, as a result of saturation effects, the phase current increased by some 40%. At the same time (see figure 6.6) there was a reduction in efficiency of 9%. The saturation, it should be pointed out, is due to the increased time that the dc supply is connected across the winding at the lower chopping frequency.

Results given in chapter 8 show that at a chopping frequency of 1.2 KHz and operating frequency of 70 Hz efficiencies of 80% are obtainable.

6.4 Mechanical resonance problems with system.

While operating the test motor it was found that under certain conditions resonant electro-mechanical oscillations of the motor and brake developed. These oscillations although aggravated by the low stiffness of the torque transducer could, depending on the operating conditions of the motor, very

Figure 6.5 a Efficiency curves for various chopper modulation frequencies whilst operating at 10 Hz, 31.43 deg. freewheel angle and a mark-space ratio of 5/9.

Figure 6.5 b Peak efficiency versus chopper modulation frequency.

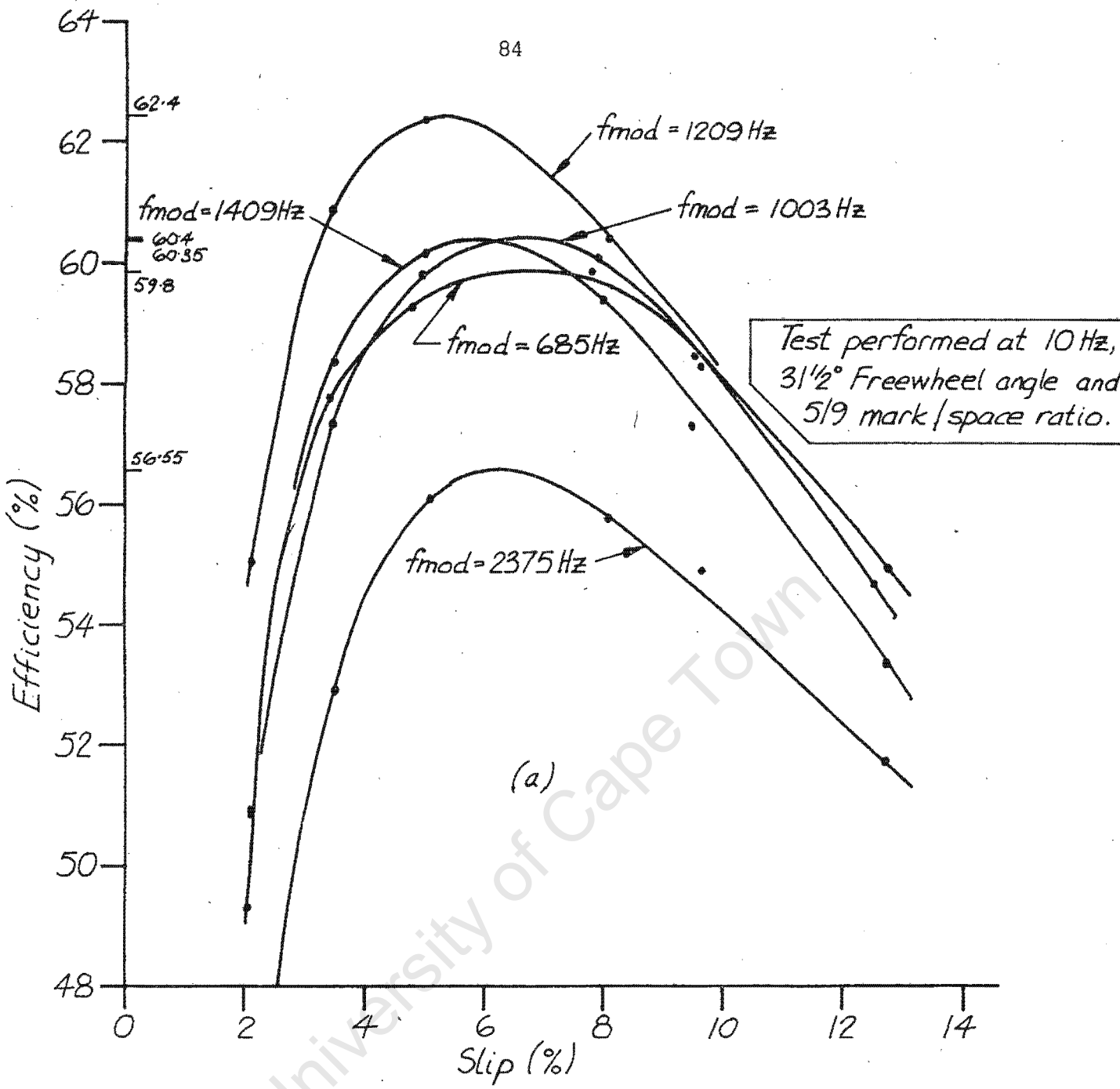

Figure 6.5a

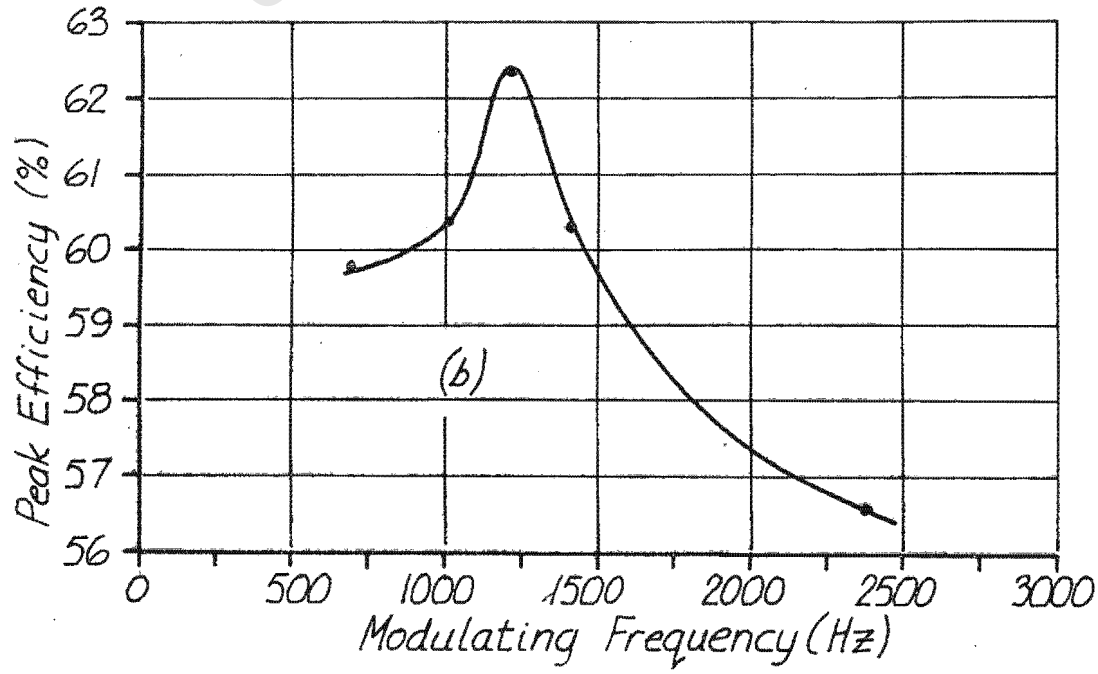

Figure 6.5b

FIG. 6.6 TORQUE AND EFFICIENCY OBTAIN FROM THE MOTOR WHEN OPERATED AT 8.3 Hz WITH CHOPPING FREQUENCIES OF 240 Hz (REF D.2) AND 1.2 KHz (REF D.8.2)

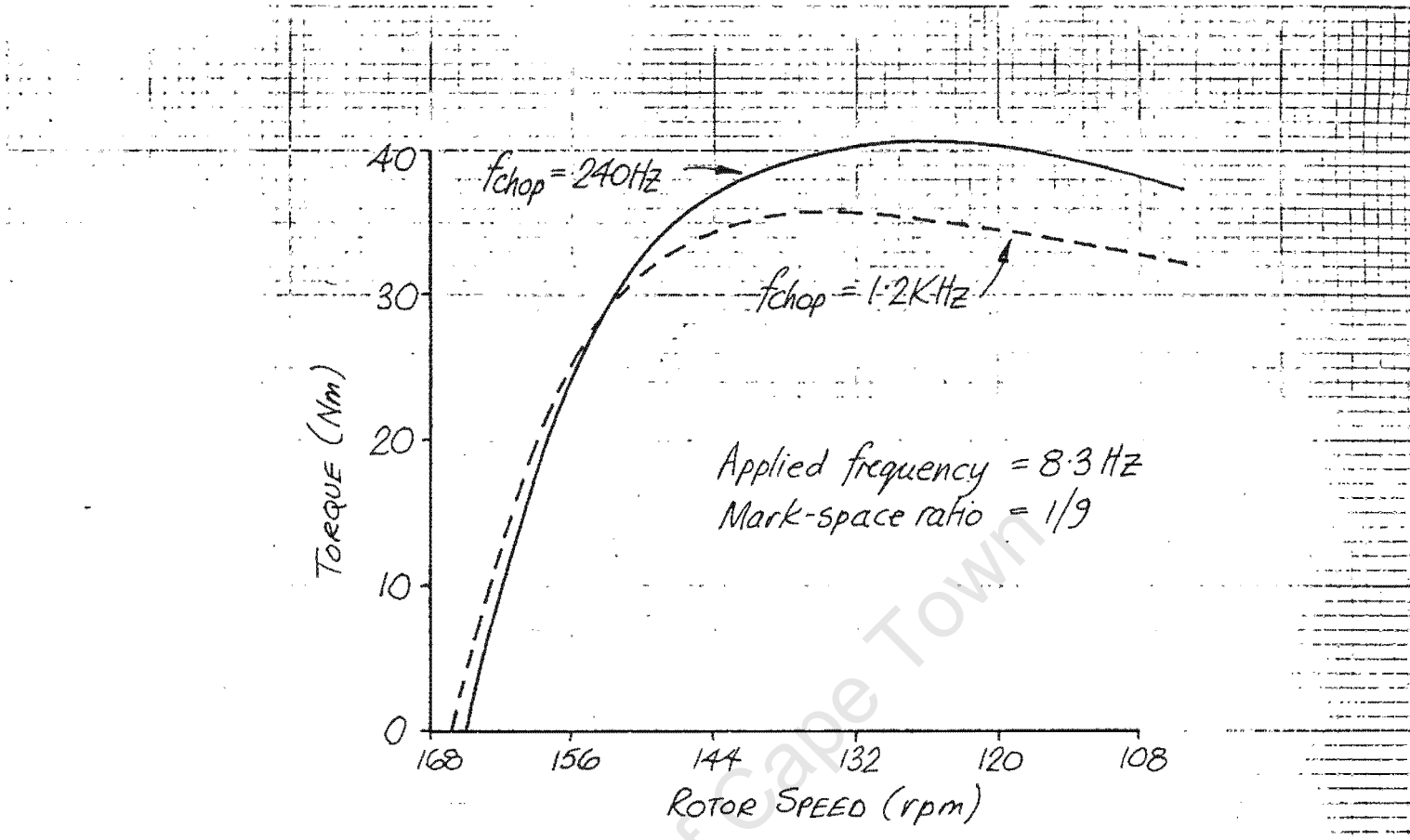

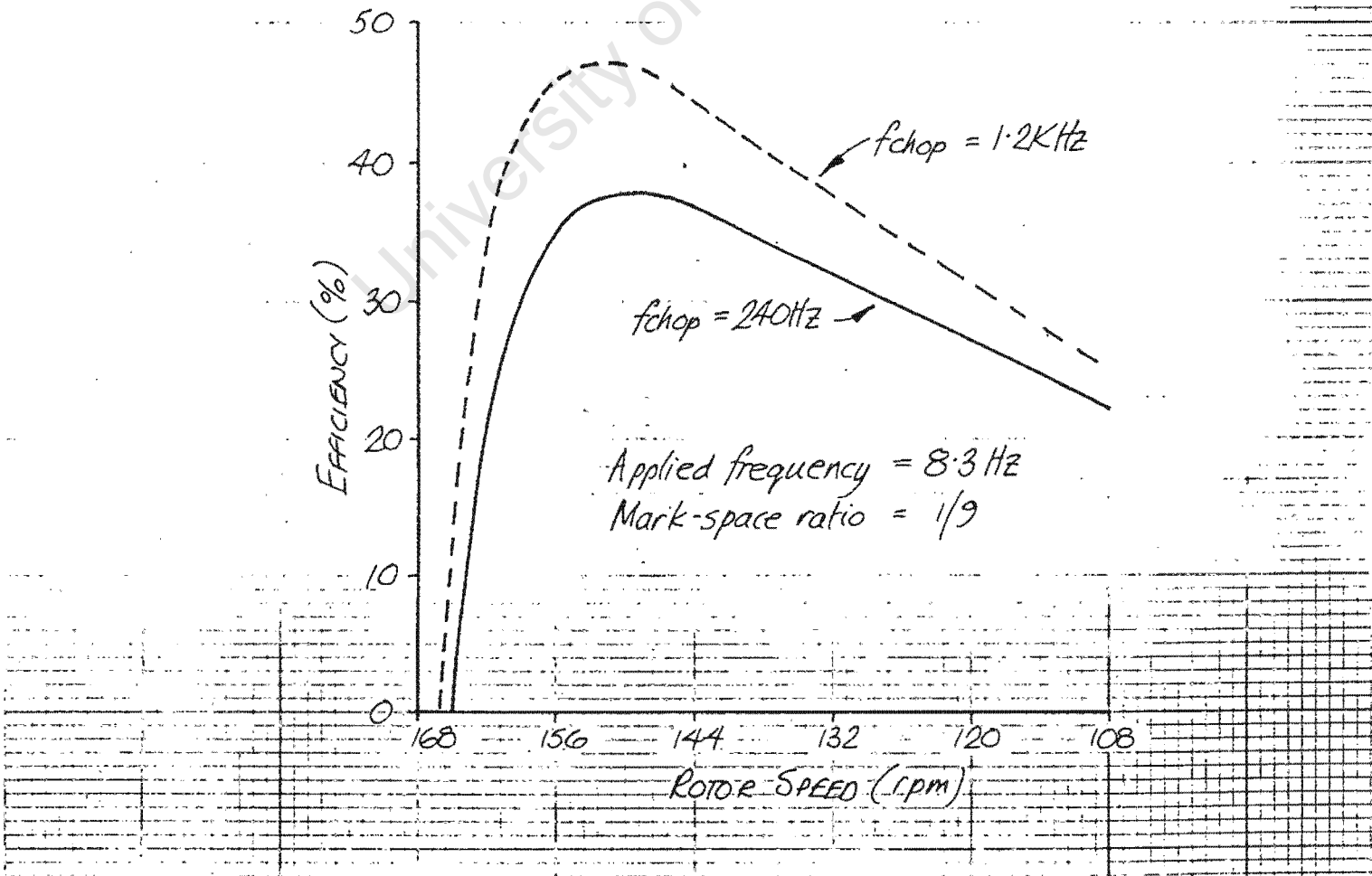

quickly build up and cause the electrical system to become unstable. This problem occurred with both square/quasi-square wave and sinusoidal excitation. The oscillations predominate at very low frequencies when the motor is in effect being pulsed and also during medium torque range operations at certain frequencies.

It has been shown (9,18) that instabilities are inherent in an induction motor fed from a variable frequency inverter. Bowler (9) proves that instabilities occur at high and low slips, leaving a stable operating region inbetween whose upper and lower limits are dependant on stator resistance. Fallside (18) approaches the problem differently, showing instability is related to dc supply voltage and frequency and stabilization could be obtained by varying rotor inductance, stator resistance or introducing feedback control. The region of instability in the test system (see figure 6.7) was the inverse of that predicted by Bowler (see figure 6.8) but could be reduced by reducing dc supply voltage. It should, however , be stressed that this instability only occurred at specific operating frequencies and slips which were compatable with the resonant frequency of the system.

The mechanical equivalent circuit of the test system is given in figure 6.7 and using this its resonant frequency can be calculated.

Figure 6.7

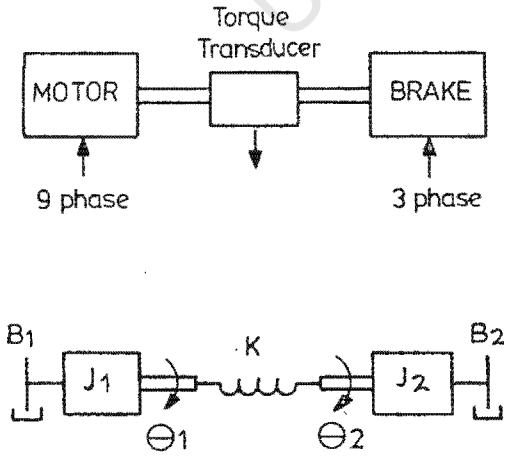

Figure 6.8

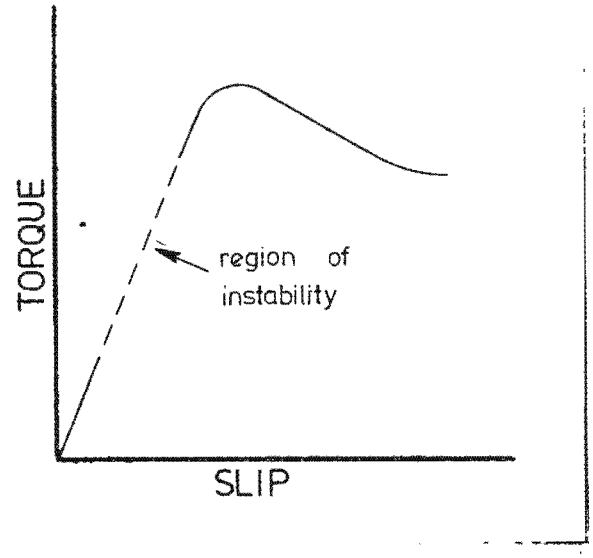

The constants of the system shown in figure 6.7 were found to be:

$B_1 = 0.126$ Nm/rad/sec $\qquad B_2 = 0.723$ Nm/rad/sec

$J_1 = 0.253$ kg.m $\qquad J_2 = 0.764$ kg.m

$K = 11459$ Nm/rad

The 4th order differential equation which defines the operating characteristics of the system is:

$$\frac{\Theta_2}{\Theta_1} = \frac{K/J_1J_2\left(J_1s^2 + B_1s + K\right)}{s^4 + \left(\frac{B_2}{J_2} + \frac{B_1}{J_1}\right)s^3 + \left(\frac{K}{J_2} + \frac{B_1B_2}{J_1J_2} + \frac{K}{J_1}\right)s^2 + \left(\frac{B_1K + B_2K}{J_1J_2}\right)s}$$

By substitution and manipulation, the poles and the zeros of the system can be found, thus showing a theoretical instability point at 39.1 Hz. Practical results, see figure 6.9, show it to be 37.5 Hz at no-load.

With these figures in hand the torque pulsations due to the quasi-square nature of the motor excitation can be separated from those pulsations due to the inherent instability of the system.

Figure 6.9 Actual torque pulsations when the motor is excited with a 1 Hz square wave.

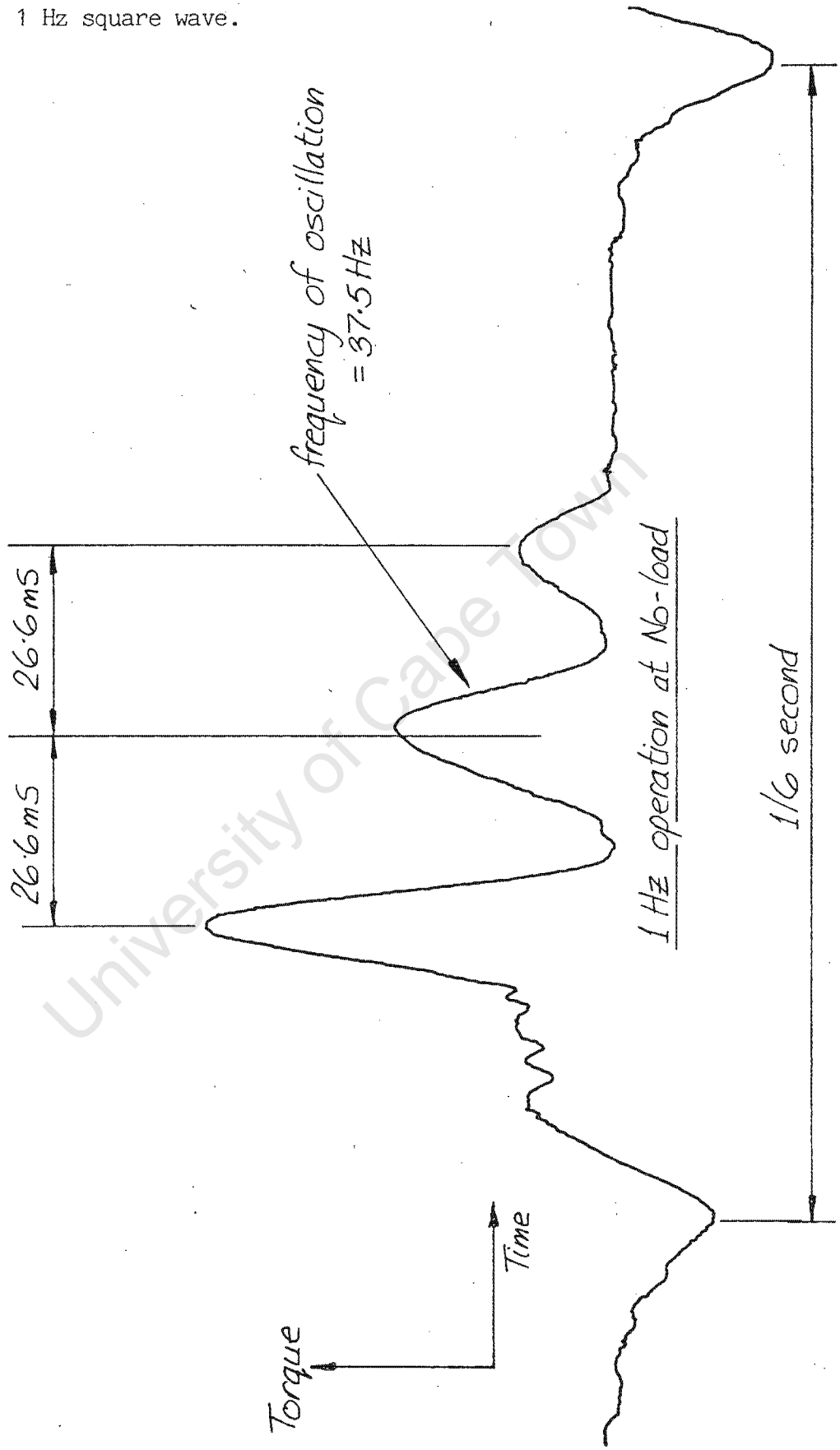

CHAPTER 7.

Results when Test Motor is Excited with Sinusoidal and Unmodulated Quasi-square Voltage Waves.

7.1 Introduction.

Extensive graphical results are given in appendix C.1 and C.2 to illustrate the comparative performance between the test motor excited with 3-phase sine waves and 9-phase quasi-square waves.The freewheel angle of the quasi-square waves was 31.4 degrees as determined in section 6.2 and the quasi-square wave was not chopper modulated. The results shown in appendix C.1 were obtained under the following conditions:

Applied 3-phase sine rms voltage = optimum voltage = 3 x f x 60/50 (7.1)

Applied 9-phase rms fundamental voltage = 1/3 x applied 3-phase voltage at particular frequency. (7.2)

The fundamental rms voltage of the 9-phase quasi-square waveform was determined by measurement using an harmonic analyzer (17).

By making the 3-phase sine wave amplitude equal to the 9-phase fundamental amplitude, any difference in performance will be due to the introduction of additional harmonics from the quasi-square waveform.

Appendix C.2 repeats the tests shown in C.1, but at a lower applied voltage so that judgement can be made of saturation effects on the motor. Therefore, in C.2 the applied 3-phase rms voltage was made equal to 2/3 x optimum voltage with a like reduction in 9-phase voltage.

7.2 Comparisons of efficiency and torque for the motor excited with 3-phase sine and 9-phase quasi-square waves.

7.2.1 Efficiency.

Peak efficiencies at various operating frequencies (refer C.1 and C.2) for optimum and reduced (2/3 x optimum) excitation are given in table 7.1. These results show that:-

(i) 9-phase unmodulated quasi-square wave excitation causes the motor to perform at a lower efficiency than when it is excited with 3-phase sine waves for the relationship Vsine(rms) = V ph[h=1](rms).

(ii) The peak efficiencies of the 9-phase motor become closer to the peak efficiencies of the 3-phase motor as the operating frequency is increased.

(iii) At the excitation voltages chosen, the reduced excitation gives higher peak efficiencies than optimum excitation. This is discussed more fully in section 7.3.

Table 7.1 Peak motor efficiencies derived from results presented in appendices C.1 and C.2 for excitation by 9-phase quasi-square and 3-phase sinusoidal waves.

	Optimum excitation			Reduced excitation		
Freq.	3-phase	9-phase	Diff.	3-phase	9-phase	Diff.
5Hz	55%	47%	8%	56%	--	--
10Hz	66%	61%	5%	69%	62%	7%
20Hz	74%*	71%	3%	77%	71%	6%
40Hz	82%*	77%	5%	83%*	78%	5%

* these results were obtained by extrapolation.

With reference to point (i), the efficiency of the 9-phase motor will always remain lower than that of the 3-phase motor. The major factor influencing

the efficiency is the magnetizing energy which in the 3-phase sine case is supplied continuously to the motor, but in the 9-phase quasi-square case is supplied in small bursts and to only one coil at a time, thus causing higher losses.

A study of magnetizing current drawn can be found in section 7.5.

7.2.2 Torque.

The torque-slip curves of the 3-phase sine and 9-phase quasi-square motor are very similar. When the 9-phase motor is optimally excited, ie. the voltage excitation is such that the magnetic circuit is slightly saturated, the torque produced for a particular slip, at frequencies less than 10 Hz, is approximately 10% higher than for the 3-phase motor. As the operating frequency is increased the two torque-slip characteristics become nearly equal (see appendix C.1).

At reduced excitation (appendix C.2) the torque-slip curves remain more or less equal throughout the whole operating frequency range.

Table 7.2 records the torques obtained for the 3-phase and 9-phase motor with a constant slip of 8 rpm.

Table 7.2 Output torque at a constant slip speed of 8 rpm for excitation by 9-phase quasi-square and 3-phase sinusoidal waves.

	Optimum excitation		Reduced excitation	
Freq.	3-phase	9-phase	3-phase	9-phase
5Hz	49Nm	54Nm	22Nm	---
10Hz	55Nm	61Nm	28Nm	29Nm
20Hz	60Nm	60Nm	27Nm	25Nm
40Hz	62Nm*	62Nm	28Nm	30Nm

* this result was obtained by extrapolation.

The smoothness of the output torque is important, especially at low frequencies, and a selection of torque waveforms measured on a digital storage oscilloscope are presented in appendix C.6. to judge this criterion.

It was shown in section 6.4, that under certain conditions, resonant torque pulsations of approximately 40 Hz could be developed. The resonance does not just exist at this frequency but, according to the conditions prevailing, eg. operating frequency, load and type of excitation waveform, can exist to a lesser extent on either side of 40 Hz. The author has indicated on the relevant plots the frequency of the oscillations.

The following conditions can be observed (appendix C.6):-

(i) At very low quasi-square frequencies, ie. less than 1 Hz, the induction motor performs like a stepping motor (C.6.1). Large step torques are apparent, followed by, in the case of 0.34 Hz and 0.44 Hz, 42 Hz resonant oscillations. At 0.74 Hz the oscillations had increased to 47.7 Hz but their amplitude was lower.

(ii) Both 3-phase sinusoidal and 9-phase quasi-square results taken at 5 Hz (C.6.2,C.6.3) show resonance problems. At higher torques, as in the 10 Hz case (C.6.4a,C.6.5a), these are damped out.

(iii) As freewheel angle is increased from 0 to 31.4 degrees the torque pulsations become less and in fact are negligable at 31.4 degrees (C.6.4).

(iv) Further examples are shown in appendix C.6.6 and C.6.8 for operating frequencies of 20, 40 and 60 Hz. Discounting resonant oscillations, these plots show that torque pulsations are very low when exciting the motor with quasi-square waves having a 31.4 degrees freewheel period.

(v) Quasi-square wave regenerative torques (C.6.9) pulsations are low, however, at high regen. torques large system instabilities developed.

(vi) Resonant regenerative torques when exciting the motor sinusoidally prevented any measurements being taken.

(vii) Although only a few torque plots are given for 3-phase quasi-square wave excitation, it was generally found that under these conditions, system instability developed very quickly and torque pulsations were serious at operating frequencies less than 30 Hz.

FIG 7·1

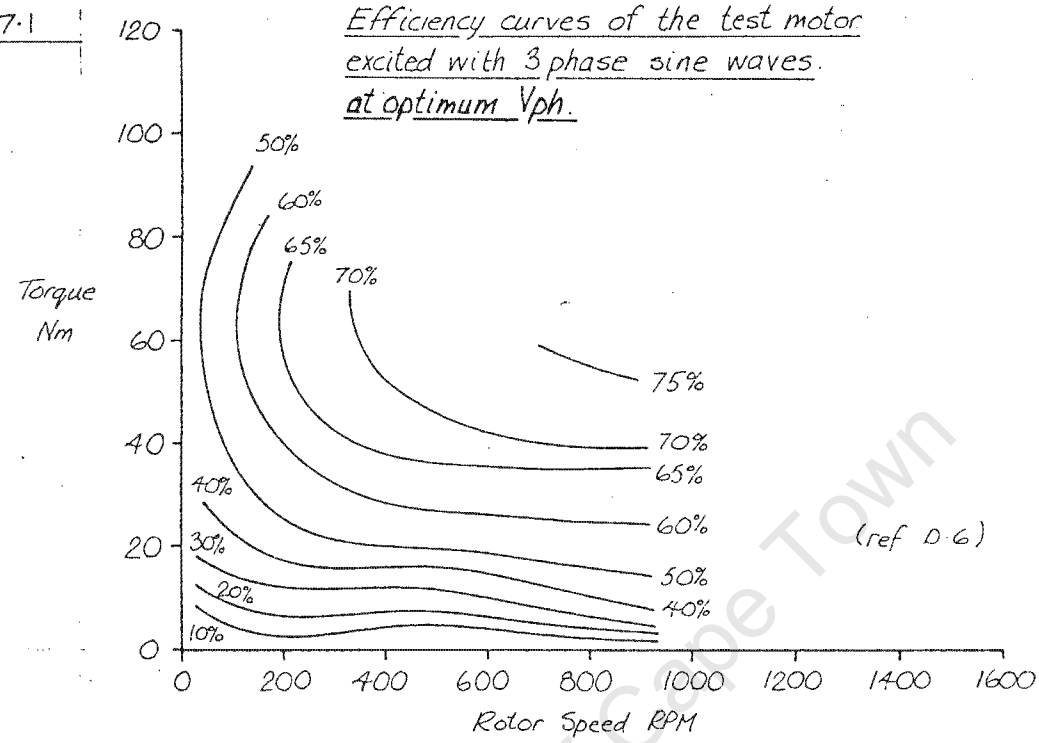

FIG 7·2

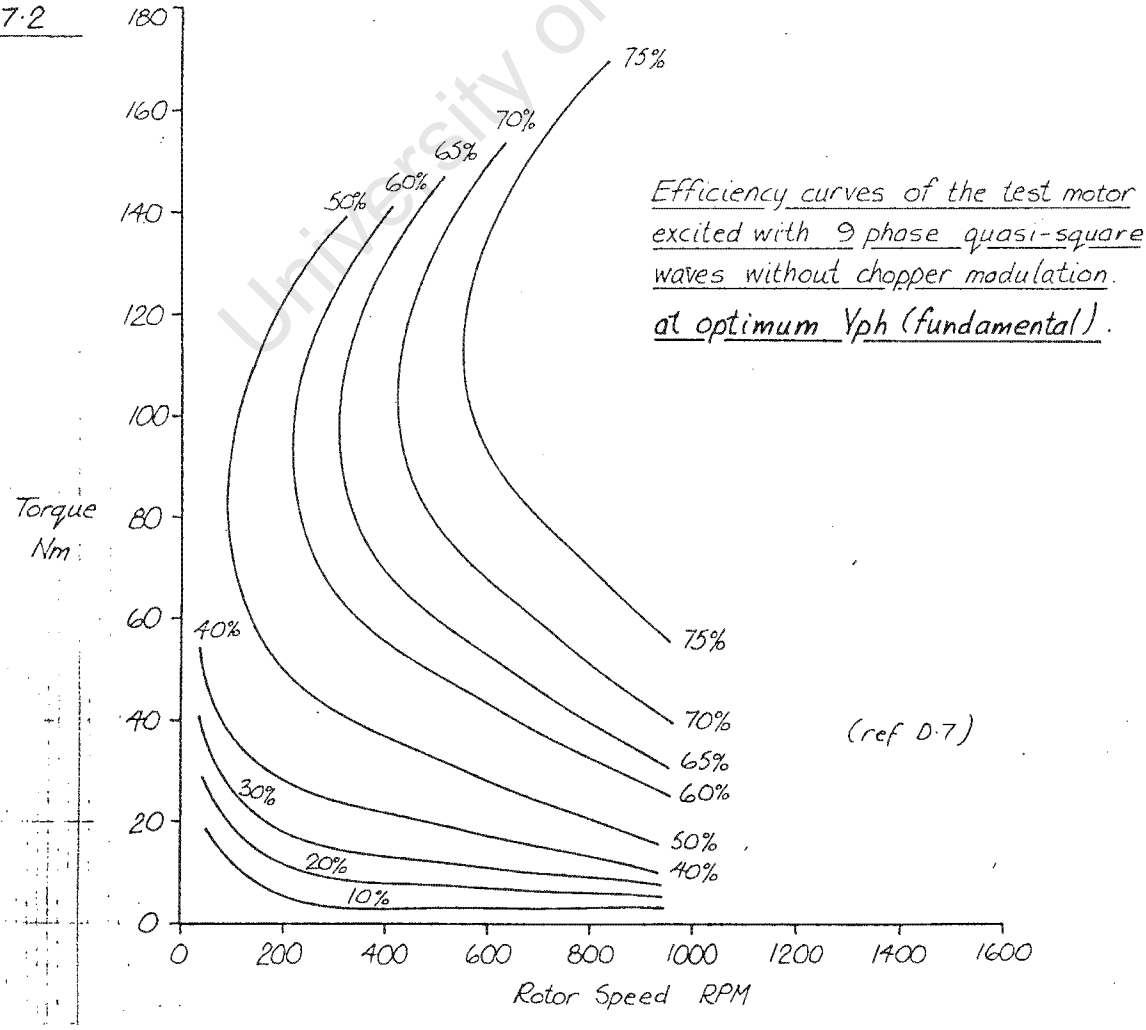

7.3 Optimizing the motor performance over the complete operating range.

Until now the performance comparisons of the 3-phase sine and 9-phase quasi-square wave excited motor have been made under conditions of constant phase voltage for a particular frequency. This has caused limitations in the motor's performance especially at low operating frequencies and low torque.

Efficiency contours plotted against torque and rotor speed are shown in figures 7.1 and 7.2 for optimum excitation (optimum excitation refers to the amplitude of the applied phase voltage - it does not mean that optimum motor performance is neccessarily achieved). Although limitations were placed on the range of sinusoidal measurements, the inherent limitations in using unmodulated quasi-square waves can be seen. The quasi-square wave excited motor, when compared to the sinusoidally excited motor, suffers from reduced efficiency over the complete operating range, and the low torque-low speed range in particular.

It has previously been noted that reduced excitation caused an increase in peak efficiency which is looked at more closely in figures 7.3a and b. It immediately becomes apparent that the original proposition that excitation voltage amplitude is proportional to frequency must be modified. For the most efficient performance over the complete torque range of the 9-phase quasi-square wave excited motor, ie. between zero and maximum torque, it is also neccessary to vary the excitation amplitude as torque changes.

At 5 Hz an efficiency of between 47% and 52% can be maintained over the major portion of the torque range and, at 10 Hz the efficiency lies between 60% and 66%. The same applies to the motor when sinusoidally excited and figure 7.4 shows that at 5 Hz the efficiency can remain between 54% and 56%.

Due to the increased slip at reduced excitation it is neccessary to increase the operating frequency slightly to keep the speed constant. The increase at 5 Hz is less than 0.5 Hz and at 40 Hz less than 2 Hz.

The efficiency contours plotted against torque and rotor speed for 9-phase quasi-square wave excitation (see figure 7.5) now become vertical lines of approximately constant efficiency. By optimizing the excitation voltage amplitude for torque as well as frequency a vastly improved motor performance is achieved.

Figure 7·3 - Efficiency vs Torque for motor excited with different amplitude quasi-square waves at a) 5Hz b) 10Hz

a)

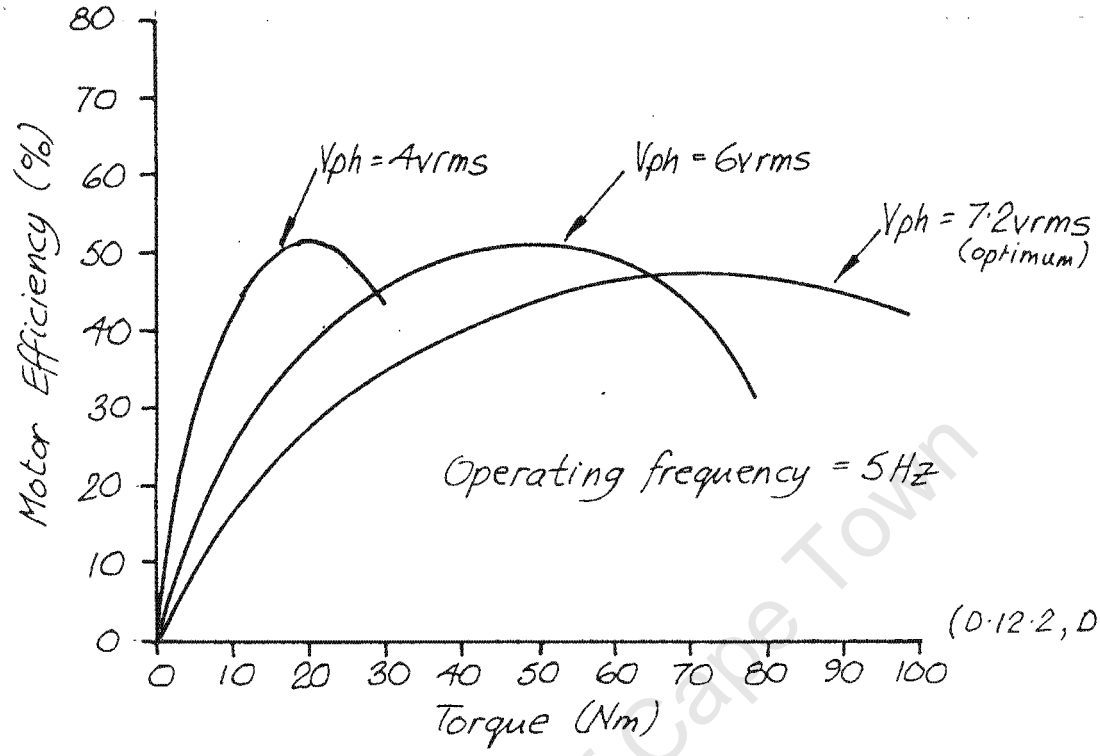

Vph	Vdc(aver)
4v	4·5v
6v	7·1v
7·2v	8·4v

(D·12·2, D·12·1, D·7·1)

b)

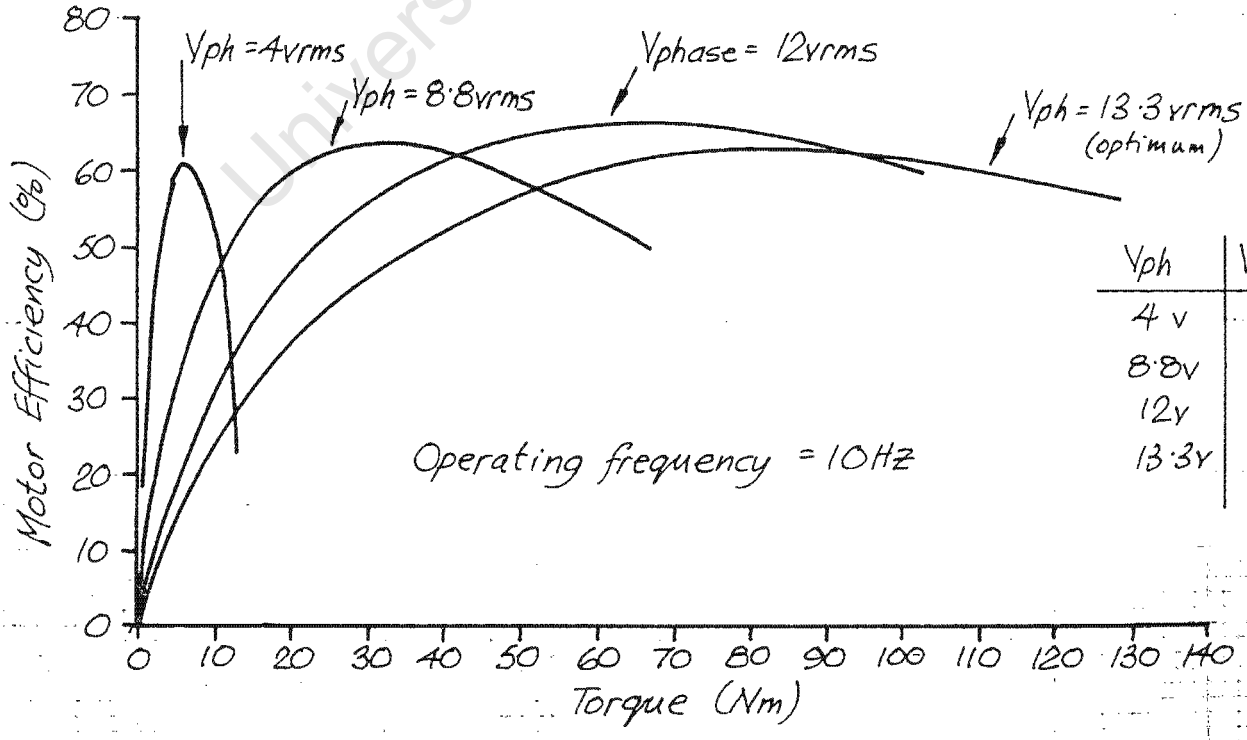

Vph	Vdc(aver)
4 v	4·8v
8·8v	10·2v
12v	13·5v
13·3v	15·2v

(D·12·6, D·7·4, D·12·4, D·7·3)

Figure 7·4 - Efficiency vs Torque for motor excited with different amplitude sinusoidal waves at 5Hz

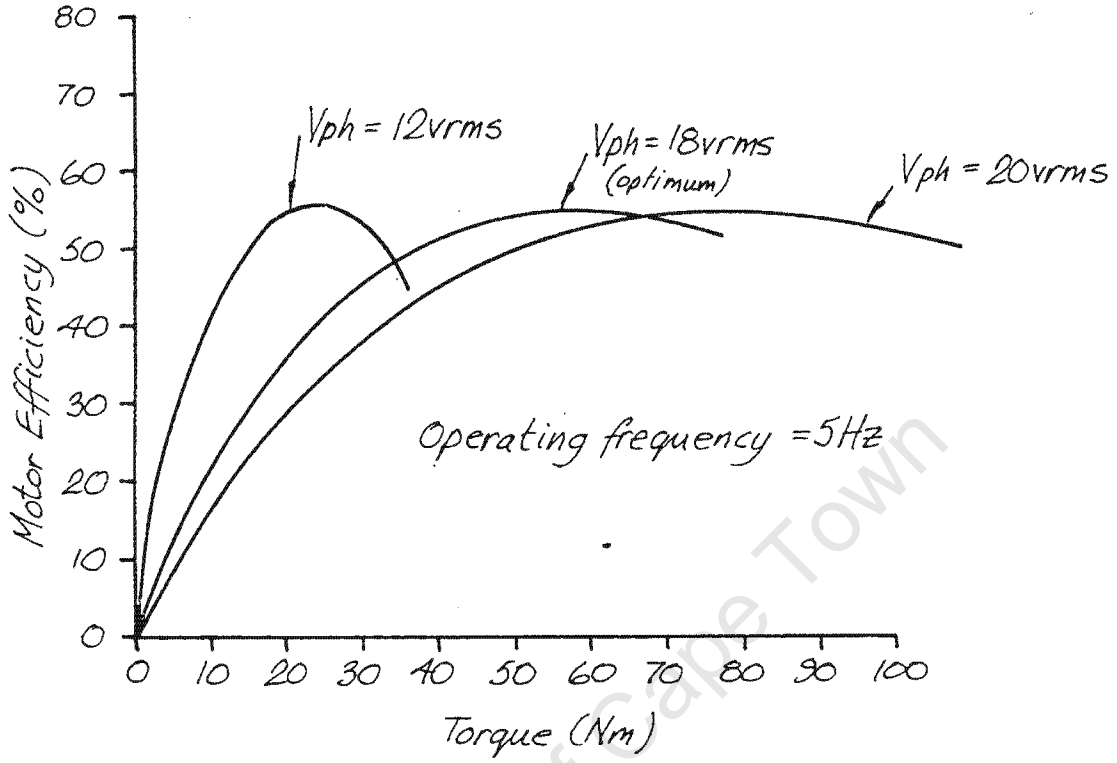

Figure 7·5 - Efficiency curves of the test motor excited with unmodulated 9-phase quasi-square waves and amplitudes optimized for peak efficiency.

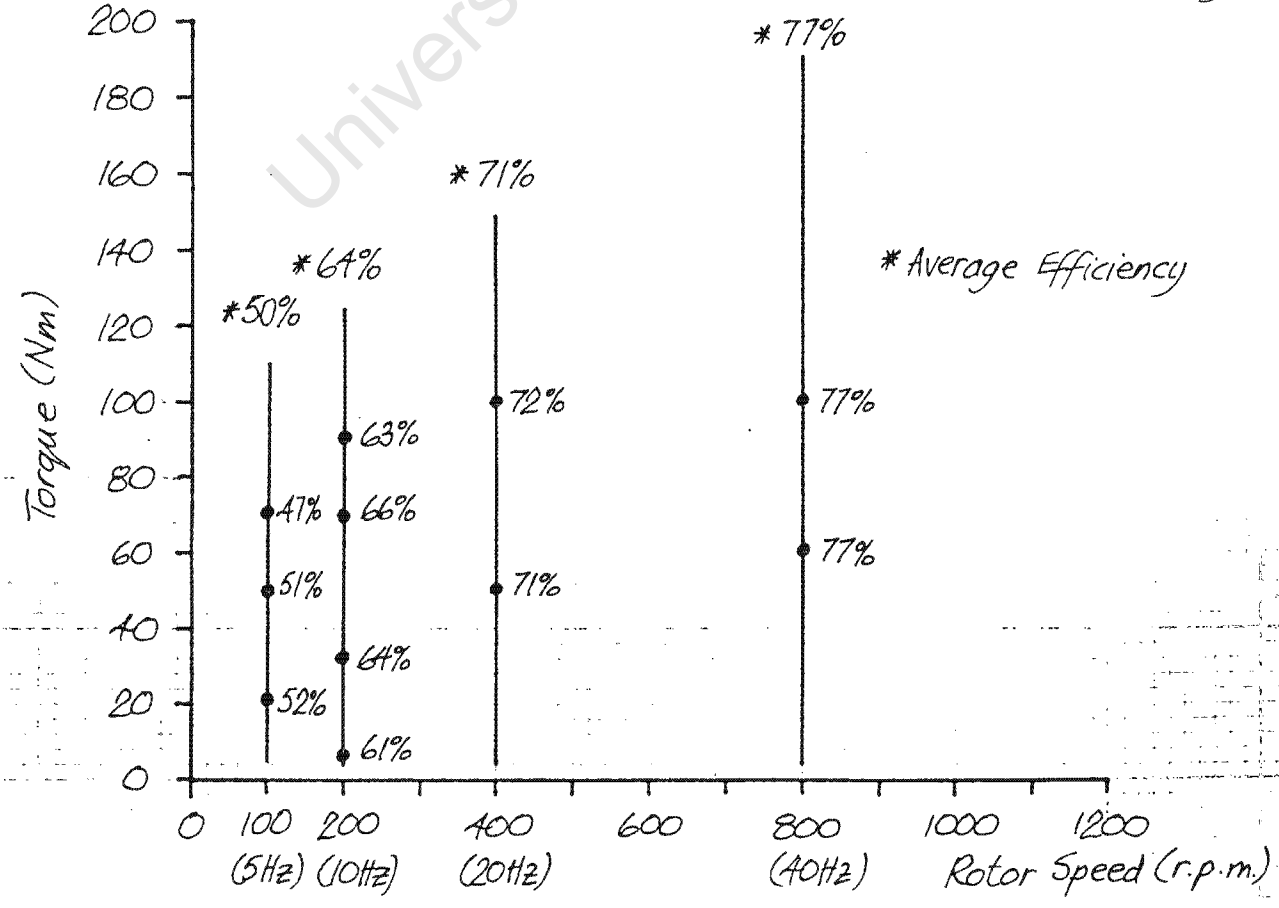

7.4 Power losses within the motor and system.

So far it has been shown that the 9-phase motor produces slightly more torque but at a lower efficiency than an equivalent 3-phase sinusoidal motor (refer to equations 7.1 and 7.2) meaning that the 9-phase excited motor accommodates a larger power loss as a direct result of the additional harmonics. Figure 7.6 gives the relative 9-phase inverter loss, motor loss and output power when the machine is developing a torque of 50 Nm for various frequencies and compares them to the 3-phase motor developing the same torque. At this particular torque, the total motor losses for the 9-phase driven machine exceed, by approximately 30%, the total motor losses of the 3-phase sinusoidally driven machine. In addition the 9-phase system has an inherent and approximately constant power loss of 300 watts in the bridge inverter system.

Table 7.3 gives a breakdown of the sinusoidally excited motor losses shown in figure 7.6.

Table 7.3

Breakdown of 3-phase sinusoidal motor losses (refer figure 7.6) at an output torque of 50 Nm and optimum excitation.

	5 Hz	10 Hz	20 Hz	40 Hz
Total input power	900	1600	2950	5500
Output power	480	1000	2050	4200
Total motor losses	412	590	885	1270
Total stator loss	376	553	851	1236
Stator copper loss	306	375	460	460
Stator iron loss	70	178	391	776
Rotor loss	36	37	34	34
Wind.& fric.loss	8	10	15	30

(Watts)

FIG. 7.6 (Ref. C.1)

Power losses in a 3phase sinusoidal driven system and a 9phase quasi-square wave driven system. at optimum excitation voltage.

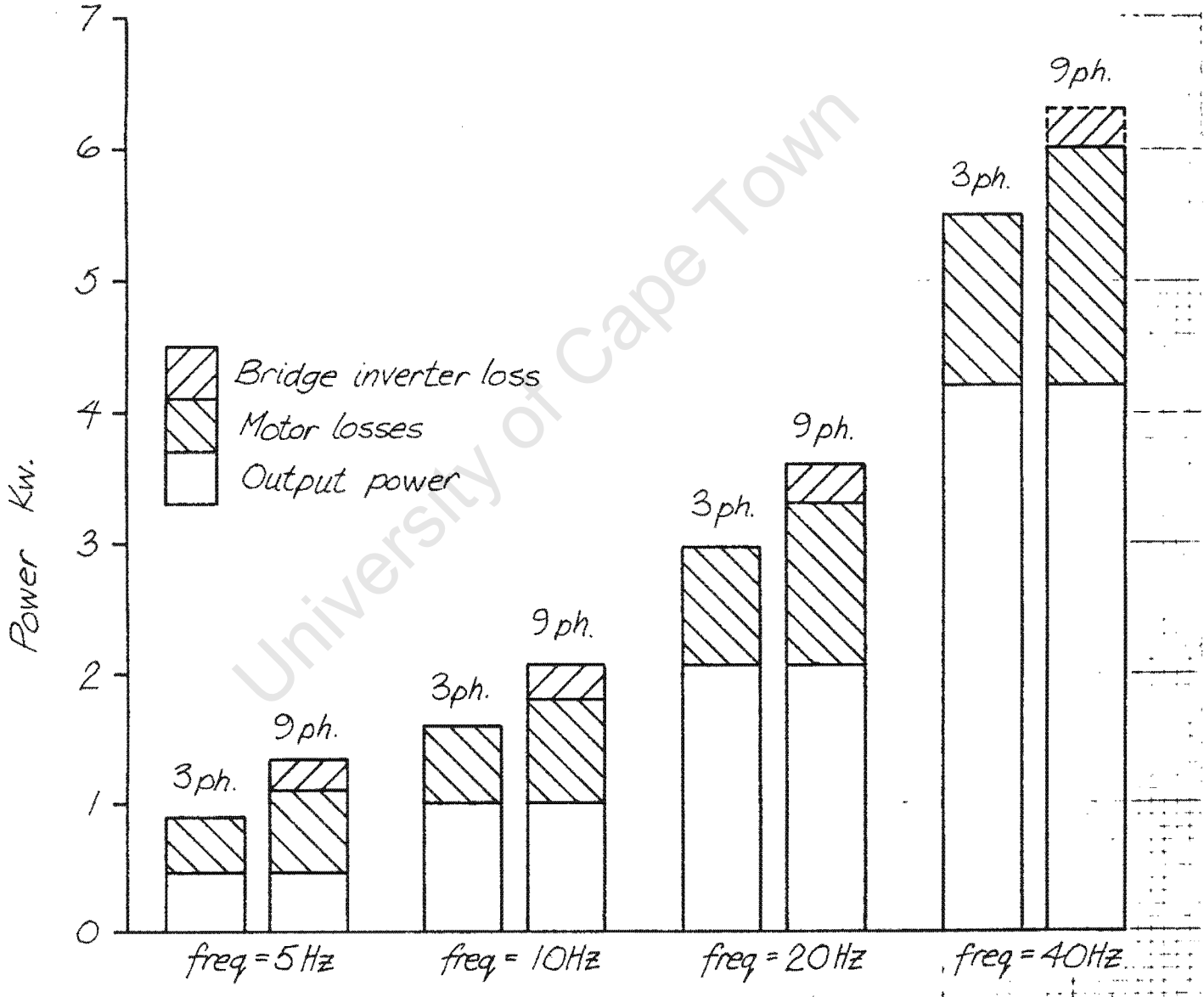

Note: Torque output at all frequencies = constant = 50Nm.
9phase fundamental rms phase volts = 1/3 x 3-phase rms phase volts.

The formulae used to derive the results in table 7.3 are :-

Input power Pi = Measured from graphs of appendix C.1

Output power Po = Measured from graphs of appendix C.1 ($T.\omega_r$)

Total motor losses = Pi - (Po + Windage & friction)

Stator power loss = Pi - $T.\omega_1$

Stator copper loss = $3I_1^2 R_1$

Stator iron loss = Pi - $T.\omega_1$ - $3I_1^2 R_1$

Rotor power loss = $T.\omega_1$ - (Po + Windage & friction)

Windage & friction = Obtained from open circuit tests

Airgap power loss = Approximated to zero

Figure 7·7 – Sinusoidal motor losses for constant torque

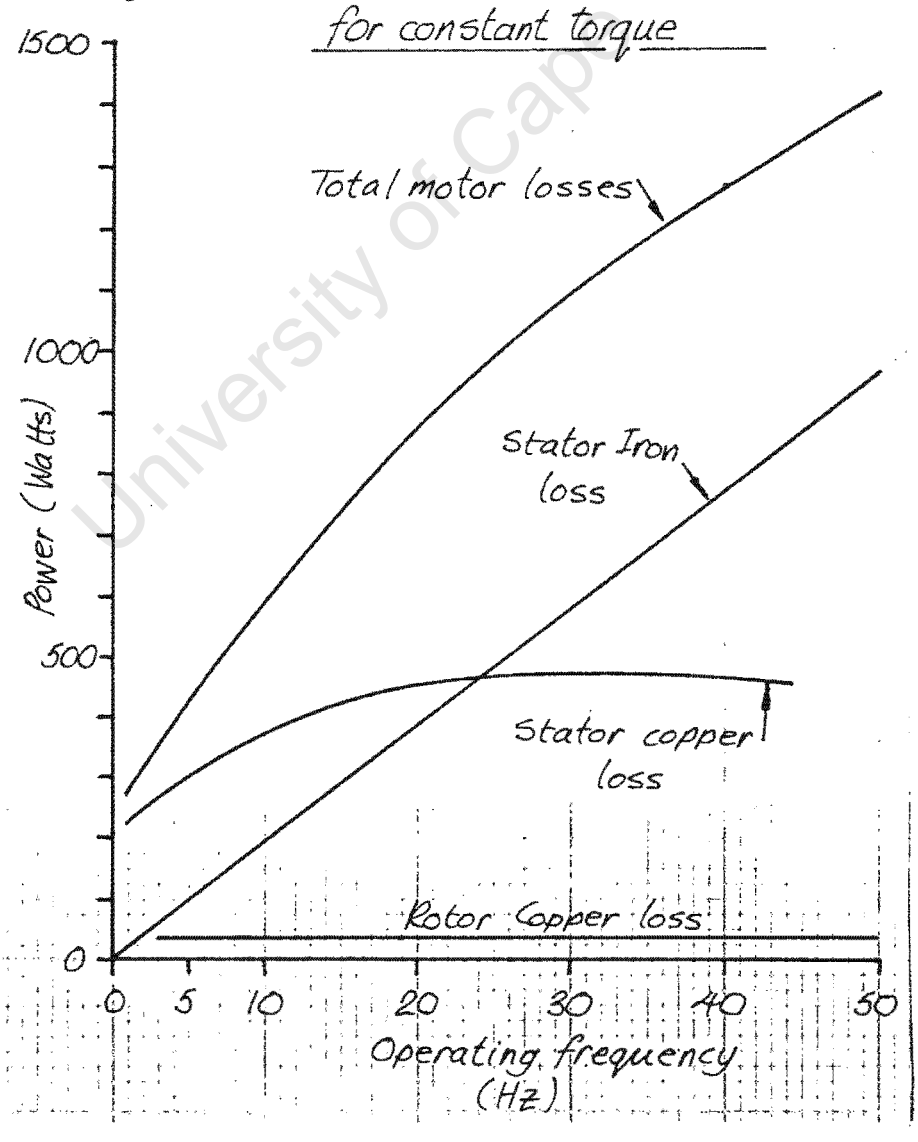

Points to note for constant torque operation and sinusoidal voltage excitation are:-

(i) At frequencies of 5, 10, 20 and 40 Hz the phase currents are 24.2, 26.8, 29.7 and 29.7 amps respectively.

(ii) The relationship between stator copper loss and iron loss is shown in figure 7.7. Iron loss is made up of hysteresis loss (proportional to $f.B^n max$ where n is between 1.6 and 2) and eddy current loss (proportional to $f^2.B^2 max$). Iron losses, according to figure 7.7, are linearly related to frequency thus indicating that hysteresis losses predominate.

(iii) Low rotor frequencies of 0.40, 0.36, 0.32 and 0.31 Hz for 5, 10, 20 and 40 Hz operating frequency mean that rotor iron losses will be negligible and the rotor losses mainly copper losses. These are small due to the low rotor frequency and approximately constant.

The harmonic losses due to the application of quasi-square wave excitation are, however, more complex and difficult to allocate.

Table 7.4

Power contribution by harmonics of a quasi-square wave form (3-phase freewheel = 60 deg.,9-phase freewheel = 31.4 deg.) (D.12)

Harmonic	3-phase,10Hz	9-phase,10Hz	9-phase,40Hz
1	96.6%	93.8%	95.0%
3	0	5.5%	4.3%
5	0.6%	0	0
7	1.9%	0.1%	0
9	0	0.4%	0.4%
11	0.8%	0.2%	0.2%

Figure 7.8 Magnitude and phase relationship of the time harmonic components of voltage, current and power flowing into the motor. Actual waveforms are shown in figures 3.12a,b and c.

	67·5 Nm 3 Phase, 10 Hz	86 Nm 9 Phase, 10 Hz	106 Nm 9 Phase, 40 Hz
Fundamental Volts	22·7	11·5	47·0
Fundamental Amps	30·9 ∠-30·9°	28·6 ∠-41·3°	33·3 ∠-48·7°
" Watts/phase	602·2	247·6	1033·8
3rd harm. Volts	0·3	2·8	12·2
Amps	0·5 ∠-18·0°	10·9 ∠-62·2°	12·6 ∠-72·5°
Watts/phase	0·1	14·4	46·3
5th harm. Volts	3·4	0·9	2·3
Amps	2·7 ∠-66·9°	2·6 ∠-87·7°	1·4 ∠-86·0°
Watts/phase	3·6	0·1	-0·2
7th harm. Volts	6·6	0·2	2·7
Amps	5·0 ∠-68·8°	2·9 ∠-66·2°	3·6 ∠-88·0°
Watts/phase	12·0	0·2	0·4
9th harm. Volts	0·2	1·0	3·5
Amps	0·6 ∠-8·9°	4·2 ∠-76·6°	4·5 ∠-74·7
Watts/phase	0·1	1·0	4·1
11th harm. Volts	5·2	1·2	4·6
Amps	2·9 ∠-70·9°	4·0 ∠-82·5°	3·6 ∠-83·7°
Watts/phase	4·9	0·6	1·8
Total rms Volts	24·7	12·1	49·2
Amps	31·6	31·5	36·3
Watts/phase	623·5	264·1	1087·7
Marek rms Volts	27·4	13·3	51·4
Amps	33·2	32·4	37·5
Watts/phase	730·0	303·5	1220

Up to 19th harmonic accounted for.

FIG. 7.9

ACTUAL WAVEFORMS OF RESULTS GIVEN IN FIGURE 7.8

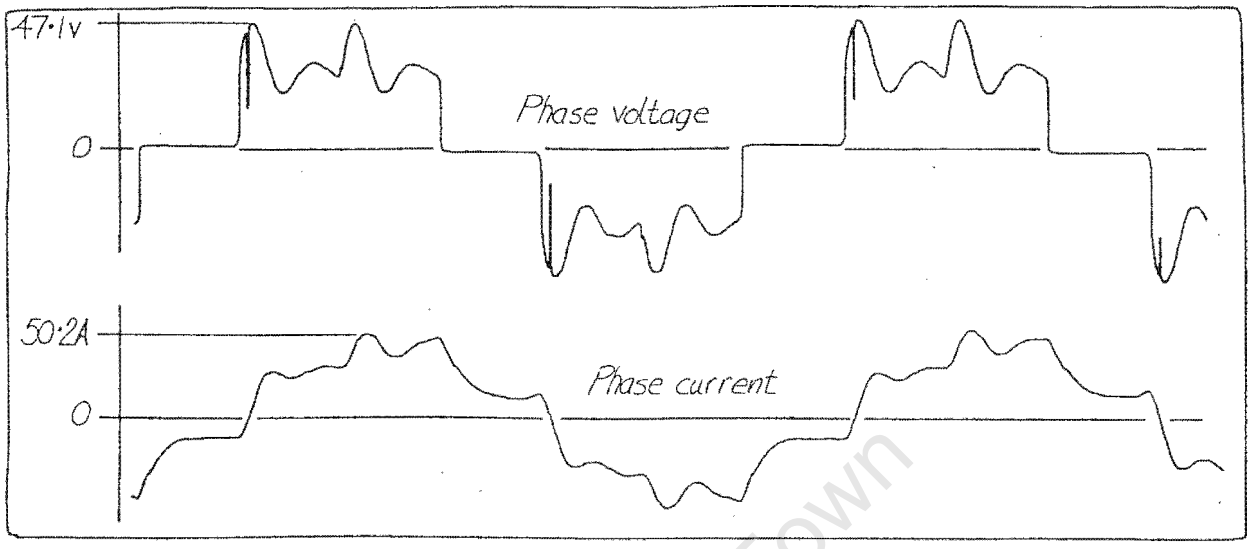

a) 3 Phase 60° freewheel ; 10Hz ; Torque = 67·5Nm FIG. 7.9a

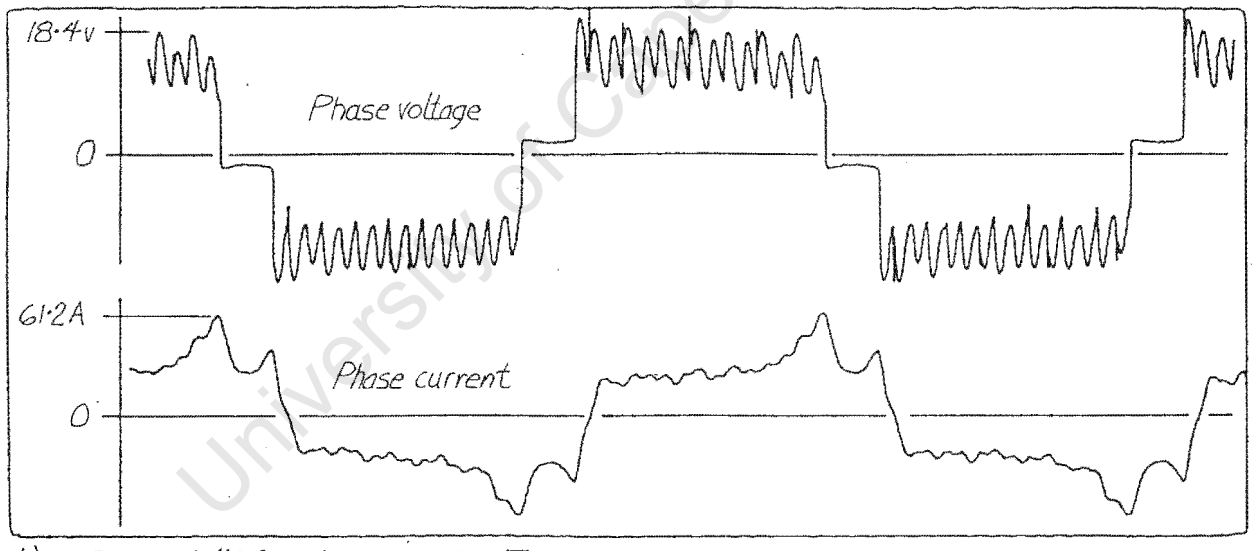

b) 9 Phase 31½° freewheel ; 10Hz ; Torque = 86Nm FIG 7.9b

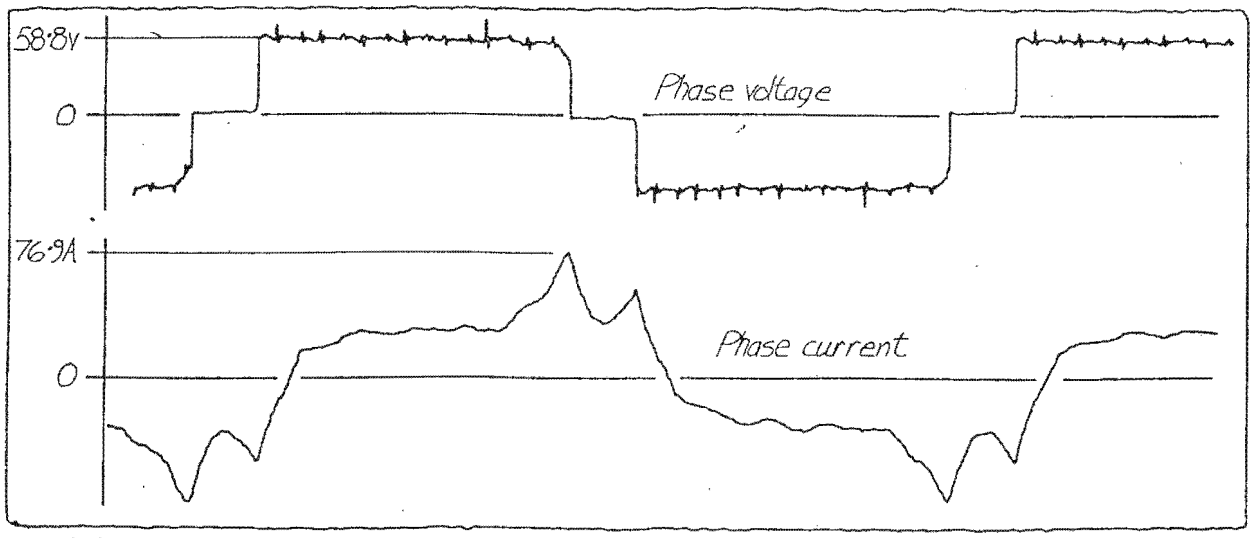

c) 9 Phase 31½° freewheel ; 40Hz ; Torque = 106Nm FIG 7.9c

With the aid of an harmonic analyser (17), the magnitude and phase relationship of the time harmonic components of voltage, current and power flowing into the motor could be determined (see figures 7.8 and 7.9a, b and c). A check on the reading was made with a Marek power analyser (which has an accuracy of 0.5% between 0 and 50 KHz), and these are included in figure 7.8. The percentage contribution to the input power by each harmonic is given in table 7.4 and from this and figure 7.8, the following conclusions can be drawn.

(i) The fundamental power component carries the majority of power to both the 3-phase quasi-square and the 9-phase quasi-square induction motor.

(ii) The absence of 3rd and 9th harmonic contributions in the 3-phase quasi-square motor results from using a 60 degree freewheel period (refer A.5.2, α = freewheel period + $\pi/3$ = 120 degrees).

(iii) Fifth and 9th harmonic contributions in the 9-phase quasi-square motor are low due to the freewheel period of 31.43 degrees (refer A.5.6, α = freewheel period + $\pi/9$ = 51.4 degrees).

(iv) Theoretically, at α = 51.4 degrees, a certain amount of 5th harmonic contribution should occur. It does not because the formula for determining α is innacurate for 9-phase high torque operation.

(v) In the 3-phase motor the very small amount of power supplied by the 3rd and 9th harmonics is almost entirely for a resistive load. Reactive VARS are supplied to the 9-phase motor by the 5th and 7th harmonics (refer figures 7.8 and 7.10).

Figure 7.10 Current harmonic phase relationship with respect to fundamental voltage for 9-phase, 10 Hz operation at 86 Nm torque.

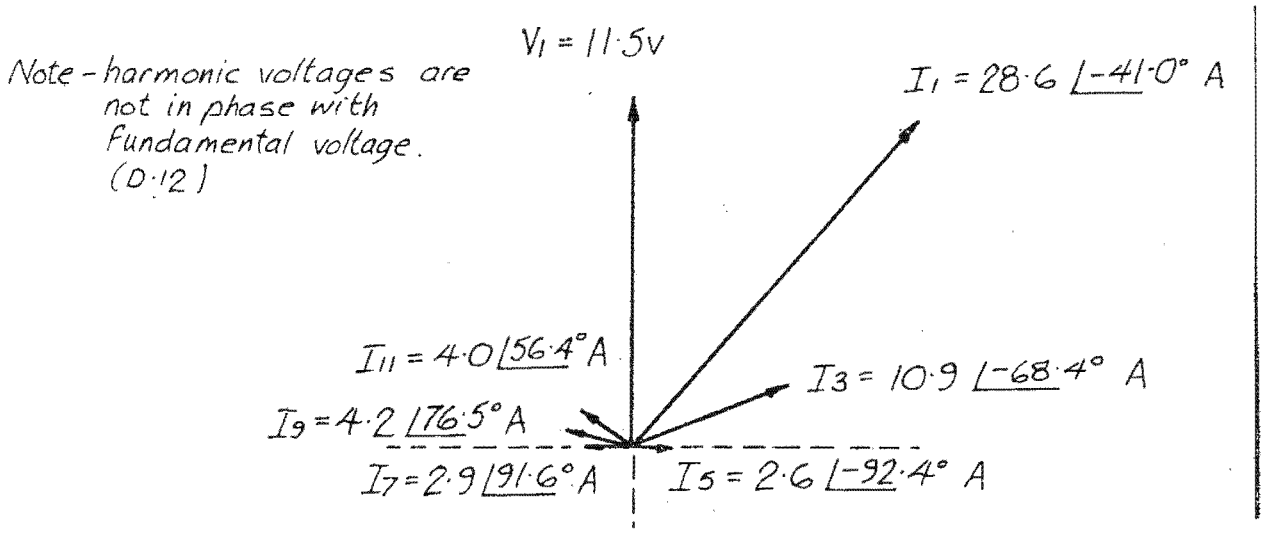

(vi) The accuracy of the harmonic measurements can be judged by comparing the actual current and voltage waveforms (figure 7.9) with those built up using the measured harmonic components (D.12).

The allocation of power losses in the quasi-square wave excited motor operating at 10 Hz and developing 50 Nm can now be looked at more closely and compared to the losses developed in a 3-phase sinusoidally excited motor also operating at 10 Hz and developing an output torque of 50 Nm (refer figure 7.6).

From table 7.4 for 9-phase quasi-square wave operation at 10 Hz, the fundamental power component contribution, at the motors input, was approximately 94% of the total power input. This leaves a contribution by all other harmonics, though mainly the 3rd, of 6%. Using this information the author has constructed a suggested power flow diagram, shown in figure 7.11b, to account for the additional 200 watts lost (see figure 7.6) in the 9-phase driven motor as a result of using quasi-square wave excitation. For comparison purposes the 3-phase sinusoidal driven motor power flow diagram is shown in figure 7.11a. The additional assumptions made are:

i) The ratio of normal motor losses to input power for both the fundamental and the harmonic power components of the 9-phase system is the same as that for the 3-phase sinusoidal system ie. 590/1600.
ii) The fundamental power component supplies power to compensate exactly for the reverse and fast forward power components generated by the additional harmonics.
iii) The reverse power components developed by the fundamental time harmonic are negligible.

The various power allocations within the motor were calculated using the following formulae:

$$\frac{\text{Fundamental losses } (W_{1,1})}{\text{Fundamental input } (W_1)} = \frac{590}{1600} = \frac{\text{Harmonic losses } (W_{3,1})}{\text{Harmonic input } (W_3)} \qquad (7.3)$$

$$\text{Fundamental compensation loss } (W_{1,2}) = \text{Harmonic reverse loss } (W_{3,2}) \qquad (7.4)$$

FIG. 7.11

A) ALLOCATION OF POWER LOSSES IN 3-PHASE SINUSOIDALLY EXCITED SYSTEM

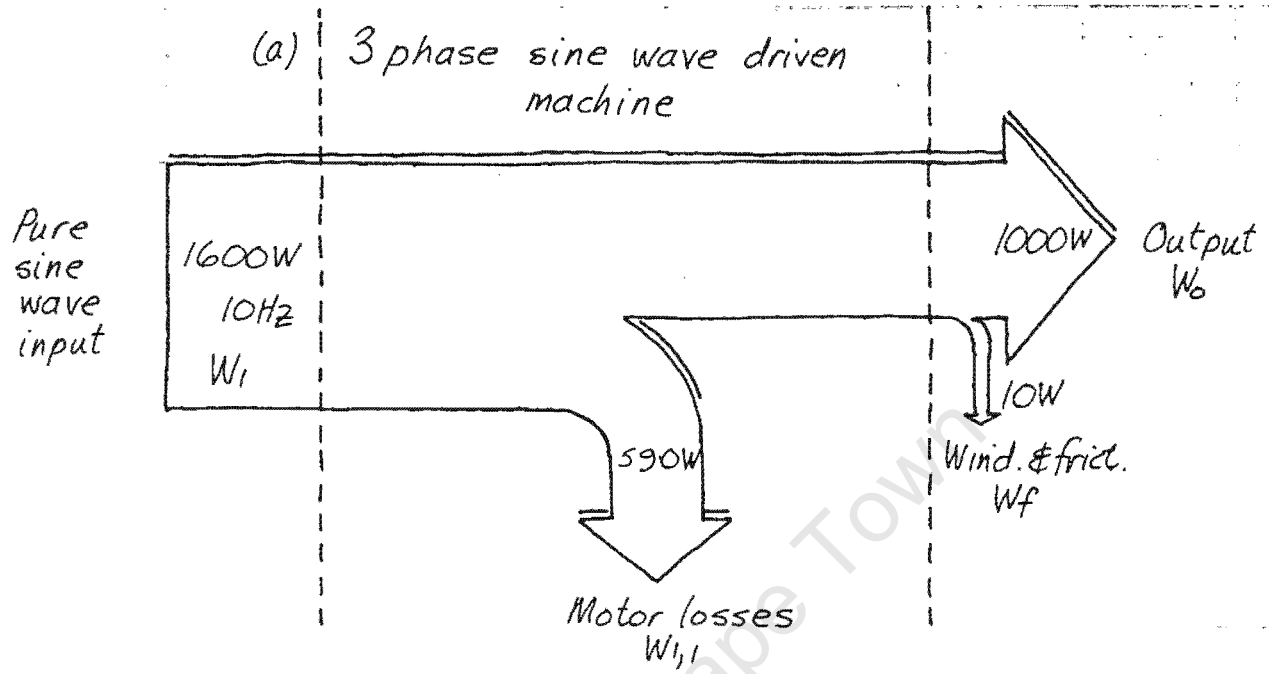

B) ALLOCATION OF POWER LOSSES IN 9-PHASE QUASI SQUARE WAVE EXCITED SYSTEM

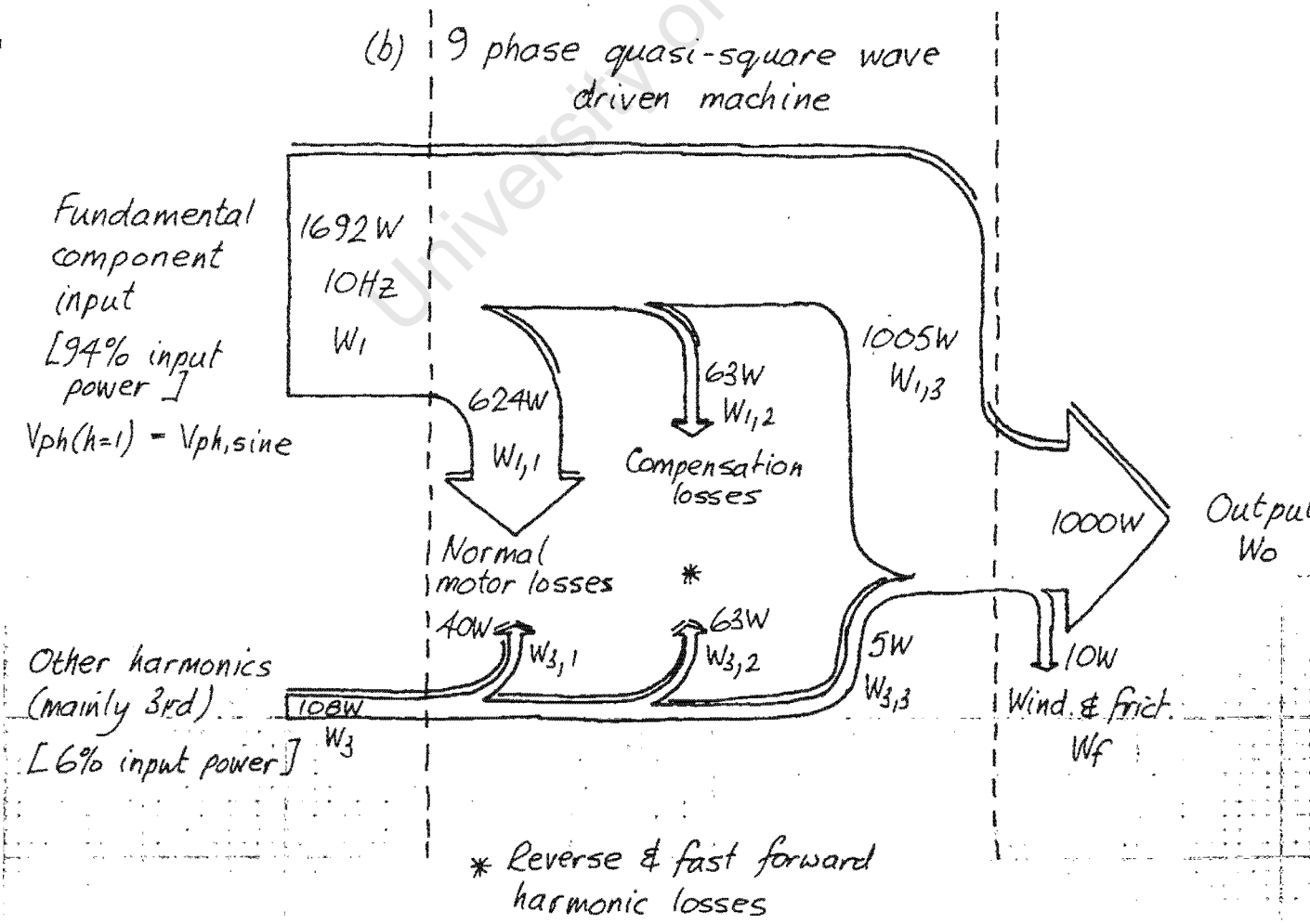

Output + Wind.& Fric (W_o+W_f) = Fundamental and harmonic output contribution $(W_{1,3}+W_{3,3})$ (7.5)

$$W_1 = W_{1,1} + W_{1,2} + W_{1,3} \quad (7.6)$$

$$W_3 = W_{3,1} + W_{3,2} + W_{3,3} \quad (7.7)$$

By substitution and manipulation the power values given in figure 7.11b can be deduced. The efficiency of the fundamental component is 59.4% and that of the other harmonics 4.6%, indicating a gross inefficiency where harmonic inputs are concerned. The measured efficiency, for comparison purposes, including windage and friction as part of the output, is 56.1%. The measured efficiency of the sinusoidaly excited system generating the same output power is, including windage and friction, 63.1%, a difference of 7%.

7.5 Magnetizing current.

Vector diagrams of the motor operating both loaded and unloaded are given in figure 7.12. Because the period of the harmonics is not the same as the fundamental, the harmonic vectors rotate with respect to V_1 and I_1. The harmonic voltages are not shown and it should be noted that they are not necessarily in phase with V_1. No components of less than 1 amp have been shown. The following deductions can be made:-

(i) When the freewheel angle is 20 degrees, all harmonic components greater than the 5th have negligible influence on the output of the motor. The 9th harmonic is actually zero, which agrees with the Fourier analysis of the waveform.

(ii) The vector diagrams for a waveform with a freewheel angle of 31.43 degrees indicate, as a result of the large magnetizing currents at no-load, that the phase voltage is too high and saturation is taking place. This ties up very well with the efficiency results, which show that higher peak efficiencies can be obtained if excitation voltage is reduced.

(iii) At the optimum freewheel angle of 31.43 degrees, more harmonic current components are present.

Figure 7.12 Vector diagrams of the test motor under loaded and unloaded conditions at a)f=40Hz & f/w=20deg b)f=40Hz & f/w=31.43deg c)f=10Hz & f/w=31.43deg.

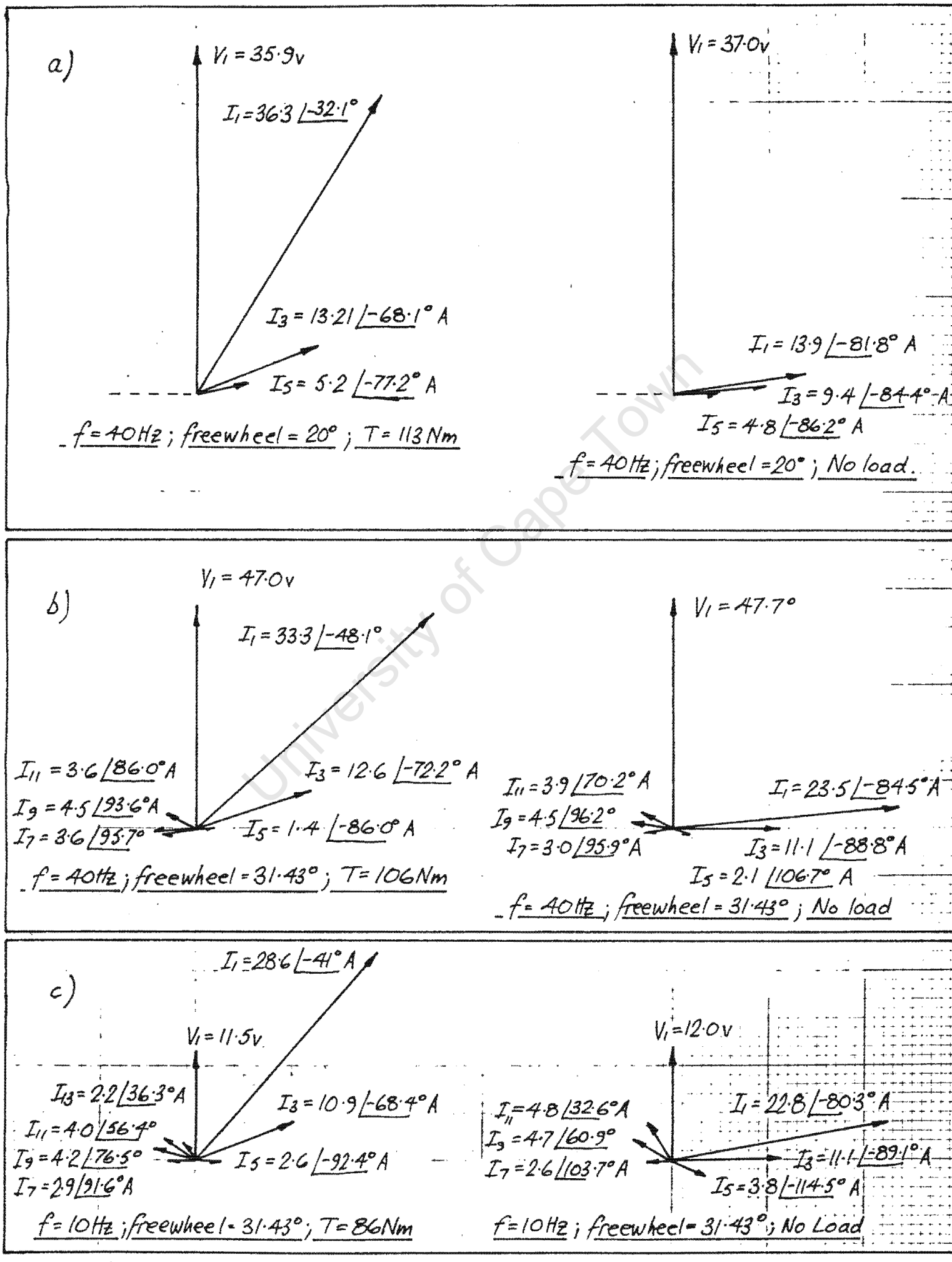

(iv) The harmonic magnetizing currents at no-load are very similar in amplitude and phase to the harmonic currents when the motor is loaded.

The magnetizing current peaks developed by the test motor are, in some cases, not well defined due to the physical construction and winding parameters of the motor rather than the type of excitation waveform.

Tests were conducted on a motor with a double cage rotor, a different winding arrangement and a higher number of turns per stator coil. These differences with respect to the test motor had the effect of lengthening the electrical circuit time constant and thus producing much smoother and well defined waveforms (see figure 7.13a). The motor was excited with a pure square wave voltage of varying amplitude and frequency and measurements taken of the magnetizing current peak height. The results are shown graphically in figure 7.13b.

The conclusion reached is that, within the non-saturated range of the motor, the magnetizing current peak amplitude is directly proportional to the step function of the voltage waveform at a particular operating frequency. If the operating frequency is decreased, the magnetizing current peak height will increase non-linearly with respect to the frequency. Magnetic saturation resulting from high phase currents also causes a non-linear increase in the expected peak height.

These conclusions are equally valid, although not as apparent, for the test motor.

Figure 7.13 Peak magnetizing current test results.

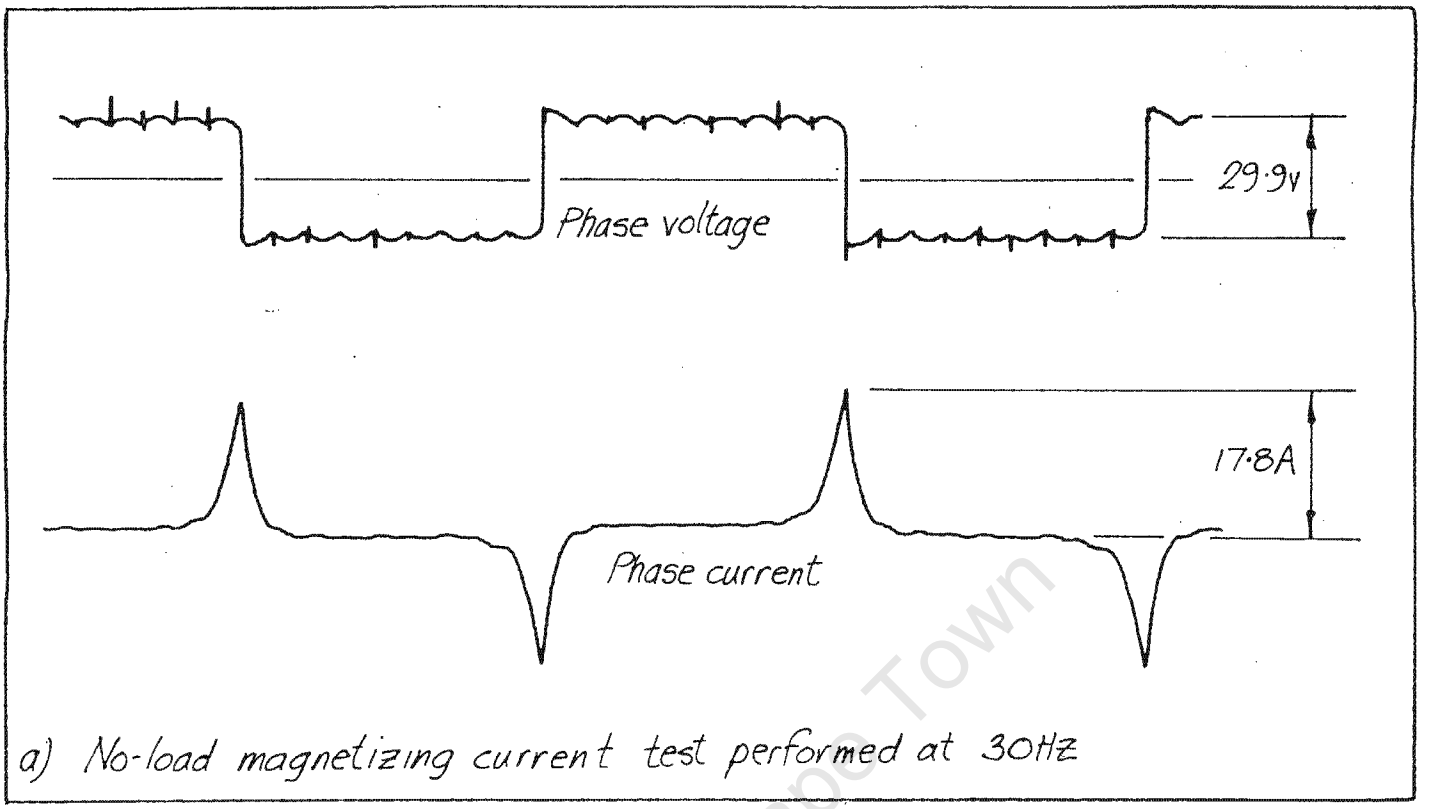

a) No-load magnetizing current test performed at 30Hz

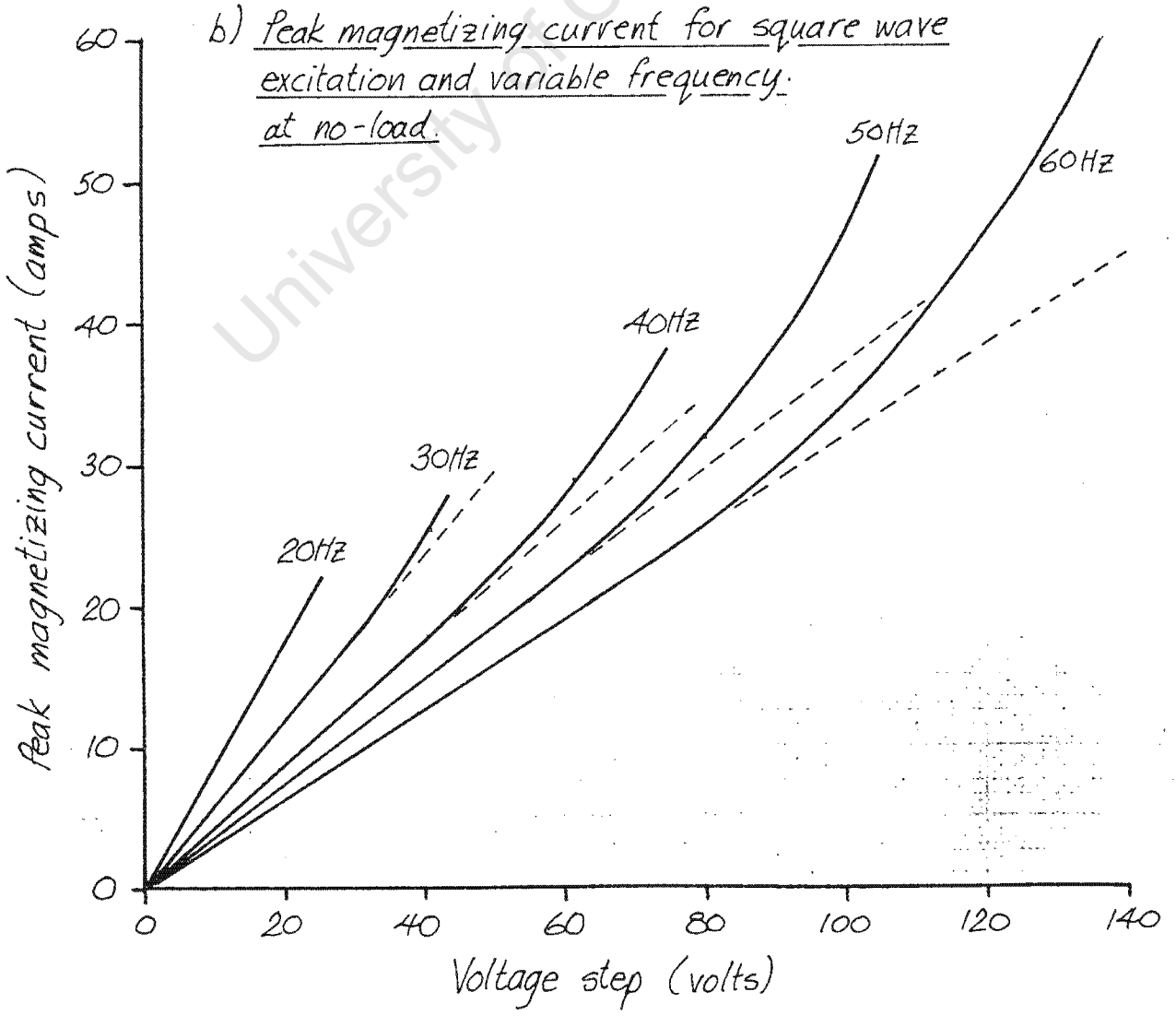

CHAPTER 8.

Results when Test Motor is Excited with Chopper Modulated Quasi-square Voltage Waves.

8.1 Introduction.

Tabulated results for the tests performed within this section are given in appendix D.8, C.4 and C.5. Load tests were performed using the parameters given in table 6.2 relating operating frequency to mark-space ratio where the frequency tabulated was the lowest to be used at its particular mark-space ratio. The freewheel angle for all the tests was 31.43 degrees as determined in section 6.2 and the modulating frequency, unless otherwise stated, remained constant at 1.2 KHz.

8.2 Motor performance characteristics when excited with chopper modulated quasi-square waves.

It has been shown in section 7.3 that the efficiency may be maximized by varying the amplitude of the phase voltage with respect to torque. This can also be done when operating in the chopper modulation mode although only nine voltage levels are available via the variable mark-space ratio. Figures 8.1a, b and c show, for frequencies of 16.6 Hz, 25.0 Hz and 33.3 Hz, which mark-space ratio gives the most efficient performance over a specified torque range. The plot for 8.3 Hz is shown in appendix C.3.1 and can only accomodate a 1/9 mark-space ratio. Extremely high phase currents were obtained if the mark-space ratio, operating frequency parameters in table 6.2 were ignored. For instance at a mark-space ratio of 2/9, frequencies below 16.6 Hz will cause saturation. If the motor is operating at 16.6 Hz, saturation and subsequent high phase currents will occur if the mark-space ratio is increased to 3/9.

Using the results shown in figures 8.1a, b and c and appendix D.8 an efficiency contour graph versus torque and speed has been constructed in figure 8.2. Unlike the previous sine and unmodulated quasi-square wave plots, the limited voltage levels cause discontinuities which have been

Figure 8.1 a & b Efficiency versus torque for motor excited with different mark-space ratio chopper modulated waveforms at a) 16·6 Hz and b) 25·0 Hz operating frequencies

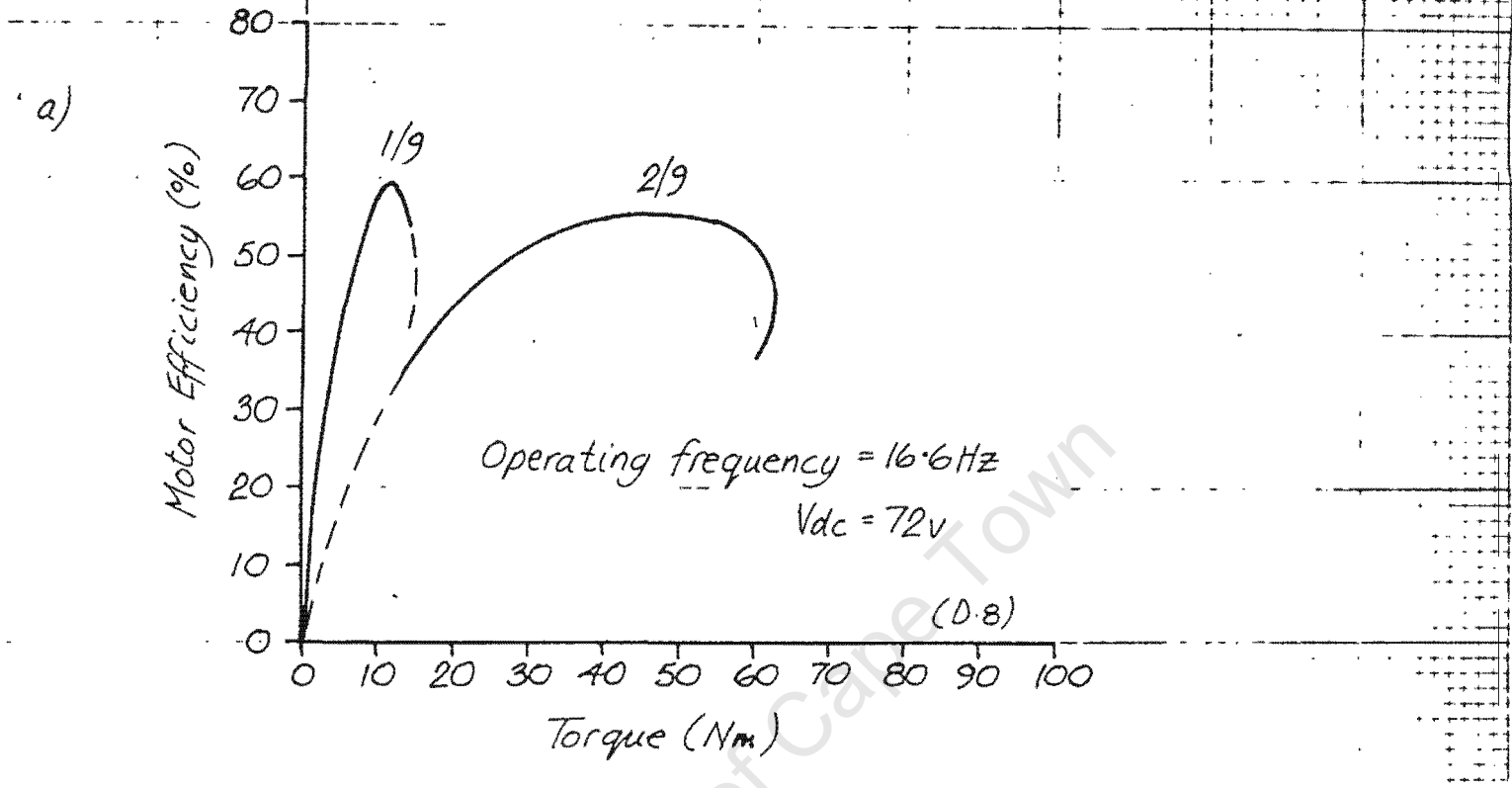

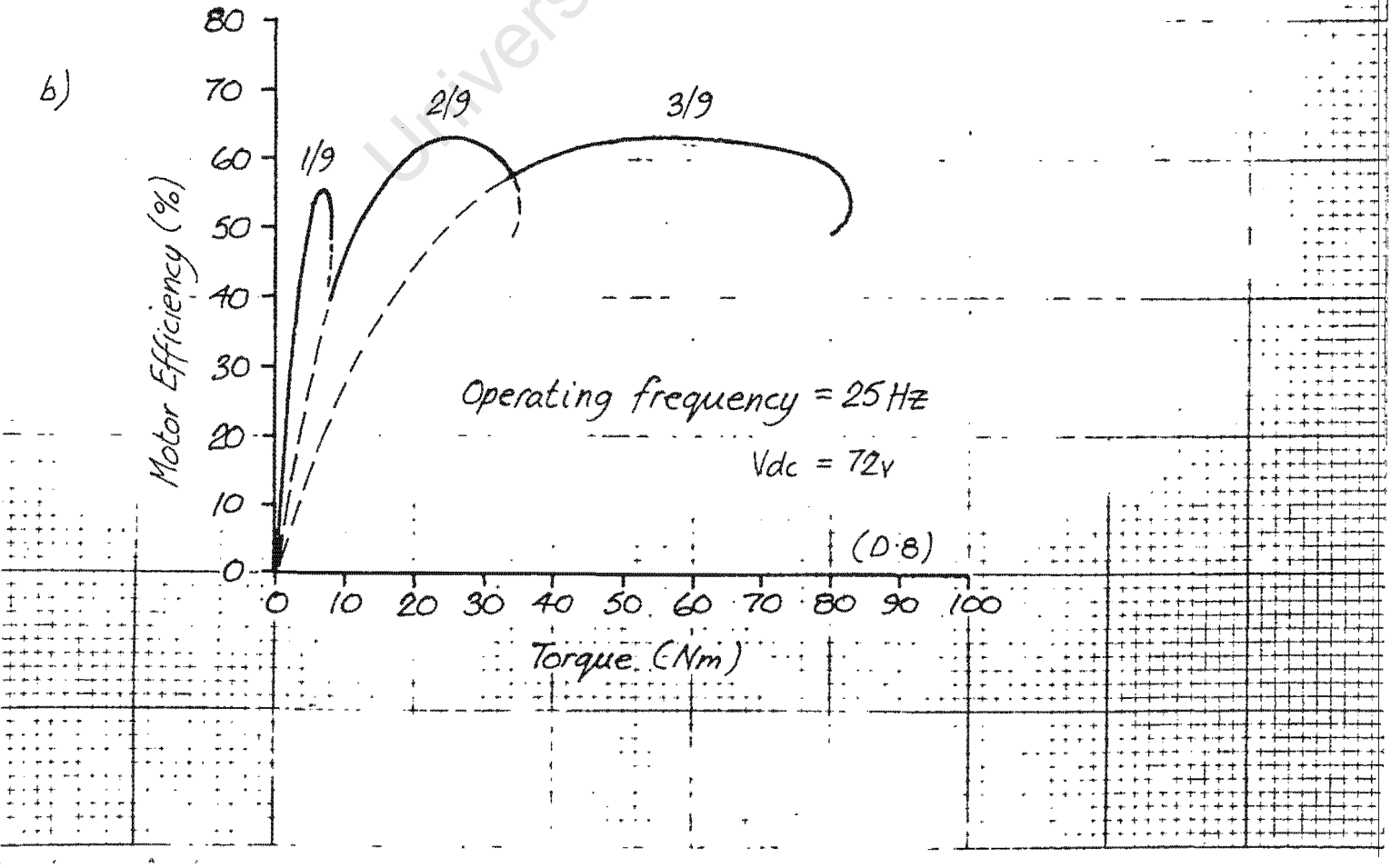

Figure 8·1c Efficiency versus torque for motor excited with different mark-space ratio waveforms at 33·3 Hz operating frequency.

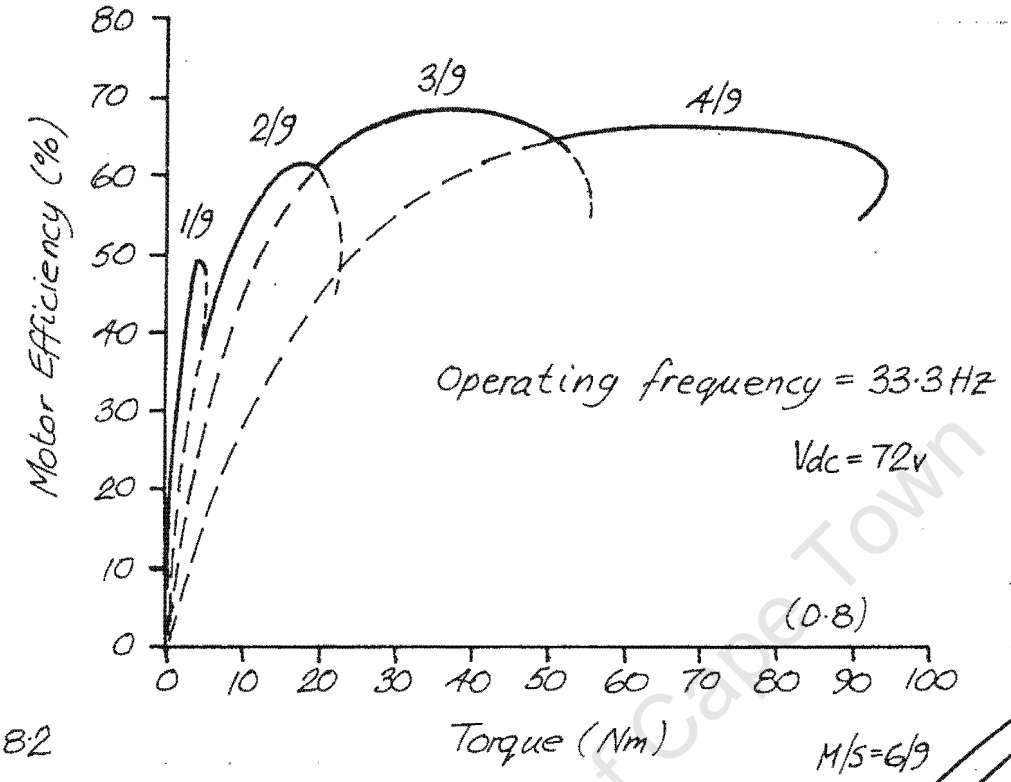

Figure 8·2

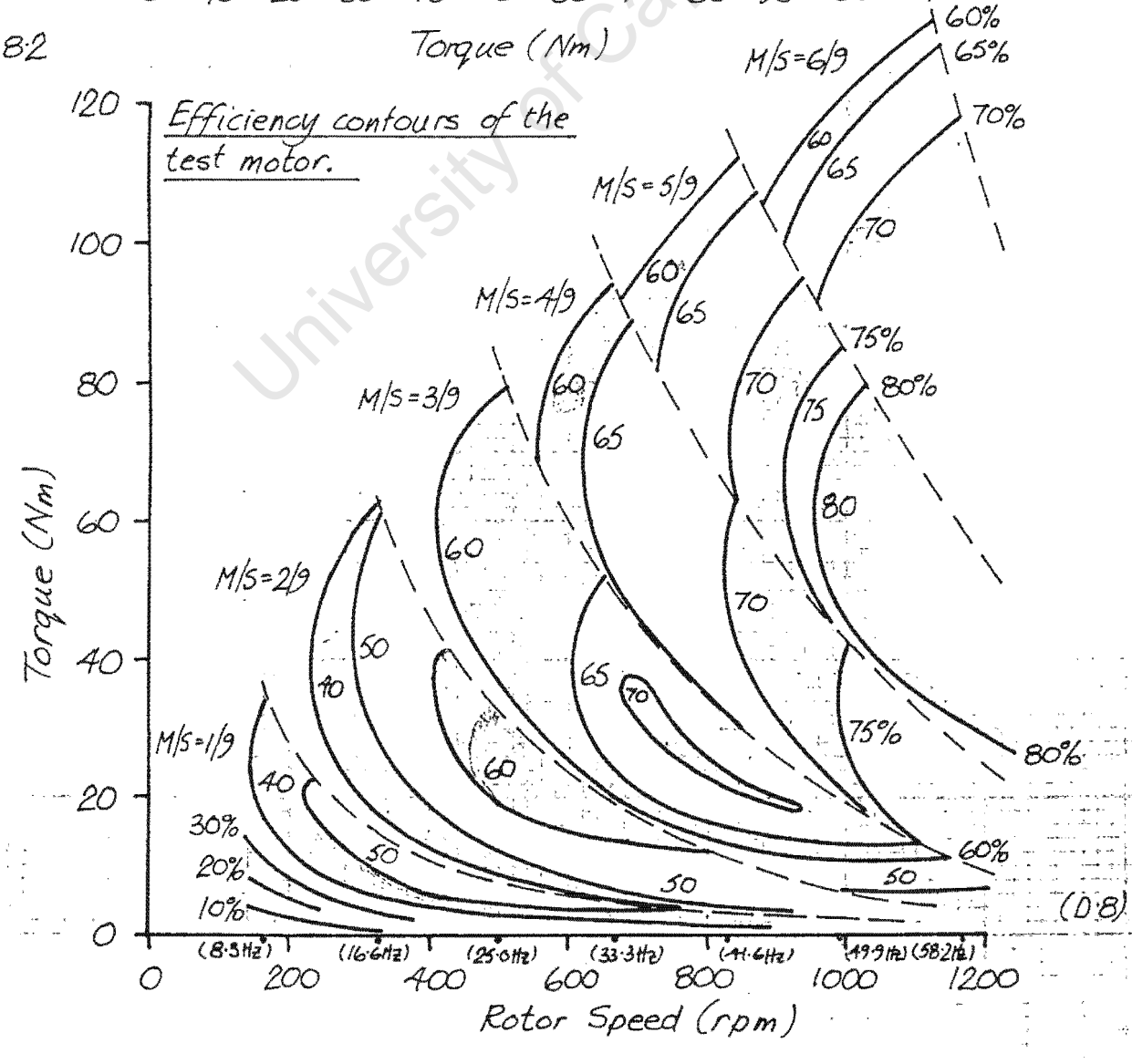

represented on the graph as dotted lines. The discontinuities are in fact mark-space ratio boundaries. With reference to figure 8.2 the following points should be noted:-

(i) The upper right hand boundary of any mark-space region denotes the maximum torque obtainable at that mark-space ratio.

(ii) The leftmost contour line of any mark-space region indicates the minimum frequency that can be used without saturation occuring at that mark-space ratio.

(iii) It is important that if the operating point crosses a boundary while frequency is being decreased, the mark-space ratio must be lowered. If frequency is increased, it will be impossible to cross a boundary unless the mark-space ratio is raised due to the boundary being the maximum torque line.

The following comparisons are made with the sine and unmodulated quasi-square wave efficiency contour graphs shown in figures 7.1 and 7.5:-

(i) The operating frequency cannot be decreased below approximately 8 Hz as a result of the limited excitation voltage amplitudes available.

(ii) Chopper modulation of the quasi-square wave causes a drastic reduction in output torque at the lower speed range of the motor (also refer to section 6.3).

(iii) There are certain operating areas that give a more efficient performance than when the motor is excited with sine waves (see figure 7.1). These areas are shown shaded in figure 8.3 and predominate in the medium to high speed, low torque range of the motor.

8.3 Torque.

Figure 8.2 can be used to show that the limitations placed on efficiency in the lower speed ranges also apply to torque. Appendices C.3.3 and C.3.5 give the actual slip vs torque curves for the frequency range 8.3 Hz to 74.9 Hz and show an almost constant slip window, ie. the slip at maximum torque, of 30 rpm for all operating frequencies. It should be noted that during the chopper modulation tests, unlike the pure quasi-square and sine wave tests, the motor and system did not exhibit large instabilities. Resonance oscillations did occur but the only factor limiting the range of results was maximum phase current.

Figure 8·3 Operating regions of the chopper modulated quasi-square wave excited motor which give a more efficient performance than the sinusoidally excited motor.

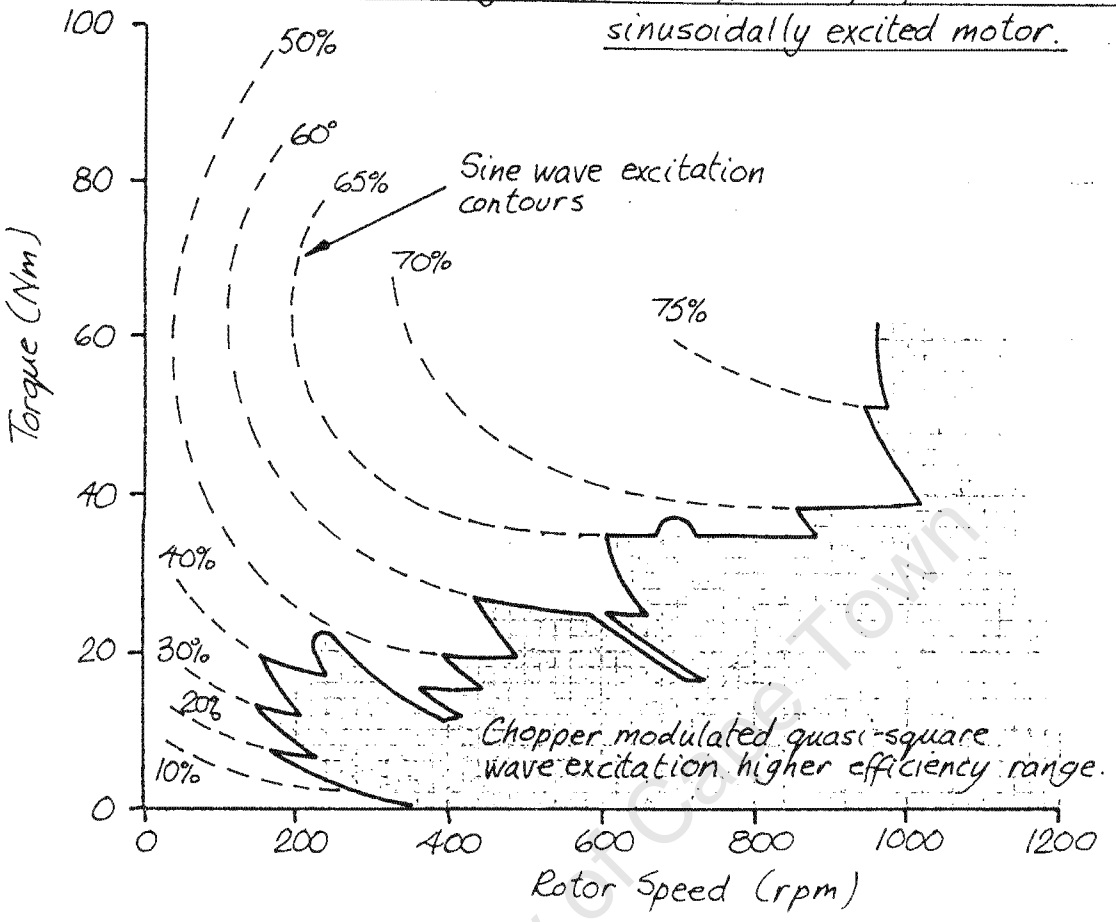

Figure 8·4 Total motor losses against rotor speed for a constant torque of 50Nm.

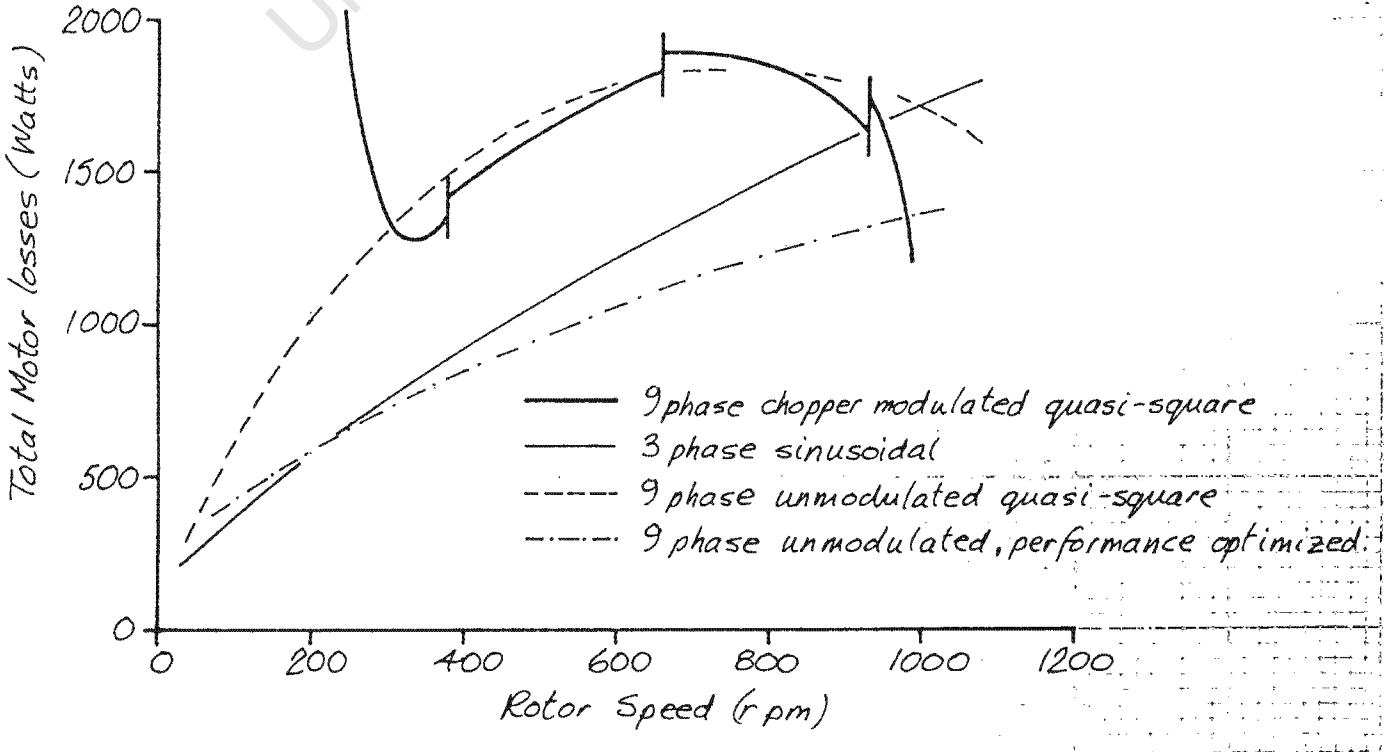

The torque waveforms obtained when the motor is excited with chopper modulated quasi-square waveforms are given in appendix C.5 and conclusions that can be reached when operating in this mode are:

(i) Discounting resonance, which was system derived, the torque pulsations between 8 Hz and 75 Hz are negligable. The very small pulsations that do occur compare favourably with those obtained when the motor is excited with sine waves.

(ii) Pulsations due to the chopper modulation are not apparent in the output torque.

(iii) Although resonance oscillations do appear in the regenerative region, they are not as serious as those obtained with sinusoidal and pure quasi-square wave excitation.

The torque plots are cross referenced with the current and voltage plots given in appendix C.4 and the time bases correlate.

8.4 Power losses within motor and system.

Appendix C.3.6 to C.3.14 show the power allocation within the motor and inverter for the nine operating frequencies and mark-space ratios listed in table 6.2. It should be noted that;

(i) negative torque indicates the motor is being driven above its synchronous speed.
(ii) positive torque indicates it is operating in the motoring region and is driving a load.
(iii) positive power indicates in general, a net current flow from the dc source to the motor.
(iv) negative power indicates in general, a net current flow from the motor to the dc source.

These plots show clearly the dilemma of higher overall system efficiency than motor efficiency with the dc input power being less, in certain areas,

than the ac power into the motor. Tests to determine the reason for this were inconclusive.

From the 8.3 Hz results (ref C.3.6) the motor regenerates currents at large negative torques but the regeneration current is lost in the dc to ac bridge inverter. This particular result is discussed more fully in section 9.2.

During experimentation it was found impossible to reach maximum negative torques due to the very high phase currents being regenerated back into the supply, which caused overheating of the motor.

Figure 8.4 compares the motor losses over the operating frequency range at a constant output torque of 50 Nm (refer to section 7.4 as well) for 3-phase sine, 9-phase unmodulated and 9-phase chopper modulated excitation. The graph shows that:-

(i) Speed cannot be reduced below 250 rpm while an output torque of 50 Nm is maintained due to saturation problems.

(ii) Sinusoidal motor losses exceed those of the 9-phase chopper modulated motor when it is operating above 950 rpm (47.5 Hz). It is important to remember that this occurs at a particular torque of 50 Nm and will not apply at a different torque.

(iii) The motor losses for 9-phase chopper modulated and 9-phase unmodulated quasi-square waves are comparable within the speed range 300 to 900 rpm. If the performance of the latter is optimized its losses decrease substantially.

8.5 Chopper modulated current and voltage waveform analysis.

A full set of current and voltage plots measured directly on a digital oscilloscope are given in appendix C.4. From these plots and in particular C.4.7 to C.4.11 one can obtain a better understanding of the operation of the bridge inverter which was described in section 2.4.

When the motor is loaded normally (ref C.4.7) the phase current can be seen to rise and decay, in a sawtooth fashion, as the dc voltage is switched across the winding and the freewheel period occurs

respectively (refer section 4.1). The current also decays over the programmed freewheel period between positive and negative cycles. As a result of the small magnetizing current peaks at the end of each half cycle and the motors L/R time constant, the freewheel current does not decay to zero. A clearer picture of the magnetizing current can be seen in appendix C.4.22.

During regeneration (ref C.4.8) the phase current decays towards zero as a result of the regeneration back into the supply and 'rises' to a more negative value during the freewheel period. An interesting point to note is that the magnetizing current peaks are still needed at the same time as when the machine was operating in the motoring region under load. Because of this requirement, it can be seen that the motor ceases to regenerate towards the end of each half cycle. During the programmed freewheel period the phase current also increases. Again appendix C.4.23 gives a clearer picture of these magnetizing currents.

The reason for limited, and some times zero, regenerative current when the mark-space ratio is increased above the optimum setting is shown in appendix C.4.11. Because of the longer regeneration time, the current is allowed to decay too much, and, in fact, becomes positive. The current can flow in a positive direction because the bridge inverter transistors, which parallel the regen. diodes, are on at the time. In the case of plot C.4.11 the sawtooth is not completely symmetrical about zero therefore a small regen. current is obtained (see figure 9.4a). At frequencies below approximately 10 Hz, regeneration does not occur (see section 9.2) and the same reasons outlined apply (ref C.4.2). When, at 8.3 Hz, the chopper modulation frequency was reduced (ref C.4.3) to attempt regeneration (see figure 9.2) all that happens is that a larger oscillation about the zero point occurs. The plot in appendix C.4.3 shows how, if the freewheel period is too long, the motor reaches a point where it is unable to sustain the magnetic flux and the rate of increase of freewheel current drops to zero.

CHAPTER 9.

Current Regeneration Capabilities of Test Motor Excited with Chopper Modulated Quasi-square Phase Voltages.

9.1 The effect of regeneration on the dc supply.

When the test motor is excited with unmodulated quasi-square waves while running loaded in its motoring region, a constant dc current is drawn from the supply. As predicted in section 4.1, regeneration does occur during the short underlap periods and figure 9.1b shows the regenerative pulses and subsequent ringing, impressed upon the dc supply. It should be noted that the two pulses shown are developed by different phases while the motor is operating at 25 Hz.

Regeneration back into the supply, when operating with chopper modulated excitation, occurs during the mark period of the modulated waveform (see appendix C.4.8). Because of interlacing, nine pulses are regenerated during one period of the chopper modulation frequency. In an experiment of 25 Hz and M/S = 3/9, a mean regenerative current of 40 amps was maintained while the motor developed -144 Nm at its output shaft. Figure 9.1a and c (also refer figure 9.4b) show the phase voltage and current and regenerative current in the dc supply for these parameters. The regenerative pulses developed are not synchronous with the original quasi-square waveform therefore are not in synchronism with the current pulse regenerated during the programmed underlap period.

9.2 Regeneration efficiency and torque.

Appendices D.8.1 to D.8.13 give results obtained when the test motor is excited with chopper modulated quasi-square phase voltages while operating in its regenerative region. Based on these results the following deductions can be made:-

(i) At an operating frequency of 8.3 Hz and mark space-ratio of 1/9 no

FIG 9.1a

CHOPPER MODULATE VOLTAGE AND CURRENT WAVEFORM DURING REGENERATION AT 25.0 Hz. TORQUE = -114Nm and Idc mean = -40A. MARKSPACE RATIO = 3/9.

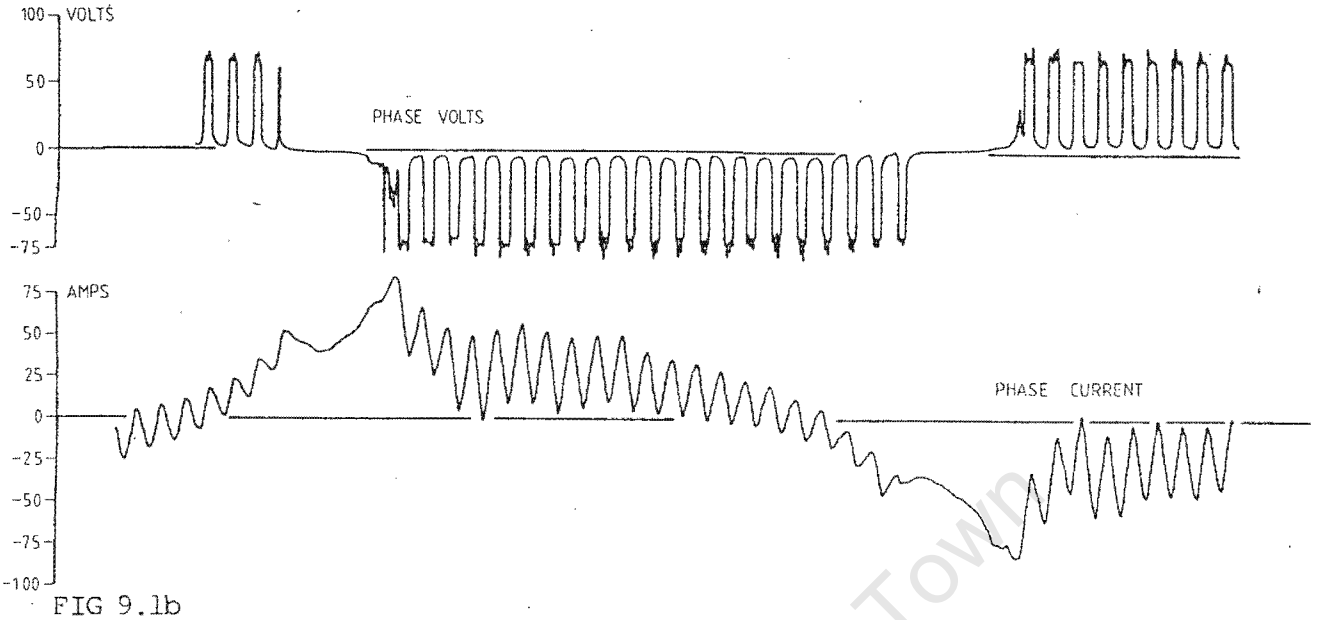

FIG 9.1b

CURRENT FROM DC POWER SOURCE WITH MOTOR NORMALLY LOADED, OPERATING FREQUENCY = 25.0 Hz AND MARKSPACE RATIO = 9/9. (Vdc WAS REDUCED TO ACHIEVE THIS WITHOUT SATURATION)

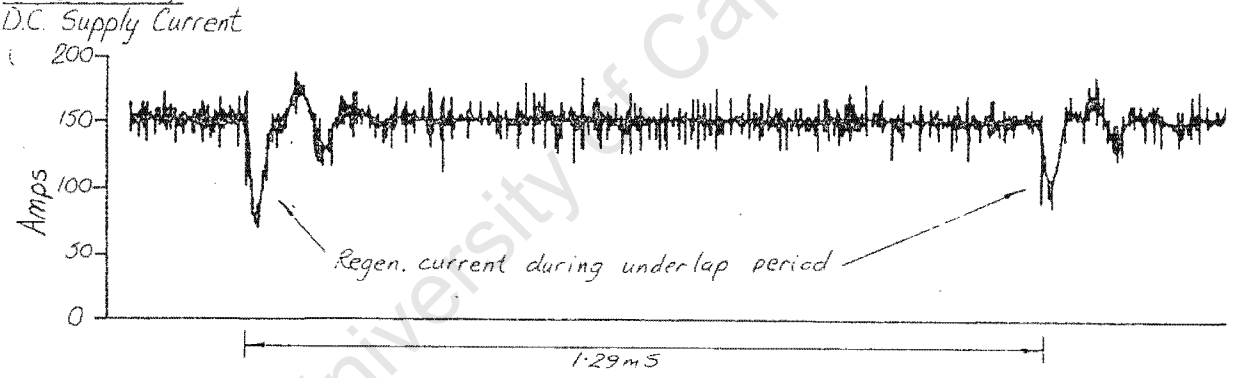

FIG 9.1c

REGENERATIVE CURRENT INTO DC POWER SOURCE WITH CONDITION AS PER FIG. 3.23a.

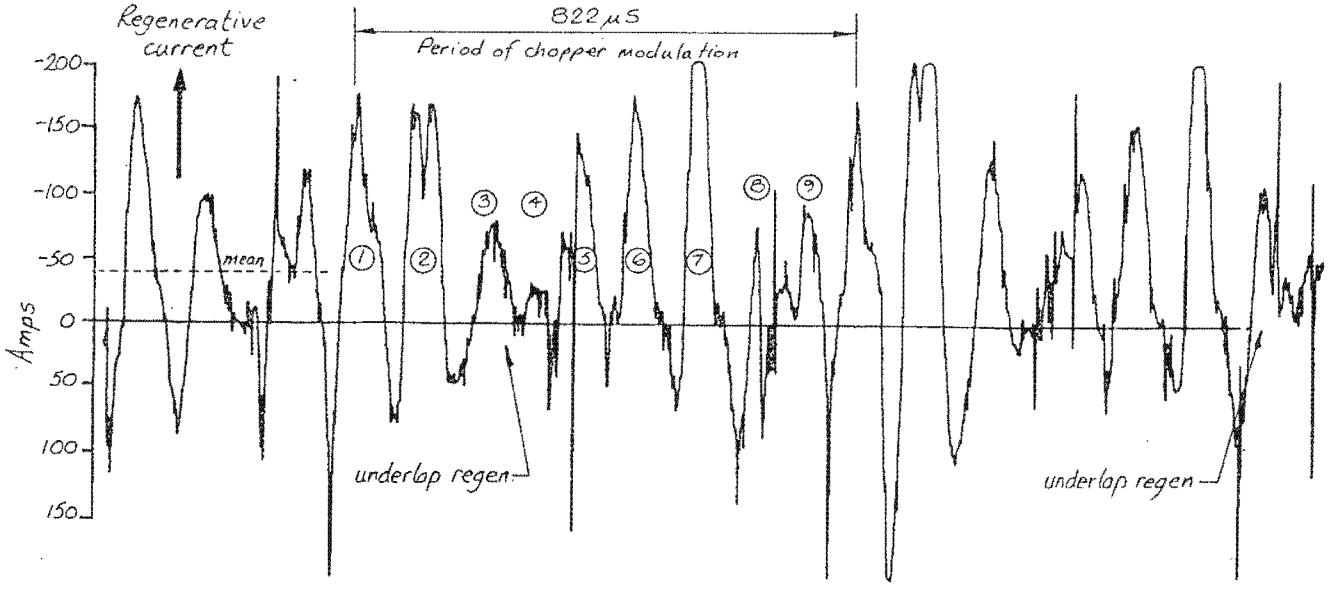

regeneration occurs (see figure 9.2). Although not recorded, it was found that the phase currents became excessively high if the mark-space ratio was increased above the optimum value, for 8.3 Hz, of 1/9.

(ii) In an attempt to assist regeneration at 8.3 Hz the chopper modulation frequency was decreased below 1.2 KHz, but as shown in figure 9.2 this was unsuccessful.

(iii) Regenerative currents can be induced at 10 Hz and above.

(iv) Regeneration can occur over a different negative torque range and sometimes at a slightly higher efficiency (see figures 9.3 and 9.4) if the mark-space ratio is reduced below its optimum value as determined for the positive torque region.

(v) In all cases if the mark-space ratio is increased by one, phase currents become excessively high and regeneration is negligible.

(vi) If the mark-space ratio is reduced further than one step down regeneration will start to occur closer to zero torque (see figure 9.4), thus moderate regenerative efficiencies can be acheived at low negative torques. In these cases the regenerative torque range is reduced.

(vii) Figure 9.5 shows that if frequency is increased above 49.9 Hz the peak regenerative efficiency does not increase when the mark-space ratio is reduced.

A complete set of regeneration efficiency curves at optimum mark-space ratios are given in figure 9.6 and the remainder of the regenerative current vs torque plots in figures 9.7a and b.

(iix) A system efficiency, ie. including bridge inverter losses, of up to 82% is obtainable at 74.9 Hz and M/S = 9/9. High efficiencies can be maintained at low torques when the motor is operated in its upper frequency range.

(ix) Both regenerative current and negative torques were exceptionally high

FIG 9.2

CURRENT DRAWN FROM SUPPLY AT 8.3 Hz VS NEGATIVE TORQUE.
NOTE OPTIMUM M/S RATIO = 1/9

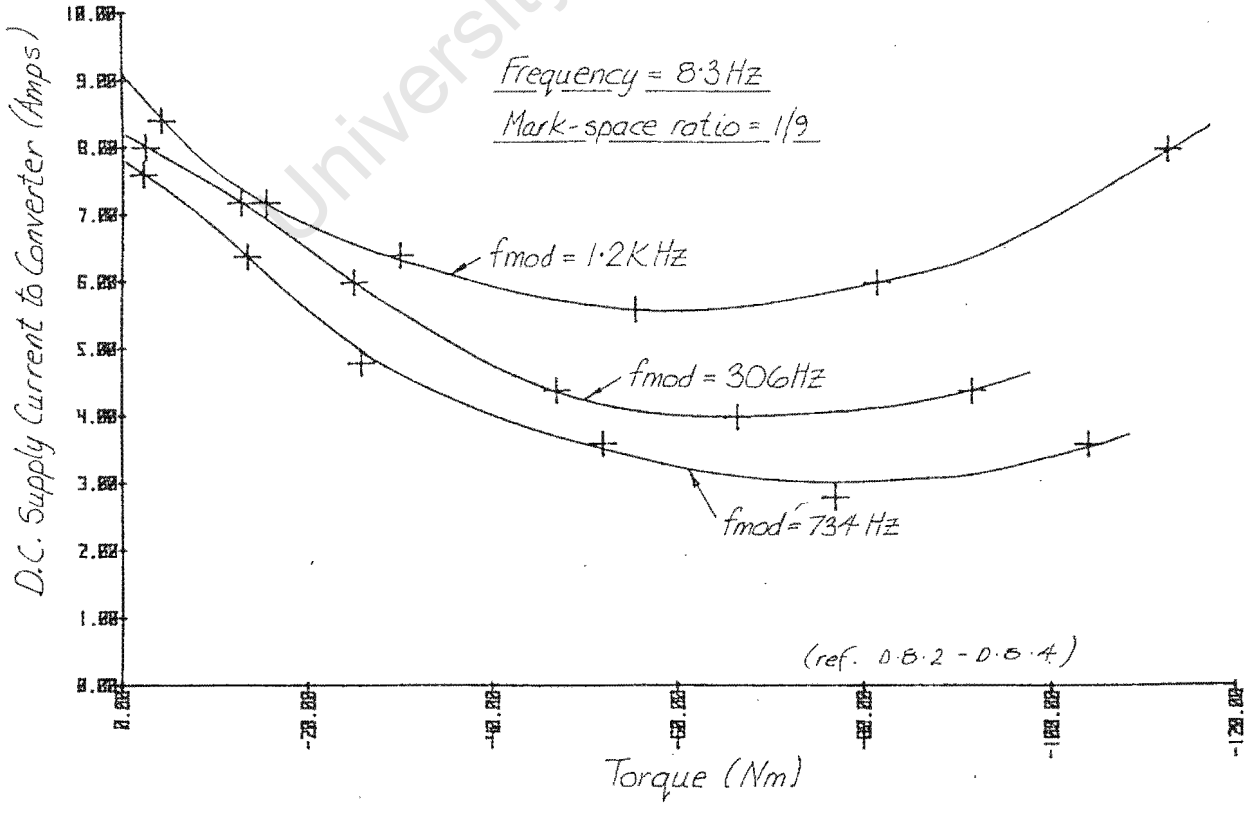

FIG 9.3a

SYSTEM REGENERATIVE EFFICIENCY AT 16.6 Hz VS NEGATIVE TORQUE.
NOTE OPTIMUM M/S RATIO = 2/9

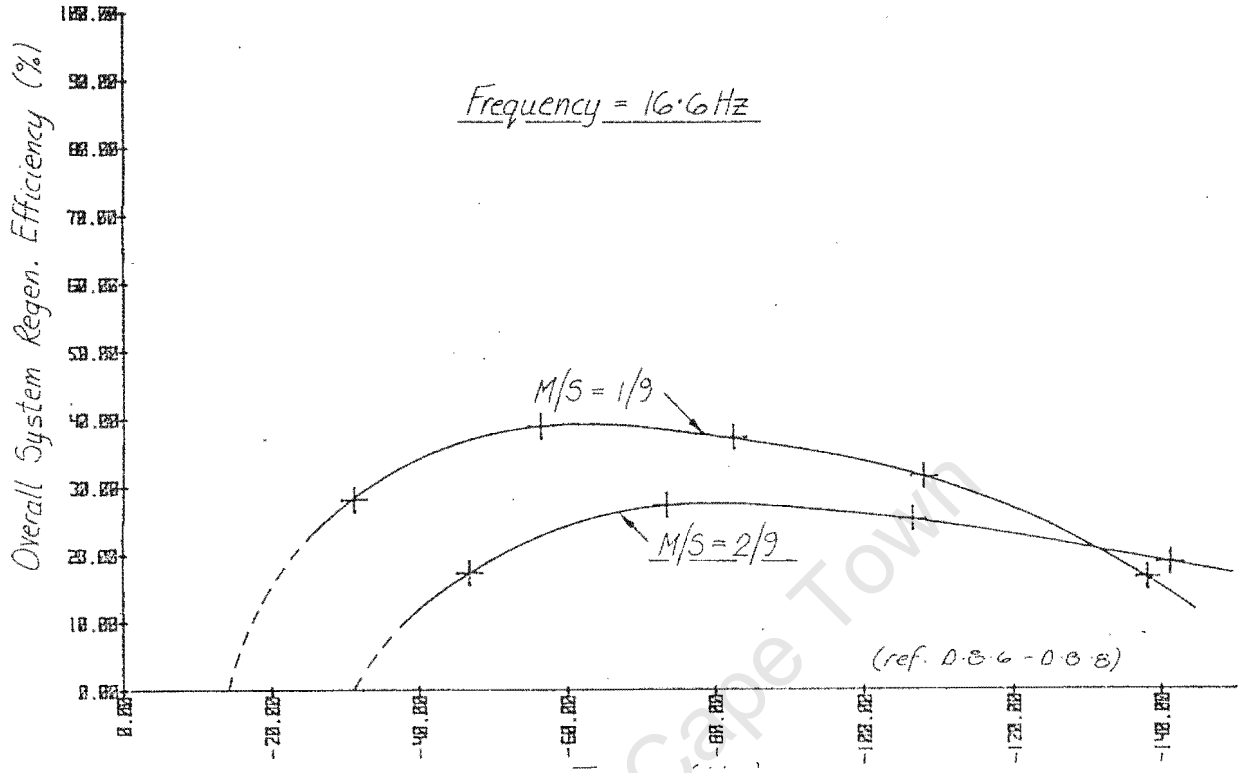

FIG 9.3b

REGENERATIVE CURRENT BACK INTO D.C. SUPPLY AT 16.6 Hz VS NEGATIVE TORQUE.

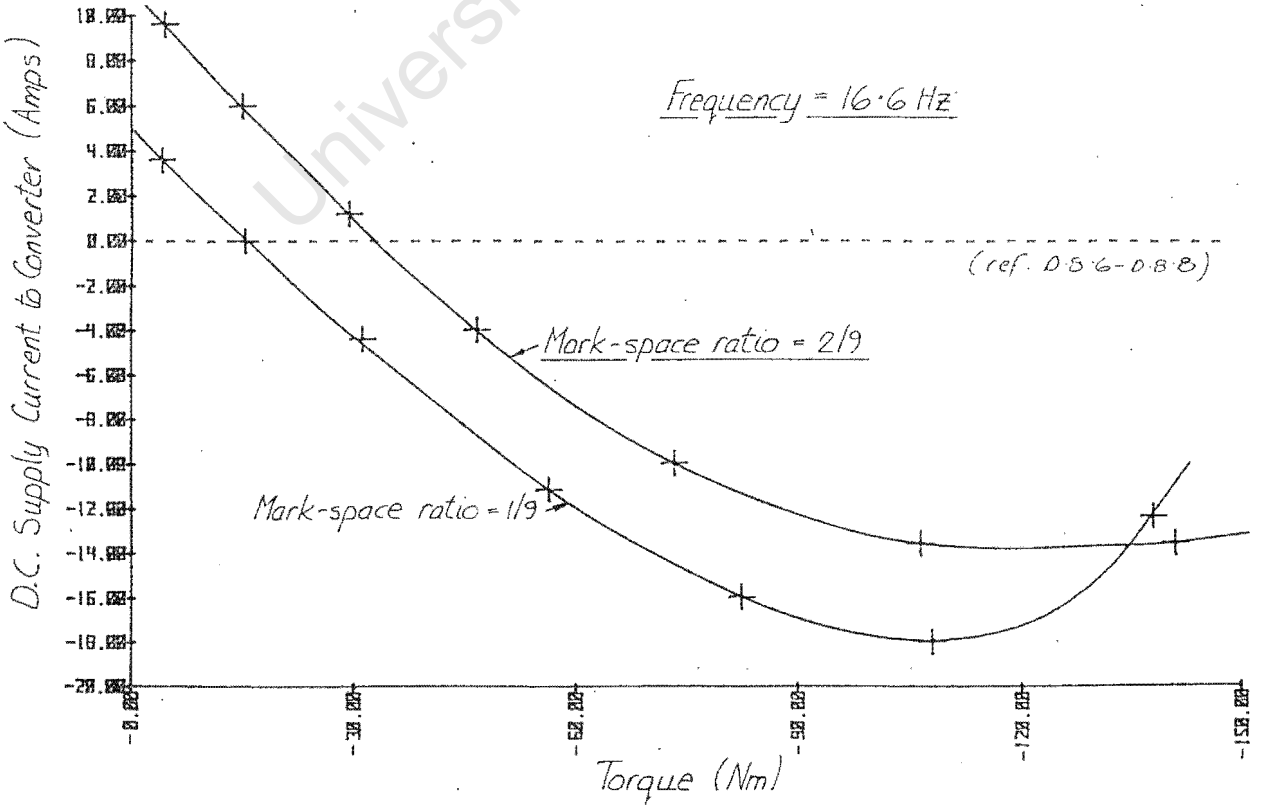

FIG 9.4a

SYSTEM REGENERATIVE EFFICIENCY AT 25.0 Hz VS NEGATIVE TORQUE.
NOTE OPTIMUM M/S RATIO = 3/9

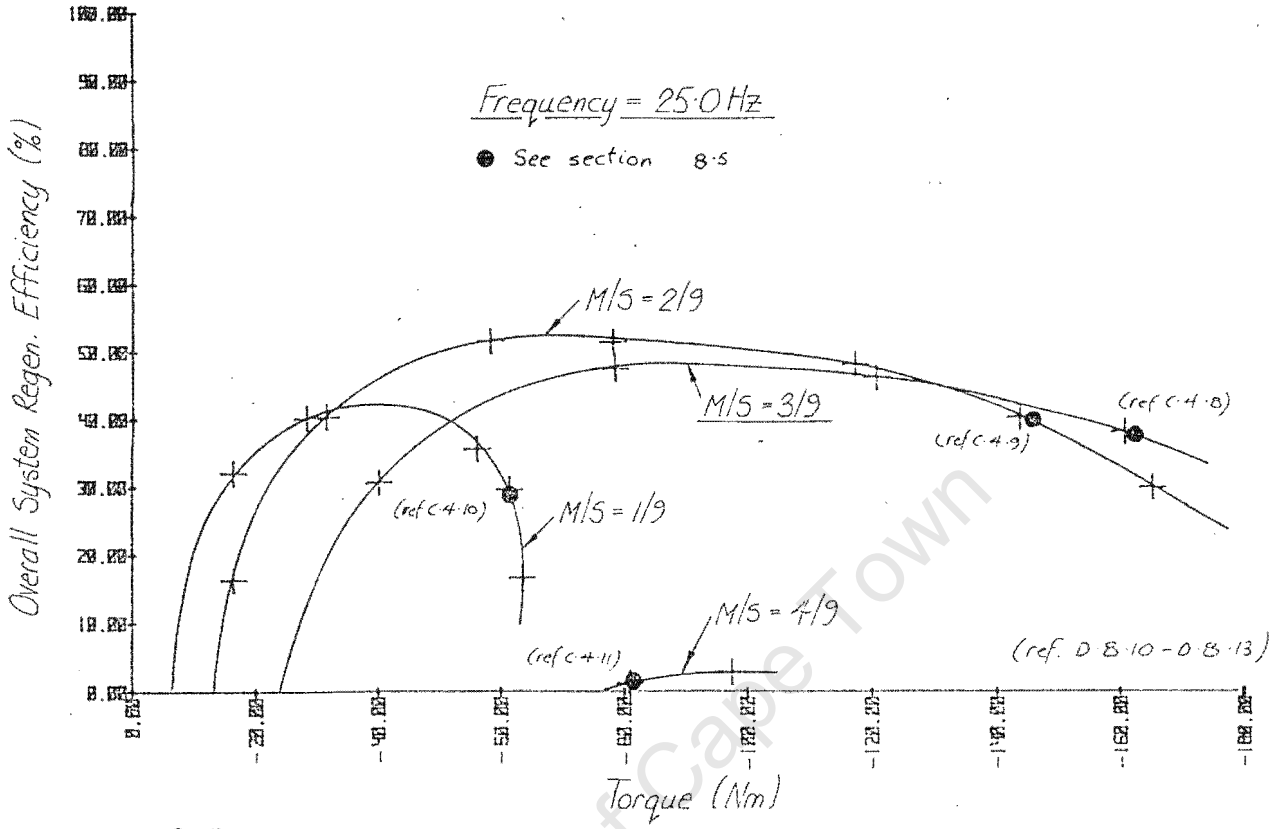

FIG 9.4b

REGENERATIVE CURRENT INTO D.C. SUPPLY AT 25.0 Hz VS NEGATIVE TORQUE

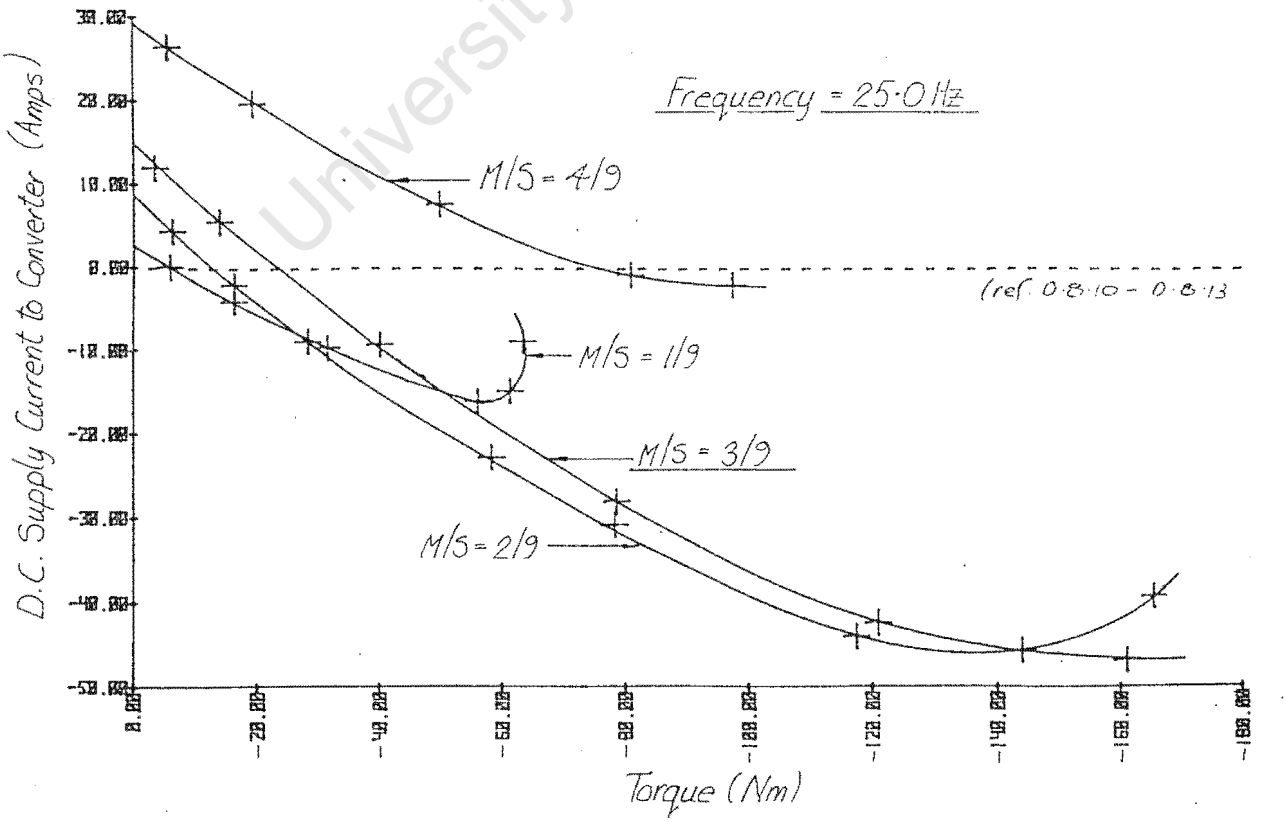

FIG 9.5

SYSTEM REGENERATION EFFICIENCY AT 49.9 Hz VS NEGATIVE TORQUE.
NOTE OPTIMUM M/S RATIO = 6/9

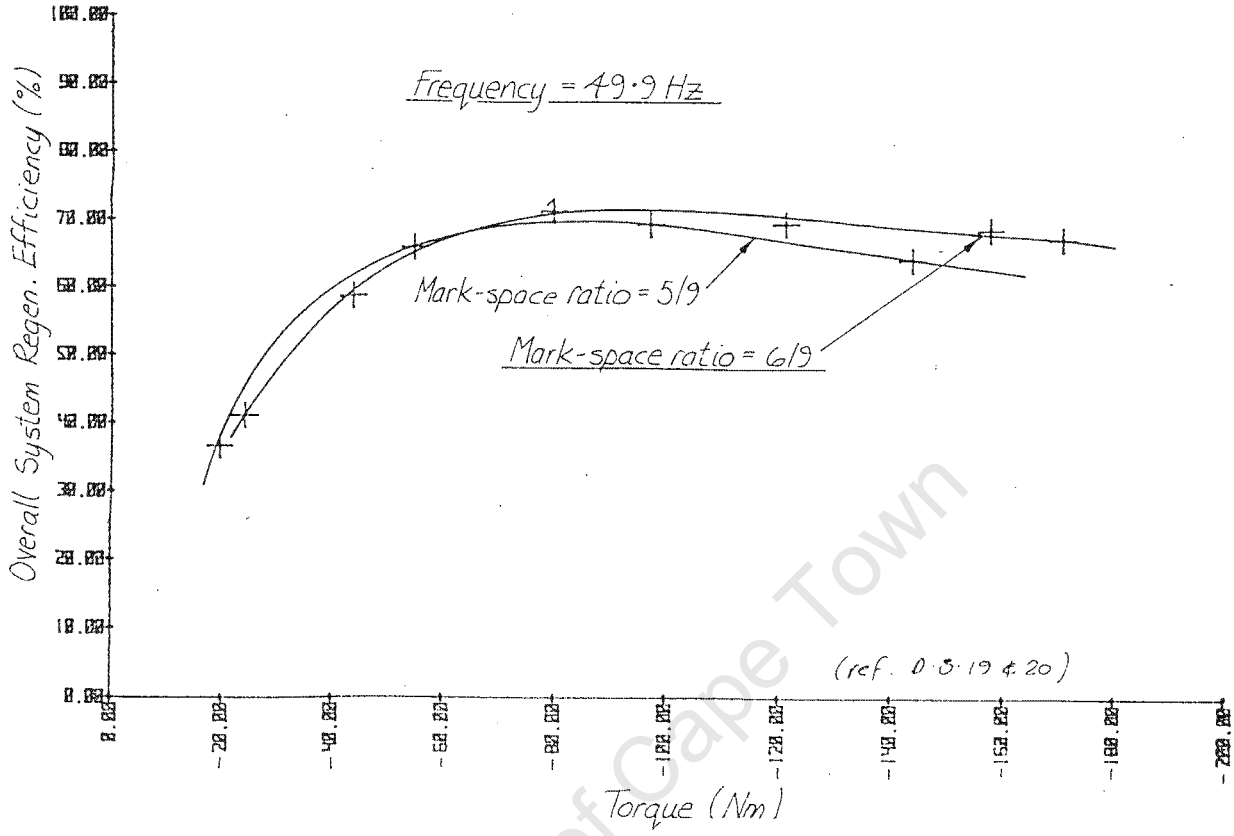

FIG 9.6

SYSTEM REGENERATIVE EFFICIENCY VS NEGATIVE TORQUE

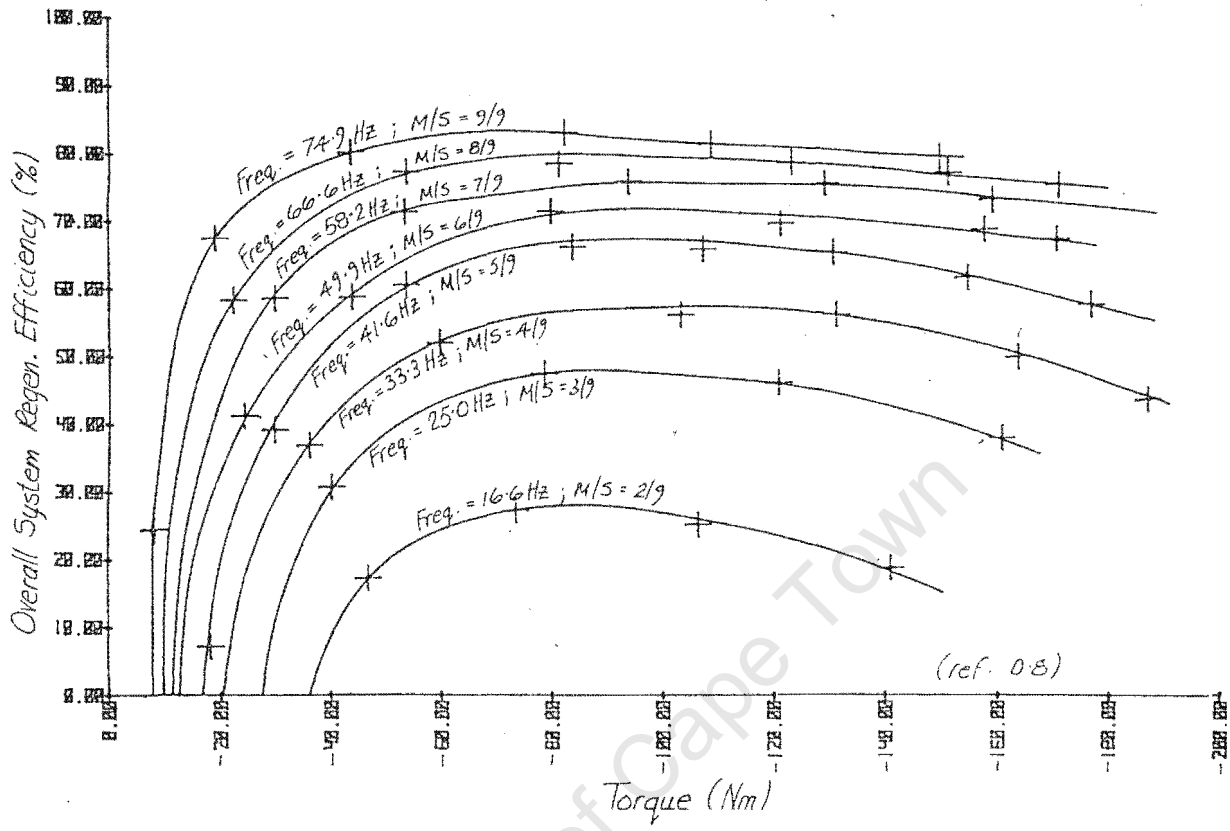

FIG 9.7a

REGENERATIVE CURRENT BACK INTO DC SUPPLY VS NEGATIVE TORQUE

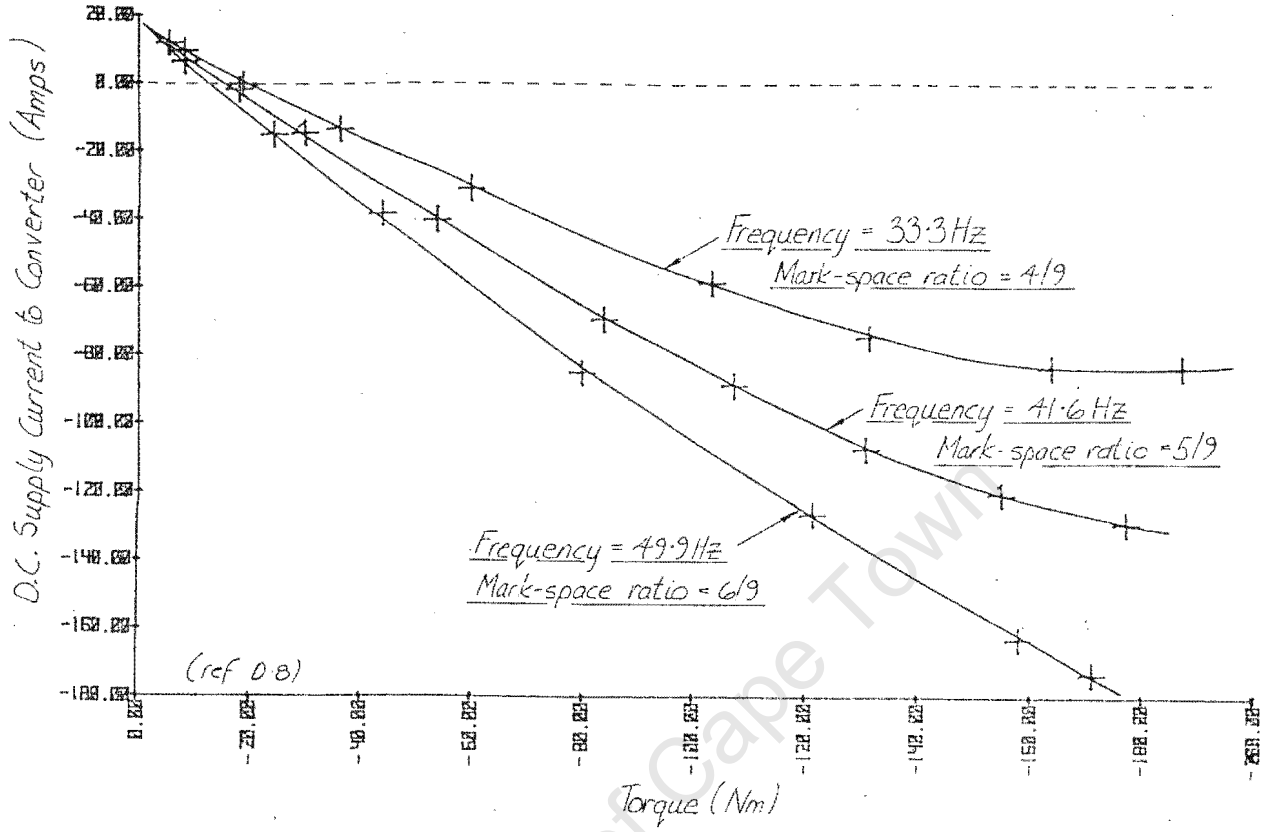

FIG 9.7b

REGENERATIVE CURRENT BACK INTO DC SUPPLY VS NEGATIVE TORQUE

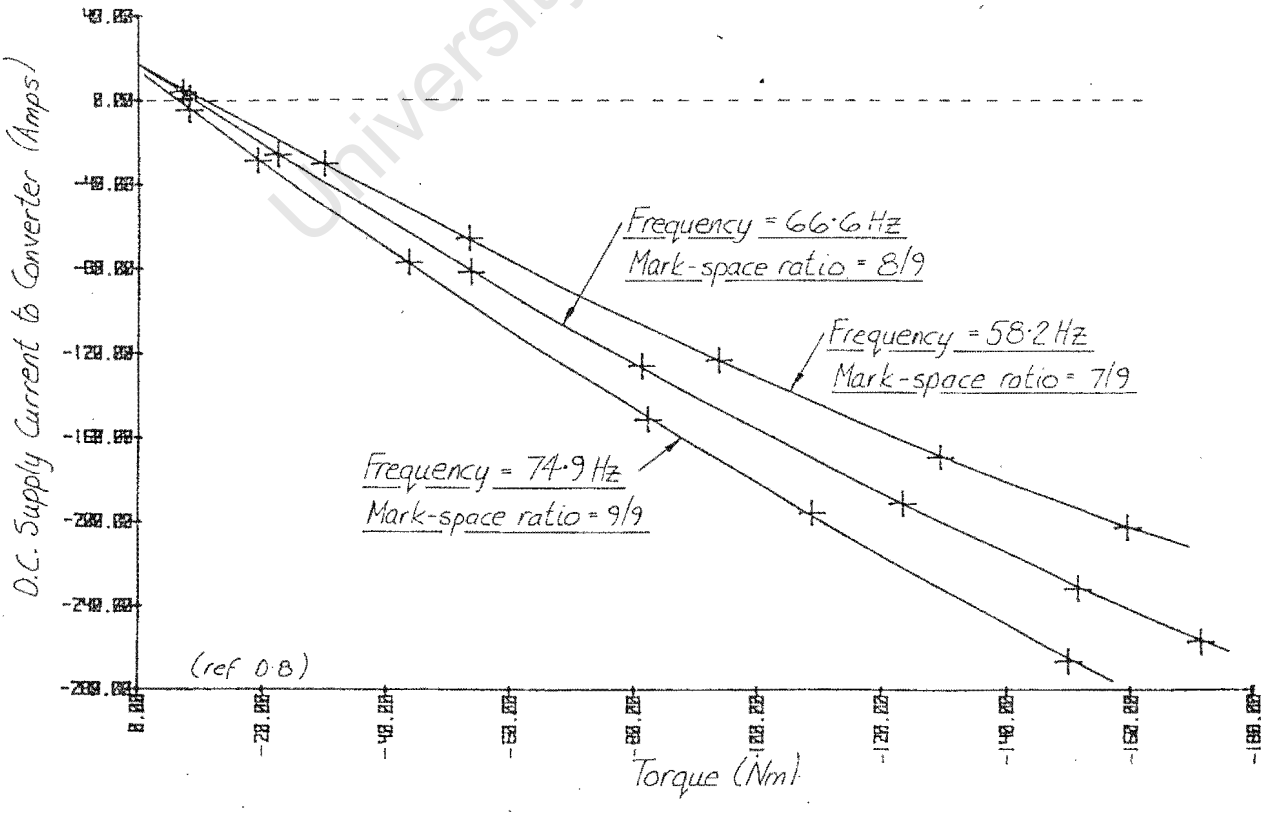

FIG 9.8a

SYSTEM EFFICIENCY IN THE MOTORING AND REGENERATIVE REGION VS OUTPUT TORQUE

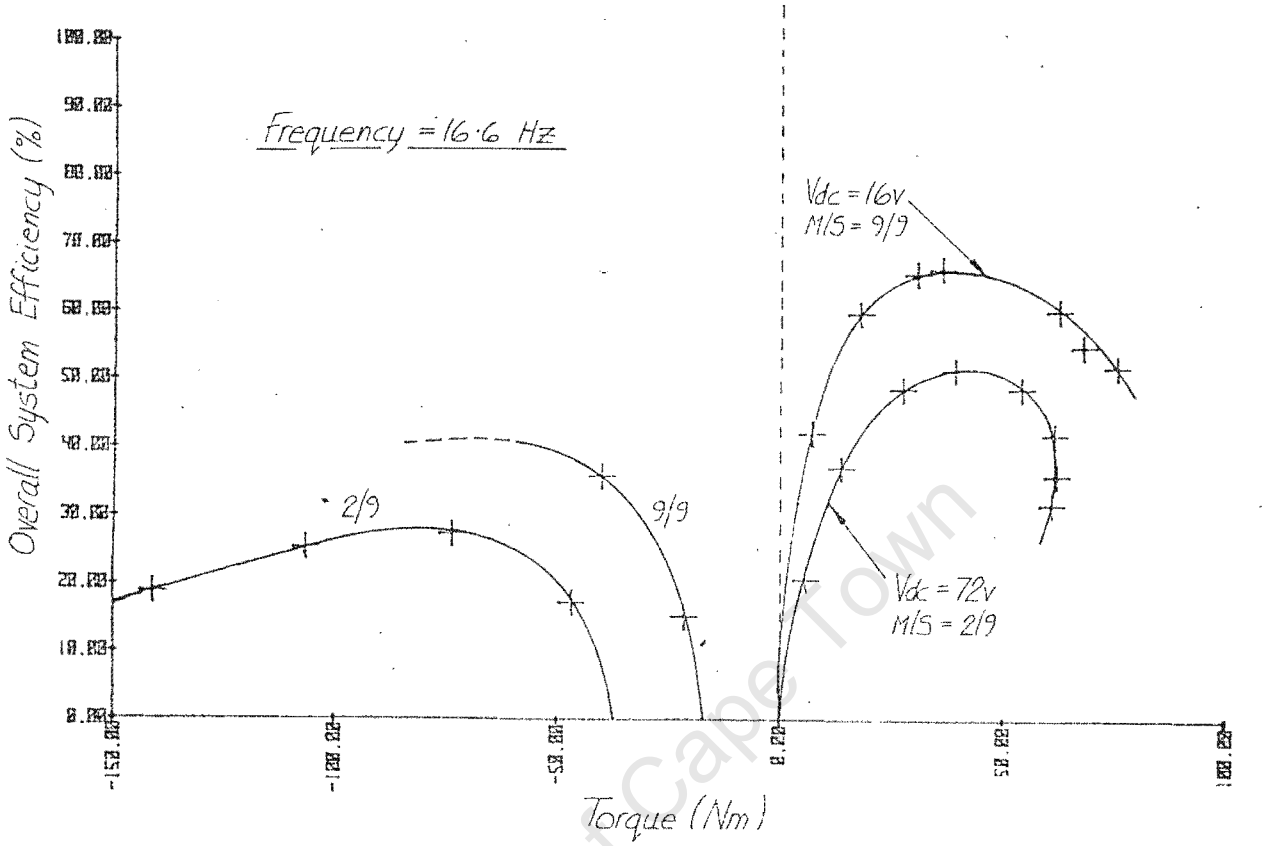

FIG 9.8b

SLIP VS TORQUE FOR A PURE QUASI-SQUARE WAVE AND A CHOPPER MODULATED QUASI-SQUARE WAVE

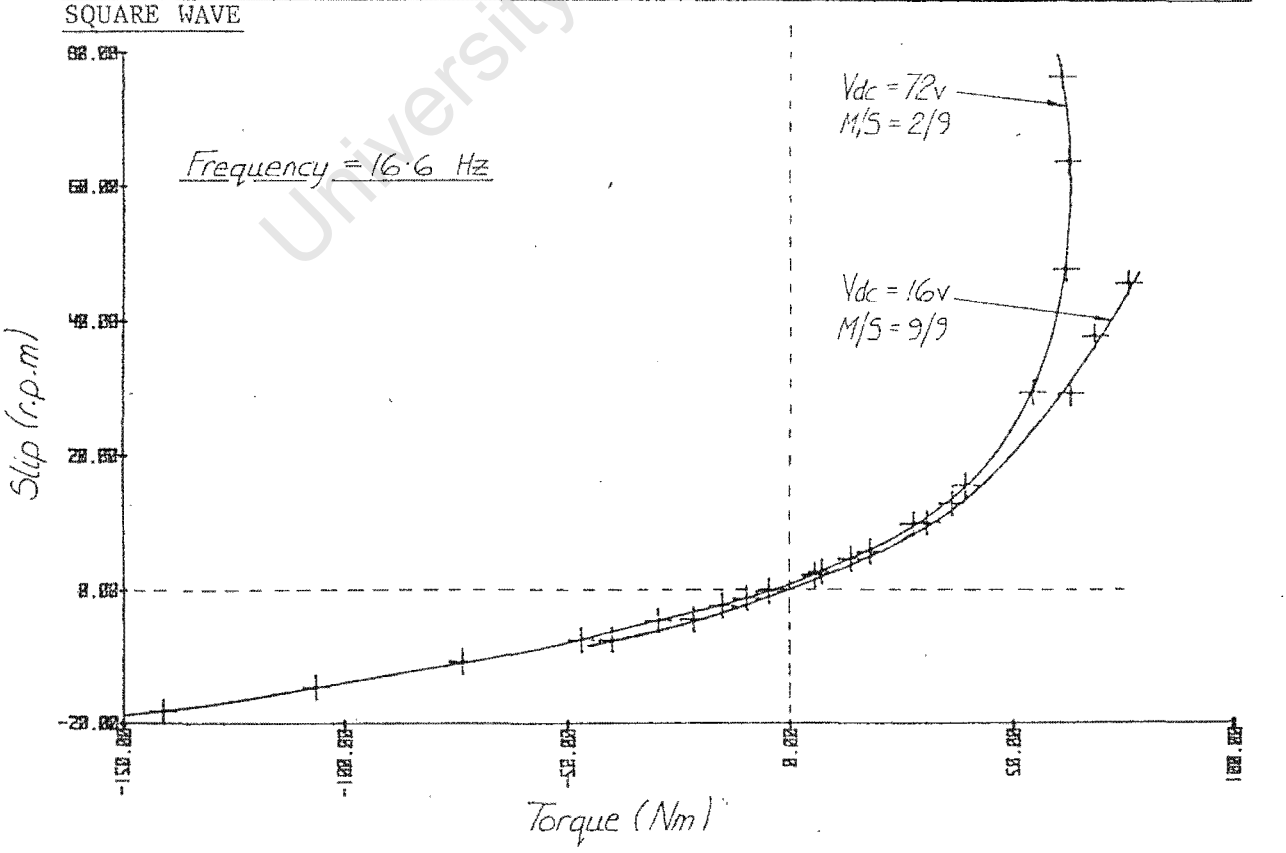

and the limits placed on them was due to maximum phase current being reached.

9.3 Comparing regeneration with and without chopper modulation.

The motor characteristics are compared when it is operating under the following conditions:-

(i) a frequency of 16.6 Hz was applied with the dc voltage equal to 72 volts and mark-space ratio equal to 2/9 giving optimum excitation.

(ii) a frequency of 16.6 Hz was applied with the mark-space ratio equal to 9/9 ie. pure quasi-square wave, and the dc voltage set at 16 volts to also give optimum excitation (see equation 6.4).

The torque-slip curves as shown in figure 9.8b are very similar between -50 Nm and +50 Nm, but the efficiency curve of the pure quasi-square wave excited motor, shown in figure 9.8a, is considerably higher in both the motoring and regenerative regions.

Problems were, however, encountered with stability when attempting to attain large negative torques at a mark-space ratio of 9/9.

Although not included in this thesis, the author did conduct extensive tests on two other machines which had deep bar squirrel cage rotors. These motors did not exhibit the excessive instability problems which appear to be inherent in the test motor.

Conclusion.

Variable speed control of a 9-phase squirrel cage induction motor excited with chopper modulated quasi-square phase voltages has been successfully carried out.

Theoretically it was shown that the contribution towards output torque by input harmonic power components, other than the fundamental, was very small (equation 1.36). Actual measurements proved this (D.12), and showed that the fundamental input power is approximately 95% of the total power drawn by the motor. An empirical analysis of the losses within the motor indicated that 99.5% of the output power was contributed by the fundamental.

Limitations in the output torque available at low frequencies due to chopper modulation of the quasi-square waveform is a serious setback, although not impossible to rectify. Higher torques are required at standstill and low speed to enable the vehicle to operate effectively when accelerating from standstill and climbing steep hills. Attempts to improve the torque by varying the chopper modulation frequency were unsuccessful (section 6.3). Originally the motor winding parameters were designed to accommodate a quasi-square waveform with mark-space ratio equal to 9/9 at 50 Hz, ie. unmodulated (section 3.1). As a result of saturation, the frequency was increased to 75 Hz (section 6.1). It is possible to increase the number of stator winding turns to optimize fluxing of the motor for M/S = 9/9 at a lower frequency. Thus, for a particular operating frequency, the mark-space ratio and peak torque would be higher.

This type of solution would cause the motor to be under excited at higher frequencies, but the subsequent reduction in torque in this region would not be too detrimental to the performance of a battery vehicle.

With the present winding configuration, however, higher output torques were developed at higher frequencies than when the motor was excited with 3-phase sine waves. Oscillograms of output torque showed that the 9-phase motor, in general, gives a lower amplitude torque pulsation than the same motor excited with sine waves.

Another method of solving the problem would be to use pole amplitude modulation to achieve pole changes. The electronic logic controller provides a easy method of switching phases, although this was not possible during testing due to the winding configuration.

Peak motor efficiencies of above 80% were achieved at the higher mark-space ratios (C.3), ie. at f=66.6 & 74.9 Hz. By changing the mark-space ratio as torque varied (figure 8.2) efficiencies of above 50% could be maintained over the majority of the torque-speed range. For instance, at an operating frequency of 33.3 Hz the efficiency only drops below 50% if the torque is reduced below 7 Nm. Above that the efficiency remains between 60% and just over 65% for almost the whole torque range up to maximum torque of approximately 90 Nm.

Comparing the efficiency of the 9-phase chopper modulated motor to the same motor excited with 3-phase sine waves, shows that higher efficiencies can be gained by the 9-phase motor in its medium to high speed, low torque range (figure 8.3). It is virtually impossible to generalize when comparing the efficiencies of the two types of excitation and it is necessary to study the efficiency contour graphs in figures 7.1 and 8.2 at specific operating points to make a worthwhile judgement.

The limited number of mark-space ratios meant that the motor could not operate below 8.3 Hz (figure 6.2) without saturating it. A higher number of mark-space steps could be provided, ie. 18 or 27, but interlacing would not be effective. If the stator winding were modified as previously suggested lower frequencies could be reached.

Problems were encountered when changing from one mark-space ratio to another with a dc supply of 72 volts because no allowance had been made for an inter-switching sequence in the digital controller. This caused currents of high amplitude and short duration to be developed whilst the logic was changing to the new setting. Further development work needs to be done in this area.

Interlacing was not completely successful in providing a smooth dc supply due to the variation in switching times of the ESM 1000 power transistor as load current changed. It is necessary to automatically modify the

interlacing time delay (figure 2.3) as load current changes. The test system digital controller was unable to do this except via a preset potentiometer.

The bridge inverter switching sequence which allowed the motor to operate between its motoring and regenerative regions without changing any control parameters was very successful. It was found, however, that regeneration could be achieved at lower torques, and in some cases higher regeneration efficiencies, for a particular operating frequency if the mark-space ratio was decreased (figure 9.4) from its optimum value. Overall system peak regeneration efficiencies varied between 28% at f = 16.6 Hz and M/S = 2/9 to 83% at f = 74.9 Hz and M/S = 9/9 (figure 9.6). It was not possible to reach maximum negative torque due to the very high regenerative phase currents developed. Regeneration did not occur at frequencies less than approximately 10 Hz and varying the chopper modulation frequency (figure 9.2) in an attempt to achieve it was unsuccessful.

Large instabilities were encountered when operating the motor under certain conditions. The presence of a 'low stiffness' torque transducer in the system did not improve the stability. The 3-phase sine wave and 9-phase unmodulated quasi-square wave tests were partially restricted due to resonance occuring. However, once chopper modulation was introduced, the system became more stable, but even here the system would occasionally resonate although not seriously. When tests were performed on another motor which had a double cage rotor and a larger number of stator winding turns a definate improvement in the stability was noticed. Further work is necessary to determine the influence of the motor parameters on the performance of the motor excited with chopper modulated quasi-square waves.

The particular rotor cage construction resulted in a very small slip window, ie. slip between synchronous speed and speed at maximum torque. In practice, the window needs to be larger than the approximately 30 rpm slip developed so that torque and speed can be more closely controlled by the digital controller. Therefore, at a particular torque a higher slip and regrettably a lower efficiency can be obtained.

It was noted that for a 3-phase sinusoidally excited motor magnetizing current was drawn continuously from the 3-phase supply. For a quasi-square wave excited motor magnetizing current is not drawn continuously but in

small pulses and by only one phase winding at a time causing lower efficiencies. The number of phases used and the freewheel angle has a direct effect upon the width of the magnetizing pulse and the amount of magnetizing power that can be supplied each cycle. Research needs to be done to determine if by lowering the number of phases to 7 or maybe 5, higher efficiencies can be achieved. This is without losing the advantage of low phase currents as a result of the higher phase number. With these points in mind, it would also be worth studying the operation of a 9-phase synchronous motor which would not need magnetizing current.

The bridge inverter performed very well, although unwanted losses are incurred by the base drive inverters. The development of a base drive circuit which delivers current according to demand should be considered as a future project, although this will not be necessary once high power switching FET's become available to replace the existing ESM 1000 power transistors.

The use of a dc to dc converter between the primary dc source (battery) and the bridge inverters should be considered in any future project. Chopper modulation would therefore be done at the dc to dc converter, producing a continuously variable dc supply feeding the bridge inverters, themselves operating in the unmodulated quasi-square wave mode. This solution will negate or decrease the following problems:-

(i) Low torque at low operating speeds.
(ii) Limited efficiency at low operating speeds.
(iii) Operating frequency cannot be reduced below 8.3 Hz because of saturation.
(iv) Transistor switching losses in bridge inverter.
(v) Voltage and current spikes on dc supply line due to inneffective interlacing.
(vi) Complex digital control circuitry required to implement interlacing.

Controlled regeneration would, however, have to be investigated.

The applications in which the drive system could be used are:-

(i) Heavy and light duty passenger and goods vehicles.
(ii) Small locomotives used in the mining industry.
(iii) Various variable speed applications in the construction and manufacturing industry.

In conclusion, some modifications to the bridge inverter and motor are necessary to make them practically viable for use in a battery vehicle, but the basic concepts supporting the use of more than three phases have been proven.

REFERENCES.

1) Performance and design of induction motors with square-wave excitation. Maclean, Alwash & Nix, PROC IEE, Vol. 116, No. 8, Aug 1969, p1405.

2) Preliminary investigation of an inverter-fed 5-phase induction motor. E.E.Ward, PROC IEE, Vol. 116, No. 6, June 1969.

3) Alternating current machines. M.G. Say, Pitman, p16.

4) Electric machines. Thaler and Wilcox, Wiley, p452.

5) Reference 3, p18.

6) Harmonic field effects in induction machines. Heller and Hamata, Elsevier, p104.

7) Induction motor drive for a battery vehicle. M. Malengret, MSc Thesis, U.C.T. 1978.

8) Power transister inverter. K. Hoffman, BSc Thesis, U.C.T. 1979.

9) Steady-state stability criterion for induction motors. P. Bowler & B. Nir, PROC IEE, Vol. 121, No. 7, July 1974, p663.

10) Power transistors in the switching mode. SESCOSEM 1975 Resumes.

11) Variable frequency and voltage drive logic. M. Scrooby, BSc Thesis, U.C.T. 1979.

12) The feasibility of using pole-change motors in inverter drive systems. N.C. Enslin, University of Cape Town Research Review, Vol. 6, No. 6, Sept/Oct 1982, p236.

13) Higher Electrical Engineering, Shepard,Morton & Spence, Pitman, p242.

14) Inverter fed induction motor. A.R.Pocock, BSc Thesis, U.C.T. 1978.

15) Reference 13, p241.

16) A technique for assessing space harmonic effects in squirrel cage induction motors. C.F.Landy, Transactions SAIEE, Vol. 73, Part 1, January 1982, p2.

17) Harmonic analyser developed by N.C. Enslin (U.C.T.). Capable of measuring the amplitude and phase relationship of voltage, current and power up to the 19th harmonic for single phase or 3-phase circuits.

18) Steady state oscillations and stabilisation of variable frequency inverter fed induction motor drives. F. Fallside & A.T. Wortley, PROC IEE, Vol. 116, No. 6, June 1969, p991.